Fiber-optic integration and efficient detection schemes for optomechanical resonators

Thesis by

Justin D. Cohen

In Partial Fulfillment of the Requirements

for the Degree of

Doctor of Philosophy

California Institute of Technology

Pasadena, California

2015

(Defended March 27, 2015)

Acknowledgements

It is probably impossible to properly thank everyone who has helped me on my path to this amazing point of my life, but I will attempt to do so here.

I have to begin by thanking Oskar Painter. Oskar, your guidance and support through my time at Caltech has been the foundation of all I have achieved here. Your excitement and brilliance in our field, as well as your unwavering belief in our capabilities, inspired me many times to attempt things I said couldn't be done, and you were usually right! Your talent for putting together the right kinds of people has made this experience both fun and successful.

While I strongly believe in making your own luck by putting yourself in the position to *be* lucky, you still need that person on the other end to take a chance on you sometimes. I profoundly thank everyone who has ever taken a chance on me, either by spending precious time mentoring me or by accepting an application. In reverse chronological order, thank you Thiago Alegre, Raviv Perahia, Oskar Painter, Caltech Physics Graduate Admissions Committee of 2009, Dylan Sweeney, Guido Mueller, Aidan Brooks, Keita Kawabe, Cheryl Vorvick, Daniel Sigg, Jerry Barry, Dan Pajerowski, Mark Meisel, University of Florida Admissions Department of 2005, and Jonathan Keohane. I also sincerely thank the many excellent instructors and teachers throughout my education.

I am extremely thankful for those specifically few long-lasting and all-time great friendships for the companionship I constantly rely on even over long distances and periods of neglect between our encounters. Thank you Ericka Garcia, Brandon and Jenna Bostwick, Chad Engel, Casey Johnson, and Amanda Arsenault. I also thank my close group of Caltech friends, who can be relied on to share the highs and low of grad school: Ari Weinstein, Laura DeLorenzo, Emma Wollman, Joseph Redford, Chan U Lei, Max Jones, Su-Peng Yu, Zach Korth, Mattias Rydenfelt, William Fegadolli, and Pinkesh Patel.

I have also been particularly lucky to find myself in a research group where I consider its members to be very good friends. Thanks to all of you past and present Painter group members for all the fun times in the lab as well as for helping me on countless occasions: Alex Krause, Tim Blasius, Amir Safavi-Naeini, Jasper Chan, Johannes Fink, Carly Donahue, Michelle Aldecua, Barry Baker, Alessandro Pitanti, Richard Norte, Taofiq Paraiso, Matt Matheny, Martin Winger, Qiang Lin, Matt Eichenfield, Jessie Rosenberg, Ryan Camacho, Mahmoud Kalaee, Kejie Fang, and Xingsheng Luan.

I must also acknowledge the graduate students of yesteryear, whose hard work developing fabrication recipes and building laboratory infrastructure laid the foundation for my achievements: Matt Borselli, Kartik Srinivasan, Paul Barclay, Tom Johnson, and Chris Michael. A specific thank you to everyone who I have collaborated with on projects: Seán Meenehan, Greg MacCabe, Simon Groeblacher, Jeff Hill, Raviv Perahia, Thiago Alegre, Matt Shaw, and Francesco Marsili, we made great teams!

I'll never be able to thank Seán enough for being such a fantastic teammate and collaborator. Seán, I have a huge amount of respect for your brilliant scientific aptitude and your determined approach to problem solving. I am immensely fortunate to have had the opportunity to work with you.

To my family, thank you for shaping me into the person I am today and for your unconditional love and support. To Gramma Phyllis, Grampa Stu, and Gramma Sylvia, thank you for always believing in me and for your unconditional support. Mom and Dad, thank you for showing me how to be the person I want to be, I see your example every day in my choices and approaches to problems. Without your encouragement to pursue my passions I never would have done any of this. Sam, thank you for being the best kind of brother anyone could ask for, supportive, insightful, easy to talk to, and fun to be around.

To my amazing wife Kelsey, how do you thank someone for the joy in life? Whether I have a good day or a bad day in the lab, every day is a good one once I come home to you. I don't know if I could have made it through this experience without your love and companionship, and I'm glad I didn't have to. Thank you for being you and for putting up with me.

Abstract

With the advent of the laser in the year 1960, the field of optics experienced a renaissance from what was considered to be a dull, solved subject to an active area of development, with applications and discoveries which are yet to be exhausted 55 years later. Light is now nearly ubiquitous not only in cutting-edge research in physics, chemistry, and biology, but also in modern technology and infrastructure. One quality of light, that of the imparted radiation pressure force upon reflection from an object, has attracted intense interest from researchers seeking to precisely monitor and control the motional degrees of freedom of an object using light. These optomechanical interactions have inspired myriad proposals, ranging from quantum memories and transducers in quantum information networks to precision metrology of classical forces. Alongside advances in micro- and nano-fabrication, the burgeoning field of optomechanics has yielded a class of highly engineered systems designed to produce strong interactions between light and motion.

Optomechanical crystals are one such system in which the patterning of periodic holes in thin dielectric films traps both light and sound waves to a micro-scale volume. These devices feature strong radiation pressure coupling between high-quality optical cavity modes and internal nanomechanical resonances. Whether for applications in the quantum or classical domain, the utility of optomechanical crystals hinges on the degree to which light radiating from the device, having interacted with mechanical motion, can be collected and detected in an experimental apparatus consisting of conventional optical components such as lenses and optical fibers. While several efficient methods of optical coupling exist to meet this task, most are unsuitable for the cryogenic or vacuum integration required for many applications. The first portion of this dissertation will detail the development of robust and efficient methods of optically coupling optomechanical resonators to optical fibers, with an emphasis on fabrication processes and optical characterization.

I will then proceed to describe a few experiments enabled by the fiber couplers. The first studies the performance of an optomechanical resonator as a precise sensor for continuous position measurement. The sensitivity of the measurement, limited by the detection efficiency of intracavity photons, is compared to the standard quantum limit imposed by the quantum properties of the laser probe light. The added noise of the measurement is seen to fall within a factor of 3 of the standard quantum limit, representing an order of magnitude improvement over previous experiments utilizing

optomechanical crystals, and matching the performance of similar measurements in the microwave domain.

The next experiment uses single photon counting to detect individual phonon emission and absorption events within the nanomechanical oscillator. The scattering of laser light from mechanical motion produces correlated photon-phonon pairs, and detection of the emitted photon corresponds to an effective phonon counting scheme. In the process of scattering, the coherence properties of the mechanical oscillation are mapped onto the reflected light. Intensity interferometry of the reflected light then allows measurement of the temporal coherence of the acoustic field. These correlations are measured for a range of experimental conditions, including the optomechanical amplification of the mechanics to a self-oscillation regime, and comparisons are drawn to a laser system for phonons. Finally, prospects for using phonon counting and intensity interferometry to produce non-classical mechanical states are detailed following recent proposals in literature.

Contents

List of Figures

List of Tables

Preface

My graduate school experience has been as much about self discovery as an exploration of a fascinating subject. While this dissertation describes this exploration in detail, here I will take the opportunity to look back on the path I have walked.

After graduating from college with the majority of my research experience in magnetic material properties at low temperature, and a brief but exciting summer research experience at the LIGO Hanford Observatory, I knew that I wanted to explore "optics in general and quantum optics in particular," to quote my first email to Oskar Painter. With little specific interest in applied technology or engineering at the time, I was drawn to Oskar's group by reading about their compelling cavity QED experiments with quantum dots in chip-based optical cavities. Oskar, with his characteristic zeal, let me get an early start on research that summer by joining the quantum dot team of postdocs Raviv Perahia and Thiago Alegre. As these things sometimes go, the focus of this team's project shifted almost immediately after my arrival to an experimental demonstration of electromechancially-tunable nanolasers. While slightly disappointed at the time to be shifted away from quantum optics, I was content to learn the ropes with this new goal.

Raviv and Thiago proved to be excellent mentors, and I soon found myself a proficient user of the Painter group clean room facility. This introduction to photonics and fabrication turned out to be an ideal starting point for me, unexpectedly forming the foundation of my developing aptitude for hands-on, applied science. As we moved into the testing and characterization phase of the project, we were joined by another first year student, Seán Meenehan. As Thiago and then Raviv moved on to other pursuits, Seán and I assumed responsibility for the work, and thus began our fruitful and rewarding partnership.

By the beginning of our second year, we had successfully brought the nanolaser work to publication, and Seán and I were ready for our next pursuit. Oskar suggested revisiting quantum dots, this time coupled to electromechanically tunable optical cavities building on the capabilities developed by our previous project. I was thrilled to return to cavity QED, and plunged into fabrication. Despite some solid achievements, such as our demonstration of the highest quality factor gallium-arsenide-based photonic crystal, this experience was ultimately disappointing, as difficulties in fabrication and bleak prospects of significant results from simulation led us to change directions after a year of

effort. While letting go of this enterprise was difficult, Seán and I took our lessons in the importance of foresight and nimble response to evolving situations in stride as we moved on to our next challenge.

Until this point, mine and Seán's connection to the blossoming field of optomechanics was tertiary, in that we used it as a tool for electromechanical tuning of cavity resonances, rather than an end in and of itself. Observing the success of our fellow group members Jasper Chan, Amir Safavi-Naeini, Jeff Hill, Alex Krause, and Thiago in the laser cooling of silicon optomechanical crystals however, made it clear that a focused effort on optomechanics was the best route forward for a successful graduate career. A dilution refrigerator was on its way to our group, and there was a critical need for the development of efficient, cryogenically compatible optical coupling shcemes. It was at this point that Seán and I started to become a well-oiled machine. While Seán helmed the design and simulation front of our effort, I pursued fabrication. Splitting the problem into our respective complementary strengths turned out to be an excellent division of labor, and we soon had demonstrated the V-groove optical fiber couplers described in the beginning of this dissertation. Working together on optical characterization and experimental design, we used these couplers to perform a high-precision continuous position measurement of a zipper optomechanical resonator, and also exported our technology to several other teams both within and outside of the Painter group.

By the middle of our fourth year, Seán and I moved on to silicon optomechanical crystals, as most of the previous team was moving on in their careers. Here we were joined by Simon Groeblacher and Jeff Hill for a short time, as we developed new fiber couplers and spectroscopy capabilities for measuring mechanical states cryogenically cooled in a dilution refrigerator to milliKelvin temperatures. We learned of a complex interplay between optomechanical and thermal effects at these temperatures, motivating a shift to a new approach, photon counting. In this regard we were extremely fortunate to be acquainted with Jeff Stern, Matt Shaw, and Francesco Marsili of JPL, who in collaboration with NIST had recently showcased the best single photon detectors in the world for near-infrared light. With Matt and Francesco's generous offering of detectors and expertise, we were armed with a powerful new tool for efficiently measuring motional ground states of cryogenically-cooled optomechanical crystals.

Over the course of preparing for our next cryogenic experiment, Seán and I were joined by a new student to the group, Greg MacCabe. Together we developed the phonon counting technique enabling the main results of this dissertation. While further experimental progress was needed before our next cooldown, at this point we realized that we were already poised to perform a novel measurement. Using two single photon detectors to perform intensity interferometry, we could map and measure the coherence properties of the acoustic field of our optomechanical crystal at room temperature with the reflected probe light. Furthermore, we had access to two distinct physical states

of the nanomechanical oscillator; thermal motion and coherent motion produced by optomechanical amplificiation to a self-oscillation regime. I asked Seán if he thought it was worth an extra long weekend to check it out. It was, and this measurement was the most rewarding of my graduate career, showing me that it was true that sometimes the best results come easily after preparation and experience.

For our final experiment, Seán, Greg, and myself combined our phonon counting techniques with pulsed laser probing at milliKelvin temperatures. This measurement allowed us to directly measure the dynamics of optical absorption heating and cooling effects in the optomechanical resonators, verifying the difficultly-extracted results of our previous cryogenic experiment. We finally demonstrated simultaneous deep-quantum-ground-state mechanical occupations and large coherent coupling between photons and phonons, as well as long thermal decoherence times of the mechanical motion.

Looking back, my interests and aptitudes are vastly different now from when I began grad school. While my final year of study has yielded great success, I am primarily proud of the practical advancements we made along the way. Instituting new fabrication protocols, constructing instrumentation, and contributing to the infrastructure of the research group are a few of my acquired abilities which I most value, and I am looking forward to how I can use them in the future.

Chapter 1

Optical Coupling to Microscale Optomechanical Resonators

This chapter will provide an introduction to optomechanical resonators, with a particular focus on microscale optomechanical crystals. Then I will describe practical considerations to experiments utilizing optomechanical systems, and provide an overview of the different types of optical coupling methods that have been used for similar types of chip-based optical resonators.

1.1 Radiation Pressure

Radiation pressure, the exertion of a force upon the reflection of light from an object, is an intriguing concept with a long history. First proposed by Kepler in the 17th century as a possible explanation for the directionality of comet tails in opposition to the sun [1], the effect was eventually codified into Maxwell's full treatment of electromagnetism [2] and later included in Einstein's formulation of special relativity [3]. Following initial experimental observations of the radiation pressure force [4, 5], Compton developed a full quantum mechanical theory in his X-ray scattering work [6]. Although fundamental to the understanding of light, for the following half century radiation pressure was regarded as a weak, perturbative effect in most contexts. As for the entirety of the field of optics, this consideration changed with the advent of the laser [7]. With the large, coherent optical powers made available by lasers, radiation pressure forces could be made significant and useful in such emerging applications as trapping of dielectric particles with optical tweezers [8] and laser cooling of resonant ions and atoms [9, 10].

In what would prove to be a groundbreaking experiment, Braginsky and colleagues measured radiation damping in a mechanical oscillator coupled to an optical resonator [11, 12]. To investigate the impact of this "optical spring" effect on measurements of extremely weak forces such as gravitational-wave deflection of test masses, Braginsky, Caves, and contemporaries developed a full framework for the limits imposed by quantum optical properties of light used as a probe [13–16]. The

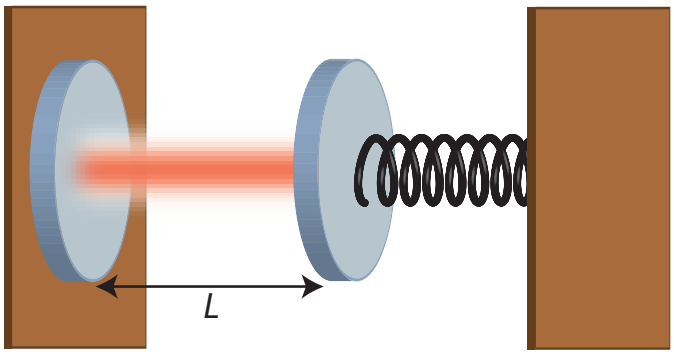

Figure 1.1: **Canonical Optomechanical System.** This example optomechanical system consists of a Fabry-Perot optical cavity formed from two high-reflectivity mirrors. One mirror is kept fixed, while the other is free to move with mechanical properties modelled in an effective spring force. Displacements of the movable mirror change the optical cavity length L, with a corresponding shift to the optical resonance frequency.

interest in systems with interacting optical and mechanical resonators (or optomechanical systems) extended with the development of micro- and nano-fabrication processes to mesoscopic objects, for which a plethora of applications is envisioned including fundamental studies of quantum mechanics, quantum information processing, and precision sensing of weak forces.

1.2 Optomechanical Devices

The canonical optomechanical system [12, 17] consists of a Fabry-Perot optical cavity, in which one of the end mirrors is mechanically compliant, as depicted by the spring-mounted mirror in Fig. 1.1. The motion of the movable mirror modulates the optical path length L of the Fabry-Perot cavity, and therefore changes the fundamental resonance frequency $f_o = c/2L$, where c is the speed of light. Thus for intracavity light with a particular wavelength, the mirror's motion imparts a shift in both the optical intensity and phase. Furthermore, since reflection of light from the mirror surface exerts a force due to radiation pressure, the intracavity optical field in turn modulates the mirror position.

These two processes, optical phase shifts due to mechanical motion and optical back-action on the mechanically-compliant object, form the backbone of the capabilities of optomechanical resonators. On the one hand, careful measurement of the optical phase shift makes an optomechanical resonator a superb sensor of the relative position of a moveable object. A detailed treatment and measurement of this application will be given in Chapter 3. On the other hand, optical back-action can be used to control the mechanical state of an object. This interaction can be selectively tuned to either drain thermal energy from the system, or to drive the mechanics into preferred states. In some instances, the mechanical motion can be driven into a self-oscillation regime, in which novel laser-like coherence is created in the acoustic field, as explored in Chapter 5.

For settings in which quantum mechanical energy levels are significant, control of the mechanical state can be utilized as a quantum memory or for translation and processing tasks in a hybrid quantum information network [18–26]. Progress towards realizing the quantum preparation and control of optomechanical resonators will be summarized in Chapter 4, and are treated in detail in the thesis dissertation of Seán Meenehan [27].

While the Fabry-Perot architecture shown in Fig. 1.1 has found applications in macroscale systems such as the Laser Interferometer Gravitational-Wave Observatory (LIGO) [28, 29] and at the mesoscale in the forms of reflective membranes [30, 31] and cantilever-mounted Bragg mirrors [32, 33], many groups in the field of optomechanics have turned to the microscale and nanoscale in an effort to increase the relative force of optomechanical interactions by reducing motional mass. Utilizing thin-film (< 500nm) microchip fabrication techniques, these optomechanical systems have been developed into many forms, ranging from capacitively-coupled LC resonators in the microwave domain [34–36] to visible/near-infrared (near-IR) optical whispering gallery mode structures [17] and optomechanical crystals [37, 38]. While each implementation features unique advantages and disadvantages, this work focuses exclusively on optomechanical crystals for their high degree of tailorability and ability to support large mechanical frequencies. Optomechanical crystals are structures featuring periodicity for both optical and acoustic waves, otherwise termed photonic and phononic crystals, respectively.

1.2.1 Photonic Crystals

Just as periodic electrical potentials in solids give rise to frequency-dependent dispersion and propagation of electrons [39], so do periodic index of refraction (N) variations create optical band structure [40]. The appropriate choice of lattice constant separation (a) between high- and low-n regions of such a photonic crystal creates destructive interference for light of wavelength $\lambda \approx a/2$. Effectively, this photonic crystal functions as a wavelength-specific mirror, as incoming optical waves at λ cannot propagate and must reflect (Fig. 1.2a). In further analogy with Fig. 1.1, optical cavities can be created by inserting a dielectric propagation region between two photonic crystal mirrors, as illustrated in Fig. 1.2b.

In this work, we fabricate quasi-1-dimensional photonic crystal cavities in silicon nanobeams of rectangular cross-section (Fig. 1.3). A 1-dimensional array of elliptical holes is etched into the longitudinal (x) direction of the nanobeam, while index confinement localizes the optical modes in the transverse (y and z) directions. The refractive index variation is then seen in Fig. 1.3a as $N_{\mathrm{Si}} = 3.48$, corresponding to the gray-shaded volume, while white regions represent air or vacuum with $N_{\mathrm{vac}} = 1$. To avoid optical scattering at the two end-mirror sections, both a and hole shape are adiabatically transitioned to a center defect, in which an optical mode at $\lambda = 1550$ nm is confined with high quality factor ($Q_{\mathrm{o}} > 10^5$).

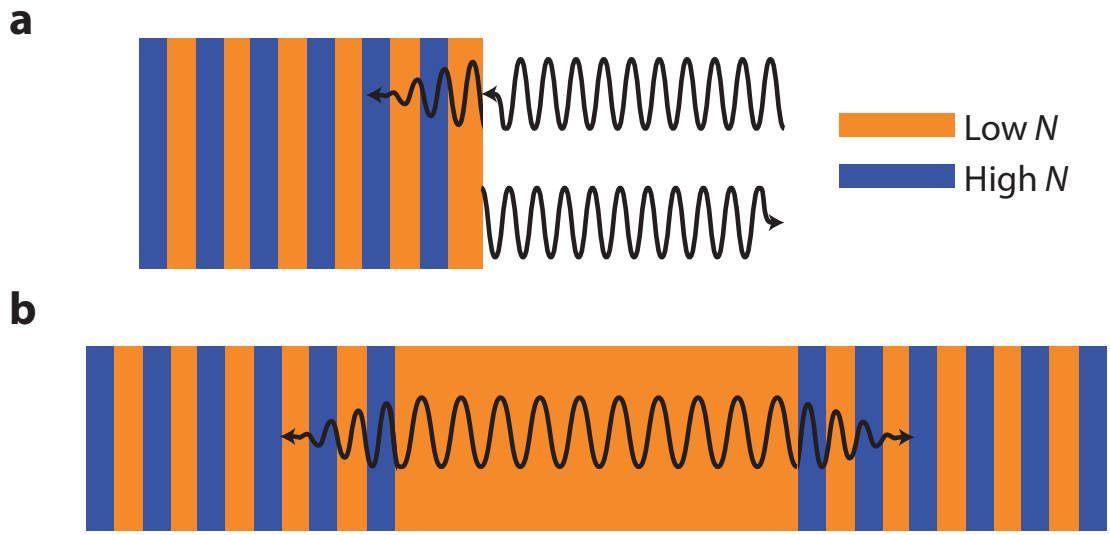

Figure 1.2: **One-Dimensional Photonic Crystal.** **a** Photonic crystal mirror illustration, with high and low index of refraction indicated by purple and orange, respectively. **b** Photonic crystal Fabry-Perot-type cavity illustation.

Another type of optomechanical device used in this work is the double-nanobeam, or zipper cavity (Fig. 1.4). The zipper cavity is usually formed from silicon nitride (Si_3N_4) for its mechanical properties, and consists of two nanobeams placed side-by-side in y. For sufficiently small air-slot separations of the nanobeams, the single-beam modes hybridize into coupled modes shared between both beams with a large optical intensity in the air slot.

1.2.2 Phononic Crystals

Due to the difference between the speed of light ($c/N \approx 10^8$ m/s) and the speed of sound ($v_s \approx 8.5 \times 10^3$ m/s) in a dielectric medium such as silicon, periodicitity on the order of near-IR optical

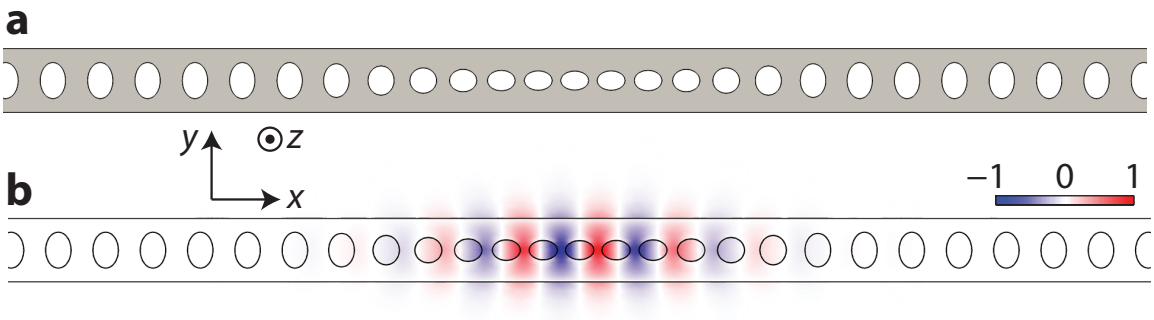

Figure 1.3: **Nanobeam Photonic Crystal.** **a** Geometry. **b** Finite-Element-Method (FEM) simulation of the normalized electric field in the y direction (E_y).

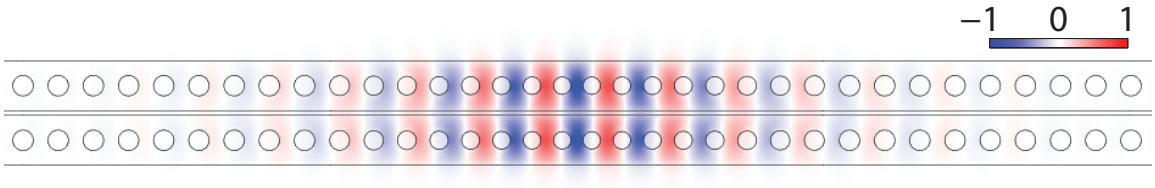

Figure 1.4: **Zipper Photonic Crystal. a** Geometry. **b** Finite-Element-Method (FEM) simulation of the normalized electric field in the y direction (E_y).

wavelengths corresponds to acoustic frequencies on the order of GHz. The nanobeam photonic crystal is designed such that the end-mirror sections function as acoustic reflectors at $\omega_m/2\pi = 3$ GHz or 5 GHz, while the center defect again confines an acoustic vibrational mode to a similar volume as the optical mode. This localized vibration, termed a breathing mode for its lateral deformation effect, is shown in a finite element method (FEM) simulation in Fig 1.5.

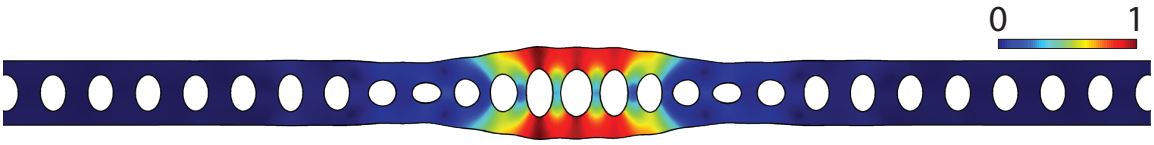

Figure 1.5: **Nanobeam Phononic Crystal.** FEM simulation of normalized displacement of the nanobeam fundamental breathing mode, showing both the magnitude corresponding to the colorbar and the deformed structure (not-to-scale).

While the nanobeam phononic crystal effectively confines the acoustic breathing mode, the mechanical band-gap only exists for modes which are symmetric in the y and z directions [41]. Although the optical band-gap is similarly not a full 3-dimensional gap, the mechanical band-gap is crossed by many more modes of different symmetries. Imperfections in fabrication can then couple these modes of different symmetry to the cavity breathing mode, causing acoustic loss through the phononic crystal end-mirrors. In order to keep acoustic vibrations from rapidly radiating out of the nanobeam, a secondary phononic crystal is added between the ends of the nanobeam and the supporting silicon wafer substrate. This phononic crystal featuring cross-shaped holes (Fig.1.6) supports a fullly 3-dimensional acoustic band-gap at the mechanical mode frequency of interest. It therefore acts as a radiation shield for the breathing mode, and raises the quality factor of the mechanical oscillator to $Q_m > 10^4$ at cryogenic temperatures.

The zipper cavity is not designed to function as a phononic crystal, but rather features an Euler-Bernoulli-type bending mode of the entire beam length (Fig. 1.7). With the appropriate choice of beam length and specific clamping conditions, this fundamental bending mode can occur over a wide frequency range of 1 kHz $< \omega_m/2\pi <$ 15 MHz.

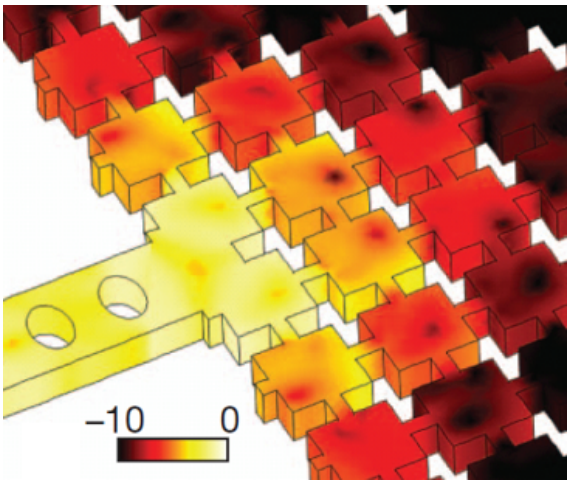

Figure 1.6: **Phononic Crystal Radiation Shield.** Reprinted by permission from Macmillan Publishers Ltd: Nature [42], copyright 2011. FEM simulation of displacement of the phononic crystal radiation shield, confining phonons which propagate out of the nanobeam to reflect back into the device.

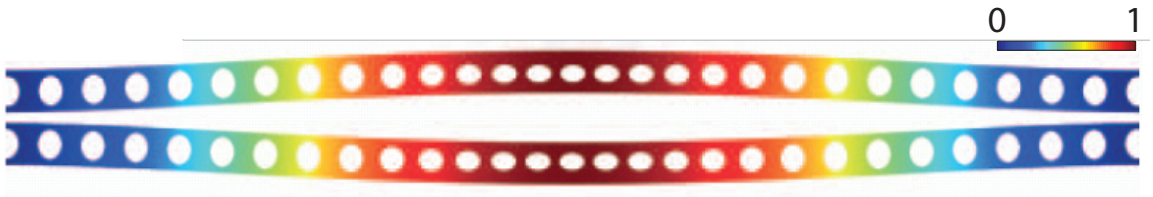

Figure 1.7: **Zipper Mechanical Oscillator.** FEM simulation of displacement of a zipper resonator fundamental bending mode (not-to-scale).

1.2.3 Optomechanical Coupling

While the previous sub-sections describe how the fundamental optical and mechanical modes of nanobeams are co-localized to a center defect, the remaining component of the optomechanical system is a coupling between these fields. Just as the length change in the Fabry-Perot optomechanical system (Fig. 1.1) effects the resonance condition of the cavity, so must the nanobeam acoustic breathing mode modulate the resonance frequency ω_o of the nanobeam optical cavity. This resonance shift is parameterized by the optomechanical coupling constant $g_{OM} = d\omega_o/dx$, where the x variable represents a general displacement coordinate.

For the case of the Fabry-Perot cavity, g_{OM} simply reduces to the ratio ω_o/L as the mirror motion directly shifts the fundamental resonance frequency. For the nanobeam optomechanical crystal however, the optomechanical coupling takes place through an intermediary shift in the index of refraction, specifically in the effective permittivity ε given by the distribution of silicon and air in the optical mode volume. As the breathing mode vibration deforms the structure, ε is shifted by

the moving boundaries [43] between silicon and air as well as the photoelastic effect caused by strain in the dielectric [44]. The optomechanical coupling is then given by a combination of the moving boundary and photoelastic effects [45].

For the optomechanical systems in this work, numerical FEM optimization of the device geometry was used to maximize $g_{\rm OM}$. Specific optimization of the photoelastic effect gives the largest $g_{\rm OM}$ for the nanobeam optomechanical crystal, while the value of $g_{\rm OM}$ for the zipper cavity is predominantly due to the moving dielectric boundaries of the slot separation between the two beams.

Scaling of the optomechanical coupling constant by the zero-point motion of the mechanical resonator is often a useful quantity for quantum regime optomechanics. The optomechanical coupling rate of photons to phonons, and the optical resonance frequency shift due to zero-point motion of the acoustic resonator, is $g_0 = x_{\rm ZPF} g_{\rm OM}$, where $x_{\rm ZPF} = \sqrt{\hbar/2m_{\rm eff}\omega_{\rm m}}$ is the zero-point displacement amplitude of a mechanical oscillator with effective motional mass $m_{\rm eff}$, with $\hbar$ representing Planck's constant. Parametric enhancement of this interaction by coupling $n_{\rm c}$ photons into the optical cavity is then incorporated into the linearized coupling strength $G = g_0\sqrt{n_{\rm c}}$.

In the full quantum mechanical treatment of an optomechanical resonator, the parametric coupling of motion to the optical cavity adds an interaction term to the self-energy Hamiltonians of the oscillators, and the full system Hamiltonian is

$$\hat{H}_{\rm tot} = \hbar\omega_{\rm c}\hat{a}^\dagger\hat{a} + \hbar\omega_{\rm m}\hat{b}^\dagger\hat{b} + \hbar g_0\hat{a}^\dagger\hat{a}(\hat{b}+\hat{b}^\dagger), \tag{1.1}$$

where $\hat{a}$ and $\hat{b}$ are the annihilation operators for the optical and acoustic, field respectively. The reference frame of the system is often rotated at the frequency of a probe laser $\omega_{\rm l}$, which is detuned from the optical resonance by $\Delta \equiv \omega_{\rm c} - \omega_{\rm l}$, in order to describe the time evolution of the optical and acoustic fields by the quantum Langevin equations [46]:

$$\dot{\hat{a}} = -\Big(i\Delta + \frac{\kappa}{2}\Big)\hat{a} - ig_0\hat{a}(\hat{b}+\hat{b}^\dagger) - \sqrt{\kappa_{\rm e}}\hat{a}_{\rm in}(t) - \sqrt{\kappa_{\rm i}}\hat{a}_{\rm in,i}(t), \tag{1.2}$$

$$\dot{\hat{b}} = -\Big(i\omega_{\rm m} + \frac{\gamma}{2}\Big)\hat{b} - ig_0\hat{a}^\dagger\hat{a} - \sqrt{\gamma_{\rm i}}\hat{b}_{\rm in}(t). \tag{1.3}$$

The last two terms of Eqn. 1.2 include an input laser probe field to the optical cavity $\hat{a}_{\rm in}$ and a vacuum noise field $\hat{a}_{\rm in,i}$, as required by the fluctuation-dissipation theorem. The mechanical resonator couples to environmental degrees of freedom determined by surrounding thermal baths parameterized by $\hat{b}_{\rm in}$ at the intrinsic mechanical decay rate $\gamma_{\rm i}$. The rates κ and γ pertain to the total energy decay rate of the optical and mechanical resonators, respectively, while $\kappa_{\rm e}$ is the optical coupling rate to a measurement channel.

For systems like the optomechanical resonators in this work, where $g_0 \ll \kappa$ (the weak-coupling limit), the approximation that the probe is dominated by a large coherent optical intensity with

a small quantum noise compenent, i.e., transforming $\hat{a} \rightarrow \alpha_0 + \hat{a}$, allows Eqns. 1.2 and 1.3 to be linearized and Fourier transformed to

$$\hat{a}(\omega) = \frac{-\sqrt{\kappa_\mathrm{e}}\hat{a}_\mathrm{in}(\omega) - \sqrt{\kappa_\mathrm{i}}\hat{a}_\mathrm{in,i} - iG(\hat{b}(\omega) + \hat{b}^\dagger(\omega))}{i(\Delta - \omega) + \kappa/2}, \tag{1.4}$$

$$\hat{b}(\omega) = \frac{-\sqrt{\gamma_\mathrm{i}}\hat{b_\mathrm{in}}(\omega)}{i(\omega_\mathrm{m} - \omega) + \gamma_\mathrm{i}/2} - \frac{iG(\hat{a}(\omega) + \hat{a}^\dagger(\omega))}{i(\omega_\mathrm{m} - \omega) + \gamma_\mathrm{i}/2}. \tag{1.5}$$

Regrouping of terms in Eqn. 1.5 produces renormalized mechanical frequency $\omega_\mathrm{m}' = \omega_\mathrm{m} + \delta\omega_\mathrm{m}$ and loss rate $\gamma = \gamma_\mathrm{i} + \gamma_\mathrm{OM}$, with

$$\delta\omega_\mathrm{m} = |G|^2 \mathrm{Im}\left[\frac{1}{i(\Delta - \omega_\mathrm{m}) + \kappa/2} - \frac{1}{-i(\Delta + \omega_\mathrm{m}) + \kappa/2}\right], \tag{1.6}$$

$$\gamma_\mathrm{OM} = |G|^2 \mathrm{Im}\left[\frac{1}{i(\Delta - \omega_\mathrm{m}) + \kappa/2} - \frac{1}{-i(\Delta + \omega_\mathrm{m}) + \kappa/2}\right]. \tag{1.7}$$

For resonators where the mechanical modulation sidebands are well-resolved in the optical spectrum (referred to as the sideband-resolved regime of $\kappa \ll \omega_\mathrm{m}$), the optomechanical damping approximates to $\gamma_\mathrm{OM} = \pm 4G^2/\kappa$ for laser detunings of $\Delta = \pm\omega_\mathrm{m}$, respectively. This dynamical back-action, in addition to damping or stiffening the mechanical oscillator, modifies the average phonon occupancy $\langle n \rangle = \langle \hat{b}^\dagger \hat{b} \rangle$ from the unperturbed occupancy n_th determined by its contact with an environmental thermal bath, with

$$\langle n \rangle|_{\Delta=\omega_\mathrm{m}} = \frac{\gamma_\mathrm{i} n_\mathrm{th}}{\gamma} + \frac{\gamma_\mathrm{OM}}{\gamma}\left(\frac{\kappa}{4\omega_\mathrm{m}}\right)^2, \tag{1.8}$$

$$\langle n \rangle|_{\Delta=-\omega_\mathrm{m}} = \frac{\gamma_\mathrm{i} n_\mathrm{th}}{\gamma} + \frac{|\gamma_\mathrm{OM}|}{\gamma}. \tag{1.9}$$

Driving the system with a red-detuned laser optomechanically cools the mechanical motion analogously to laser cooling of atomic and ionic ensembles [9, 10], and blue-detuned driving amplifies the mechanics. A great deal of interest and effort [42, 47–51] has focused on the cooling process of Eqn. 1.8, since reducing $\langle n \rangle$ to below 1 is difficult to achieve through passive cryogenic control of n_th (requiring both GHz mechanical frequencies and millikelvin envorionments as in Ref. [52]), yet is an important prerequisite of utilizing optomechanical resonators as testbeds for quantum experiments [20, 21, 23, 25, 26, 35, 52–60]. When $\Delta = 0$, there is no dynamical back-action and the only optical forces on the mechanical oscillator are due to phase or intensity noise carried by the laser probe. This is the regime of interest for presicision displacement and force sensing [14, 16, 34, 61–64], as the mechanical oscillator is minimally perturbed by the measurement while its motion strongly modulates the cavity resonance, and thereby the phase of the resonant optical probe.

1.3 Experimental Considerations to Optical Coupling Schemes

While the implementions of optomechanical systems as testbeds for quantum experiments and for classical metrology vary widely in application, a common feature of these experiments is a critical reliance on robust and efficient experimental access to the resonator. This section will describe the pertinent challenges to optically coupling to microscale optomechanical resonators.

A Scanning Electron Microscope (SEM) image of a fabricated nanobeam optomechanical crystal is shown in Fig. 1.8. Each nanobeam is referred to as a device, while arrays of hundreds to thousands of devices are formed in the thin (220 nm) silicon film layer of a silicon-on-insulator (SOI) microchip. This millimeter scale chip is also referred to as a sample.

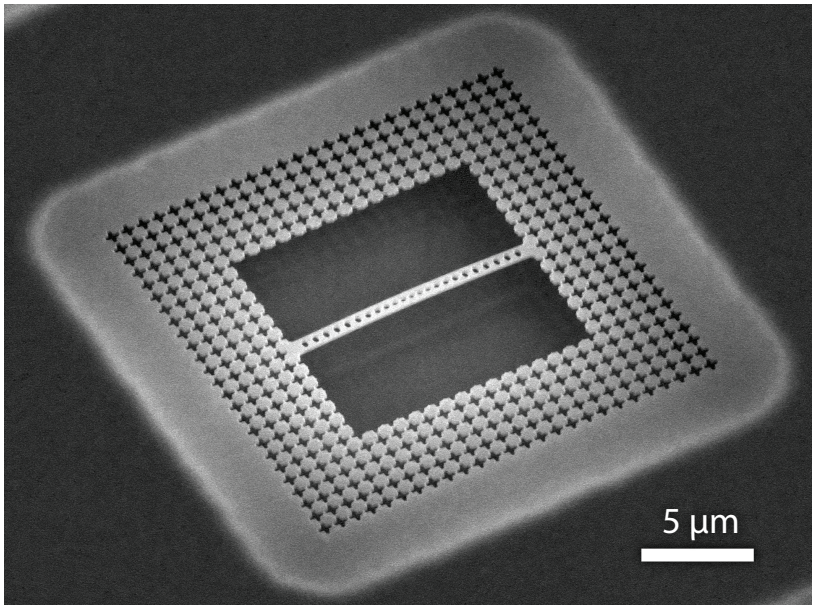

Figure 1.8: **Fabricated Nanobeam Optomechanical Crystal Device.** Reprinted by permission from Macmillan Publishers Ltd: Nature [42], copyright 2011. Scanning electron microscope (SEM) image of a nanobeam optomechanical crystal.

Typical optomechanics experiments involve preparation of an optical probe, such as the generation of laser light of a particular wavelength, power, and linewidth, which is then coupled into a single device on a sample. This light resonates in the optical cavity until it is collected in a detection channel, manipulated specifically for a given measurement, and photodetected for spectroscopy or other signal analysis. The choice of device optical wavelength of $\sim$1550 nm allows for the use of high-quality, easily commercially available optical instruments due to heavy utilization in the telecommunications industry. These components can be linked by high-efficiency, low-dispersion optical fibers, further simplifying experimental setups in comparison to alignment sensitive free-space propagation.

However, while commercial equipment may feature fiber-optic input/output ports, custom fabricated nanobeam samples do not. The coupling and collection of light into and out of a microscale resonator is a challenging task to meet, especially under certain constraints such as efficiency and cryogenic compatibilty.

1.3.1 Mechanical Compliance

Unlike travelling elastic modes such as surface and bulk acoustic waves, the nanobeam and zipper mechanical modes require the structure to be suspended, with the only substrate clamping points located on the ends of the beam (Fig. 1.8). This is accomplished in fabrication by first etching the nanobeam into the top silicon device layer of an SOI chip, and then selectively etching the buried oxide ($3\,\mu$m thick SiO_2) locally underneath the device. For Si_3N_4 zipper devices, a selective Si etch is used in this undercutting procedure.

An optical coupling method that impedes mechanical compliance, either through physical contact of an object to the device or through adverse modifications in device design, can severely degrade the performance of the optomechanical resonator. Such outcomes can include reductions of g_{OM} and Q_{m}, as well as mode-mixing of the fundamental acoustic mode with other undesirable modes of the structure. Furthermore, while device geometry modifications may be desirable in aiding optical coupling, care must be taken that they are compatible with the fabrication processes, most notably in the undercut procedure.

1.3.2 Optical Loss

While small ($\sim$1 nm scale) geometrical imperfections arising during fabrication cause an unavoidable amount of parasitic loss of light in the resonator, the optical coupling method should be as loss-less as possible. Any amount of light that interacts with the acoustic mode but is not detected in the experimental setup represents lost information about the mechanics [61]. Inefficiencies in optical coupling thus limit both the ultimate sensitivity of the optomechanical resonator as a precision sensor as well as for applications in quantum information.

Optical coupling loss can be decomposed into two effects: intrinsic and extrinsic loss. Intrinsic loss refers to the aforementioned parasitic scattering, where structural deformities cause light to reflect and scatter out of the structure before being routed to a detection port. Another source of scattering lies in imperfect mode-matching between a coupler element and the optical cavity. Just as impedance mismatches in electrical circuits cause adverse signal reflection and power drain, junctions in an optical coupler where the supported mode profiles have different size or shape will scatter or reflect light into free space or other undetectable modes of the structure.

Extrinsic loss is a necessary outcome of experimental access to a device. Light that is coupled out

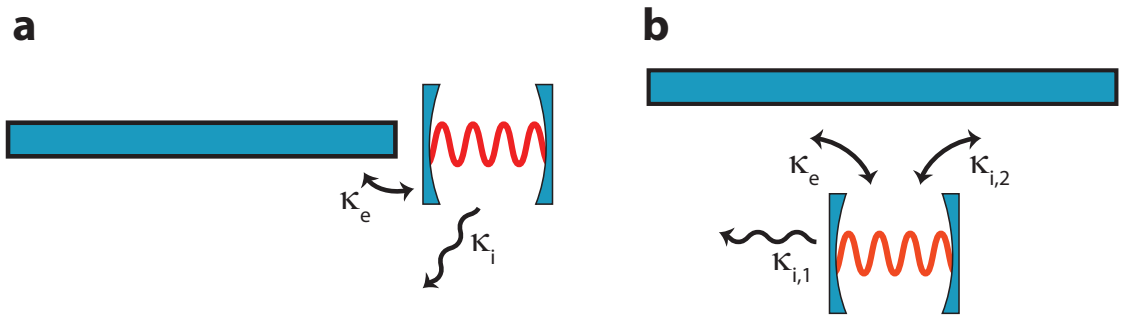

Figure 1.9: **Extrinsic coupling channels.** Illustrations of coupling schemes featuring **a** one and **b** two output channels.

of the cavity into a detection channel for measurement is still lost light with respect to the cavity. In the measurement sense, extrinsic loss is not really loss at all, and indeed it is often desirable to have large amounts of extrinsic loss in an experiment to produce large signals. However, detection channels can produce loss for particular coupling architectures as well as practical experimental limitations. Ideally, a coupling scheme will collect all of the light radiating from the resonator (excepting the intrinsically scattered light) and route the optical signal through a single detection channel to an experimental setup. However in some couplers, cavity radiation can escape into two or more channels (Fig. 1.9b), perhaps even in equal proportion. Even if the output of every channel could be collected efficiently, the optical signals could not be accurately recombined since each channel will have a different optical delay. Individual measurement of each output channel would require separate detection apparatuses, which is impractical due to complexity and cost of equipment. Thus in practice only one detection channel is used in an experiment, whereas light routed into the other output channels is regarded as intrinsic loss.

Throughout this work, optical loss will be quantified as a loss rate in radians/s units. Intrinsic and extrinsic loss rates will respectively take the symbols κ_i and κ_e, while total loss rate $\kappa = \kappa_\mathrm{i} + \kappa_\mathrm{e}$.

1.3.3 Cryogenic Compatibility

For applications of an optomechanical crystal in hybrid quantum information networks, quantum-scale amplitudes of mechanical vibration must be significant in comparison to thermal vibration amplitudes. Quantization of an acoustic field produces sound particles, or phonons, each with energy $\hbar\omega_\mathrm{m}$, where $\hbar$ is Planck's constant. Phonons are quasiparticles with boson properties, and therefore their thermally generated population n_th follows the Bose-Einstein distribution

$$n_\mathrm{th} = \frac{1}{e^{\hbar\omega_\mathrm{m}/k_\mathrm{b}T} - 1}, \tag{1.10}$$

where k_b is Boltzmann's constant and T is the temperature of the mechanical oscillator.

Initial proposals for quantum state engineering using optomechanical devices call for the generation of nonclassical mechanical states using light. One of the simplest such states is the single phonon Fock state, in which exactly one phonon occupies the mechanical oscillator. A necessary condition to generate this state is $n_\mathrm{th} \ll 1$, such that the oscillator is empty of phonons, and approaches its quantum ground state, before generation of the Fock state. For an oscillator with $\omega_\mathrm{m}/2\pi = 5\,\mathrm{GHz}$, the ground state condition is equivalent to $T \ll 350\,\mathrm{mK}$ through Eqn. 1.10.

In recent years several research groups have realized $n_\mathrm{th} < 1$, either through a combination of cryogenic pre-cooling to intermediate temperatures followed by optomechanical cooling [42, 50], or through purely cryogenic cooling with a sufficiently low-temperature system [52]. While significant progress has been made towards cooling to the ground state from room temperature [65–67], these experiments have not yet reached $n_\mathrm{th} < 1$. Therefore the preparation of an optomechanical resonator in its quantum ground state requires the sample to be located in a cryogenic system with optical coupling to a room-temperature experiment apparatus. This optical coupling can present a challenge for certain cryogenic coolers, since features such as optically transparent windows and motion controllers for alignment require specialized instrumentation to avoid significant blackbody or Joule heating at sub-Kelvin temperatures.

1.4 Optical Coupler Technologies

The optomechanical resonators utilized in this work take the form of nanoscale to microscale microchip devices. While this architecture offers a number of significant benefits, such as sophisticated fabrication processes, large-scale integrability, and a high degree of tailorability, a fundamental challenge lies in the efficient coupling of light from the chip-based device to conventional optical manipulation elements such as lenses, mirrors, and fibers. In particular, the sub-wavelength optical mode volumes ($\sim \lambda^3/8$) of the photonic crystals used here cannot mode-match to diffraction-limited components (with spot dimensions much greater than $\lambda/2$ in practice) without sustaining a large loss of optical power. Furthermore, many of the techniques that can efficiently mode-match do not meet the other mechanical compliance and cryogenic compatibility criteria of the previous section.

1.4.1 Free-Space Reflection

One of the simpler methods of coupling to microscale devices is to focus a free-space laser beam through a high numerical aperture objective lens onto the chip. With sufficient alignment to the optical mode volume of the device, light couples into the optical cavity and resonates for a characteristic time determined by Q_o before scattering out of the device. A portion of this light is scattered into the angle subtended by the focusing lens, and is collected for detection in the test setup.

A significant limitation of the free-space reflection method is the size and shape of the laser beam spot on the chip. While the ultimate diffraction limit of $\lambda/2 = 775\,\text{nm}$ is comparable to the dimensions of the device mode volume, non-ideal numerical aperture and flaws in the microscopy system usually limit the achievable beam diameters to $\approx 2\,\mu\text{m}$ [68]. This large spot size, in combination with differences in mode shape between the circular laser beam cross section and the nanobeam mode profile (in both near- and far-field), causes poor mode-matching and low optical transmission between the device and the collection lens. For experiments relying on high efficiency of detection, free-space coupling will likely produce unacceptable levels of optical loss.

1.4.2 Grating Couplers

Since the primary source of optical loss in free-space coupling lies in mode-mismatch, an intermediate mode converter element can significantly improve transmission efficiency. Such a mode converter will mode-match to a free-space optical beam on the input, transform the mode size and shape, and mode-match to the optical cavity on the output. A common mode converter is the grating coupler, in which a photonic crystal on the sample surface diffracts an incoming optical beam (with a particular angle of incidence) into the $x-y$ plane of the device layer [69, 70]. Appropriate design of the grating coupler can provide highly efficient coupling.

One of the qualities enabling high efficiency in grating couplers is the use of destructive interference in the sample substrate to directionalize the device output into the same mode as the input beam. This broken symmetry property reduces extrinsic loss, as output into other z directions is eliminated. However, mechanically-compliant optomechanical structures make this directionalization difficult, since removal of the buried oxide layer restores z-symmetry. The cavity radiation then has two symmetric output channels, causing at least 50% loss in collection. While some sophisticated substrate-less grating designs and fabrication processes can produce high-efficiency coupling [71], many suspended grating couplers feature significantly higher losses at levels of 90 % [72]. While modifications in fabrication processes could enable a grating coupler to be substrate-supported for an optomechanical device, these processes have not yet been developed and could prove problematic.

Another issue for grating couplers is the width of the wavelength pass-band, which can be quite narrow for certain coupler designs. Since fabrication imperfections and non-reproducibility cause uncertainty in realized optical cavity wavelengths, imperfect matching of wavelengths between the device and the coupler can add complexity and optical loss.

1.4.3 Fiber-Taper Couplers

An elegant method that circumvents the challenges of mode-matching is the evanescent coupling of the optical cavity to a waveguide such as an optical fiber [73, 74]. By tapering the diameter of a

standard optical fiber to less than a wavelength, a significant fraction of the guided optical mode will propagate in the surrounding air. This extended mode then forms a coupled mode with the optical cavity resonance when placed in the near field of the chip-based device [75]. Further tuning of the fiber placement can produce high-efficiency ($> 90\,\%$) coupling and collection [76], as well as provide in-situ control over κ_e.

Fiber-taper couplers have proved to be extremely useful for a range of measurements with photonic crystal nanocavities [74–76] , whispering-gallery-mode resonators [77, 78] , and optomechanical crystals [37, 38, 42, 79–81]. This method is not without its drawbacks though, as operation in cryogenic environments is possible but difficult.

To achieve stable coupling with large κ_e, a small dimple impression on the tapered fiber [77] is brought into physical contact with an optimal position on top of the optomechanical resonator. The performance of this "taper touch" is extremely senstive to position, since the contact of the glass fiber can cause large amounts of optical scattering and mechanical damping. The process of establishing the touch thus requires feedback from an imaging system integrated into the cryogenic chamber. This has been achieved in past work with optically transparent viewports in a helium-flow cryostat, allowing imaging with a microscope objective lens. Other systems, such as dilution refrigerators, are less accomadating to viewport access and require filtered window ports with infrared imaging to avoid heating from room-temperature photons. For experiments in which pure cryogenic cooling to milliKelvin-domain temperatures is desirable, fiber-taper coupling may be very difficult and impractical.

Another drawback of fiber-taper couplers is that they are inherently two-sided (Fig. 1.9b), in the sense that two extrinsic output channels (two directions of fiber propagation) exist into which the cavity can radiate. While some structures such as whispering-gallery-mode resonators can be manipulated to provide destructive interference of one propagating output mode [82], the standing-wave nature of photonic crystals couples the cavity mode symmetrically into both output channels. Therefore even in the absence of parasitic scattering loss, the coupling efficiency is limited to $50\,\%$. Higher-efficiency coupling to a photonic crystal requires a truly one-sided coupling scheme.

Chapter 2

Fiber-Integrable Optomechanical Devices

This chapter will present the design, fabrication process development, and optical characterization of two coupling techniques optimized to meet the criteria described in Sec. 1.3. The discussions of device design cover aspects necessary to explain principle of operation, while further details can be found in Ref. [27]. Numerical simulations using finite-element method (FEM) are performed with COMSOL Multiphysics version 3.5 [83], and finite-difference-time-domain (FDTD) simulations are performed with Lumerical FDTD Solutions [84].

2.1 Silicon Nitride V-Groove

The premise of the V-groove coupler is to provide an on-chip optical fiber alignment feature [85, 86], which allows a fiber to couple to a device with high efficiency before being permanently fixed in place. This pre-alignment removes the need for in-situ fiber positioning and imaging in a cryogenic environment.

2.1.1 Device Design

The V-groove coupler design takes advantage of an anisotropic etch property of silicon, which allows V-shaped features to be defined by preferred crystal planes. For devices formed in silicon-nitride (Si_3N_4) films deposited on a silicon wafer, the device layer can act as a mask for the V-groove definition, allowing for a simple fabrication process.

The depth and wall-angle of the V-groove alignment feature determine the height at which an optical fiber (cladding diameter of 125 μm) will sit when placed in the groove. Appropriate choice of the groove dimensions places the center of the 9 μm diameter fiber core at the same height as the center of the 400 nm Si_3N_4 film. The fiber is cleaved to produce a flat-facetted tip from which the optical mode is launched towards a zipper device, as illustrated in Fig. 2.1. A mode-converter

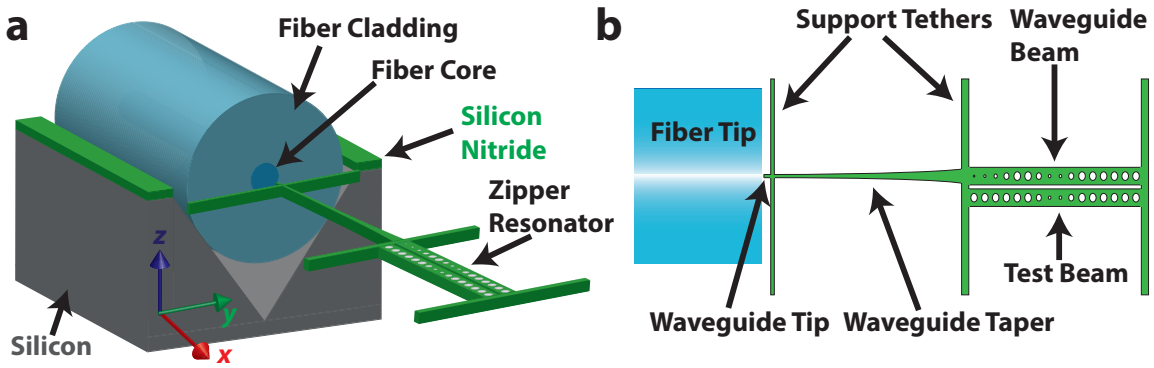

Figure 2.1: **V-Groove Fiber Coupler Illustration.** Not-to-scale illustration of a V-groove fiber coupled zipper device in **a** angled-view and **b** top-view perspective. The silicon nitride device layer is shaded green, while the silicon substrate is shaded gray for illustration. The 9 μm diameter optical fiber core is indicated by the dark blue center region, and the 125 μm diameter cladding is shaded light blue.

consisting of an adiabatically-tapered Si_3N_4 index waveguide [87–90] is used to mode-match the fiber-launched optical beam to the zipper device, into which the waveguided mode couples through a truncated photonic crystal mirror. Each of these optical coupling junctions is decribed in detail in the following sub-sections, in order corresponding to the propagation of light from the input optical fiber to the optomechanical resonator.

2.1.1.1 Waveguide Tip

An SEM image of a cleaved optical fiber (Corning SMF-28e) tip butt-coupled to a silicon nitride waveguide is shown in Fig. 2.2. The positioning of the fiber in the alignment groove feature aligns the glass fiber to the y and z position of the index waveguide tip, while the separation in x is kept below 10 μm.

Mode-matching between the Corning SMF-28e optical fiber and the Si_3N_4 waveguide tip is accomplished by determining the waveguide cross-section, which supports an evanescent field matching the 10.4 μm fiber mode-field diameter (Fig. 2.3a-c). The transmission efficiency through this junction is given by the mode overlap integral

$$\eta_{\text{overlap}} = \text{Re}\left(\frac{\int E_1 \times H_2^* \cdot dS \int E_2 \times H_1^* \cdot dS}{\int E_1 \times H_1^* \cdot dS \int E_2 \times H_2^* \cdot dS}\right), \tag{2.1}$$

where E and H are respectively the electric and magnetic fields of the optical modes supported by the fiber (subscript 1) and Si_3N_4 index waveguide (subscript 2). While the waveguide thickness is fixed at 400 nm, tuning of the waveguide width w_{tip} can be used to optimize Eqn. 2.1 via FEM simulation [83]. A width of $w_{\text{tip}} = 230$ nm is found to produce the optimal $\eta_{\text{overlap}} = 90$ % at the target wavelength of 1550 nm. The coupler is broadband in that η_{overlap} only decreases by 10 % over

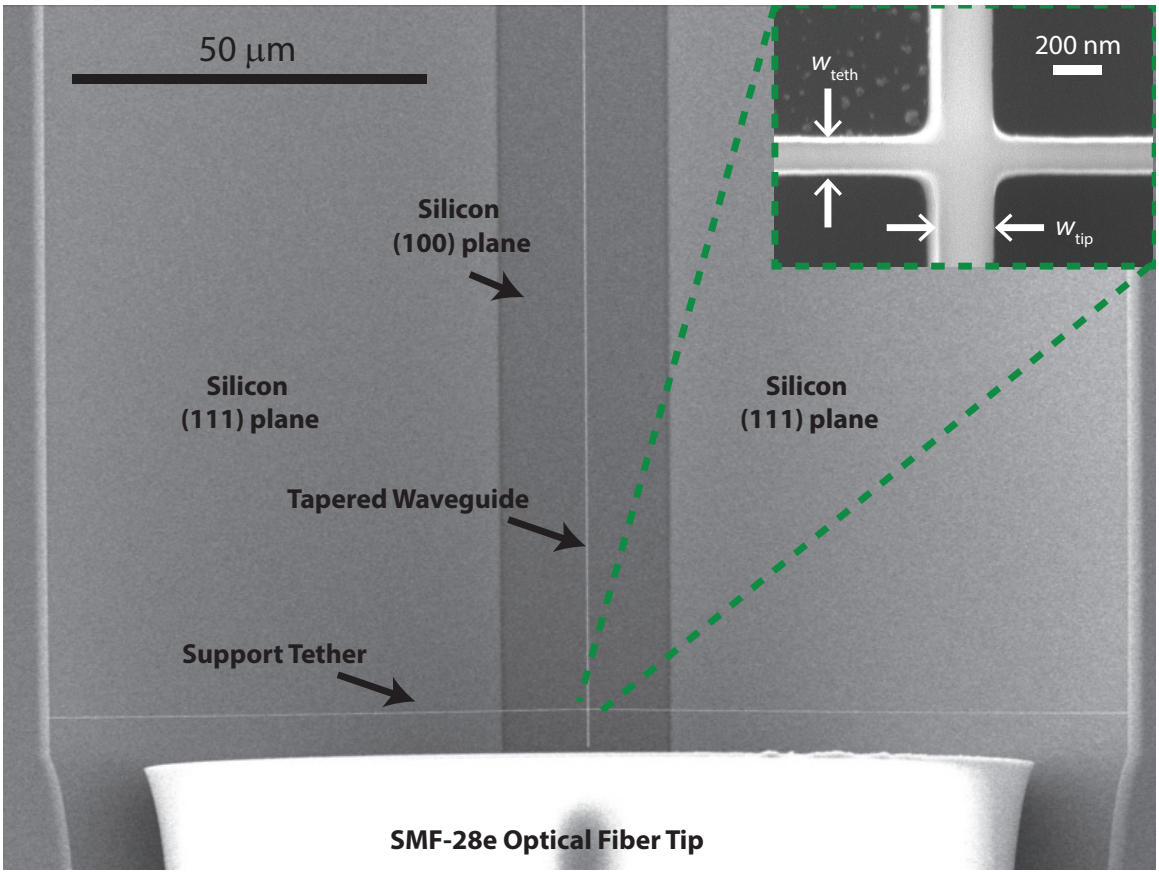

Figure 2.2: **Fiber to Nitride Waveguide Junction.** SEM image of an SMF-28e optical fiber resting in a V-groove, and butt-coupled to a silicon nitride waveguide tip. The curved image distortion at the bottom of the image is caused by electron beam deflections from the electrically-doped cladding of the optical fiber. The inset shows an SEM perspective of the silicon nitride waveguide at a distance 5 μm recessed from the waveguide tip, where it is anchored by a structural support tether spanning the length of the V-groove.

a 200 nm wavelength range (Fig. 2.3d), although the efficiency is strongly dependent on the realized width (Fig. 2.3e).

2.1.1.2 Support Tether

The length of the waveguide taper (described in the following sub-section) requires the tip to be anchored to the substrate to prevent bending (which would complicate fiber positioning and alignment). A tether feature spans the V-groove and fixes to the waveguide at a distance of 5 μm from the tip. Since the mode is significantly evanescent at this point, scattering at the tether junction causes optical loss. The amount of scattering depends strongly on the width of the tether feature, as shown in Fig. 2.5a. Tethers can be reproducibly fabricated at a width of 70 nm, producing loss of $\sim 5\,\%$.

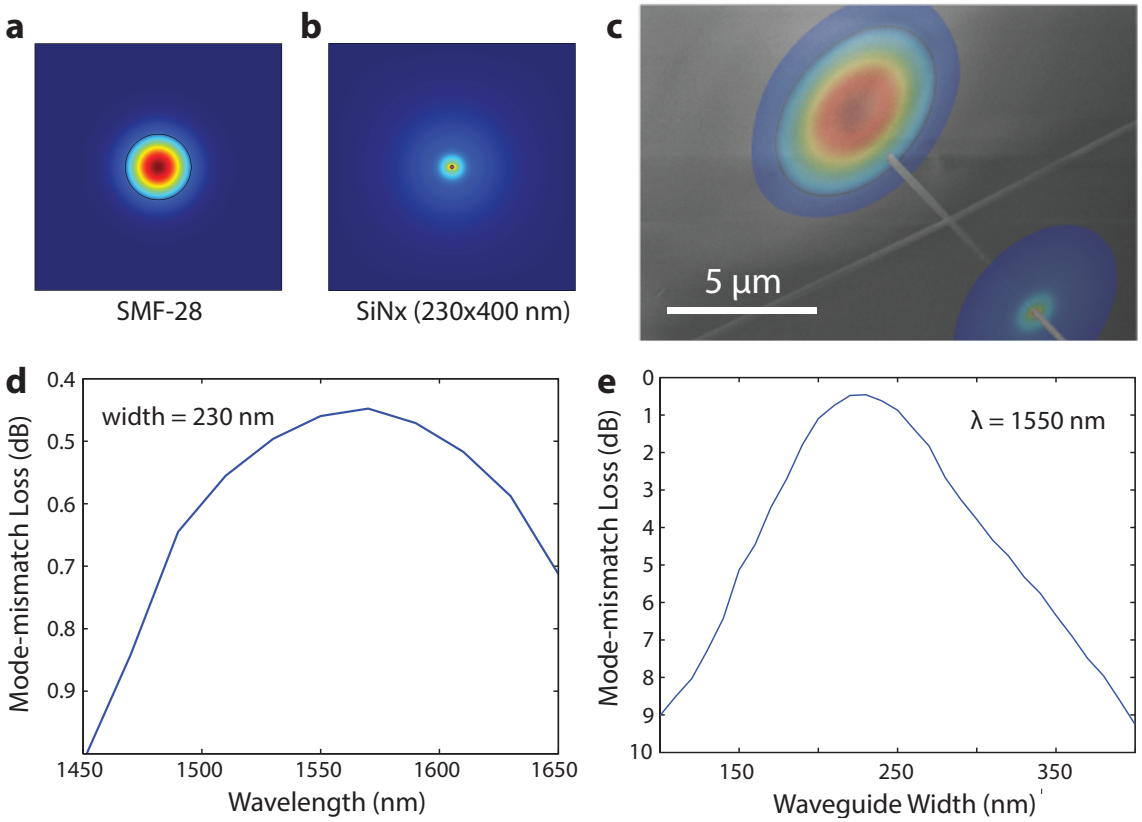

Figure 2.3: **Fiber-to-Waveguide Mode Matching.** FEM simulations E_y for the propagating optical mode of the **a** SMF-28e optical fiber and **b** silicon nitride waveguide tip. **c** Overlays of the simulations in **a** and **b** on an SEM image of a fiber-coupled device. **d** Simulated optical loss due to mode-mismatch as a function of wavelength for a 230 nm wide waveguide tip. **e** Optical loss at $\lambda = 1550$ nm as a function of waveguide tip width.

2.1.1.3 Waveguide Taper

As the optical mode propagates along the silicon nitride waveguide (in direction x), the waveguide gradually widens from the tip width of $w = 230$ nm to a zipper nanobeam width of $w = 850$ nm. This has the effect of confining the optical mode in the dielectric to a mode profile similar to the fundamental optical resonance of the zipper cavity. To accomplish this mode conversion efficiently, an adiabaticity condition

$$\frac{dw}{dx} \ll |n_{\mathrm{eff,i}} - n_{\mathrm{eff,j}}|, \qquad \forall i \neq j, \tag{2.2}$$

is enforced, where $n_{\mathrm{eff,i}}$ is the effective refractive index for an arbitrary waveguide mode. This condition ensures that light in the preferred optical mode does not couple to other modes of the structure, which could cause loss both in propagation and in coupling to the zipper resonance. Finite-difference time-domain (FDTD) simulations of the waveguide show that the adiabatic condition for this device is best met when w as a function of x expands as a polynomial of order 3 or greater, as

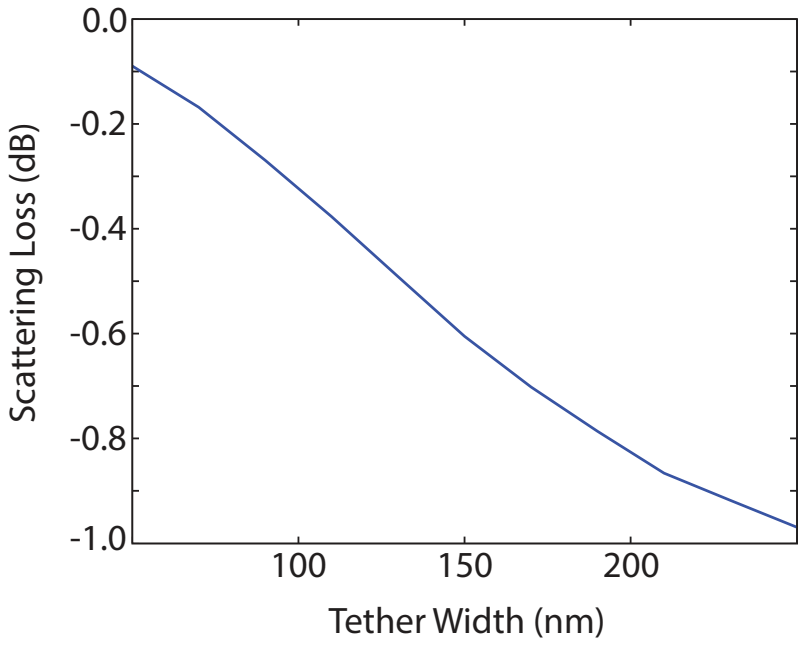

Figure 2.4: **Waveguide Support Tether.** Finite-difference-time-domain (FDTD) simulation of optical transmission loss at the waveguide tip support tether.

shown in Fig. 2.5b. By making the total length of this waveguide taper greater than 300 μm, the optical loss in the mode conversion can be kept below 10 %. The waveguide mode converter used in this work is a 400 μm long, cubic waveguide taper with simulated loss of < 10 %.

2.1.1.4 Damping Tethers

In order to prevent mechanical bending modes of the waveguide from coupling to and mixing with the nanobeam bending modes of the zipper resonator, a series of tethers is used to secure the waveguide after the 400 μm taper section (Fig. 2.6). The tethers are supported by large sections (50 μm$\times$50 μm) of silicon nitride membrane plates to add stiffness and mechanical damping to this junction. The set of support tethers span a 40 μm distance between the plates, clamping the waveguide beam in between. To reduce optical scattering from the tethers, the waveguide is temporarily widened to 1.5 μm at this point, which confines the optical mode enough that negligible amounts of field encounter the tethers. As the optical mode is already concentrated in the dielectric at the beam waveguide width $w = 850$ μm, the cubic widening to 1.5 μm takes place over a propagation distance of 10 μm while still meeting the adiabatic condition of Eqn. 2.2. The mode then encounters 15, 150 nm wide tethers with a simulated transmission efficiency of 98.8 %. The waveguide is then tapered down to a width of 850 nm for coupling to the optomechanical zipper resonator, again cubically over a distance of 10 μm.

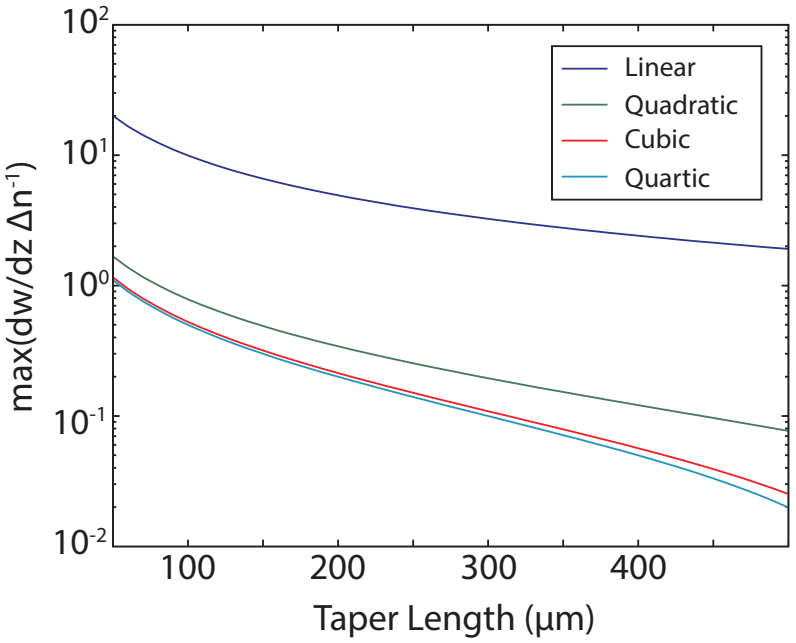

Figure 2.5: **Waveguide Taper.** Finite-difference-time-domain (FDTD) simulation of optical transmission loss of the waveguide taper due to coupling into other wavedguide modes. Waveguides expanding linearly, quadratically, cubically, and quartically with x propagation are simulated, with best results obtained for cubic and higher order polynomial taper shapes.

2.1.1.5 Photonic Crystal Taper

After the mode is confined at the zipper nanobeam width, light couples into the zipper resonance through a truncated photonic crystal mirror, as shown in the example SEM image of Fig. 2.7a and the FEM-simulated optical mode profile of Fig. 2.7b. An analogy to this feature is a conventional mirror with reflectivity $R < 1$, which weakly transmits light. The photonic crystal mirror reflectivity is reduced slightly by removing a certain number of holes, which allows light to tunnel through the mirror despite the optical band gap. In another measure to reduce loss, the index waveguide is transitioned to the photonic crystal mirror by introducing holes of linearly increasing radius. A series of $6 - 8$ such photonic crystal taper holes is sufficient to enable transmission of > 95 % in simulation. The first introduced hole has diameter of 50 nm, and the following holes expand linearly to match the nominal nanobeam mirror hole of height 380 nm and width 300 nm.

2.1.1.6 Zipper Resonator

Finally, the optical mode enters the cavity, with a shared defect mode between the nanobeam connected to the waveguide mode converter and a second near-field nanobeam. One of the tether-support membranes is also used as a support for the second zipper resonator nanobeam, which spans from the curved membrane section to the end of the V-groove (Fig. 2.15b). This nanobeam

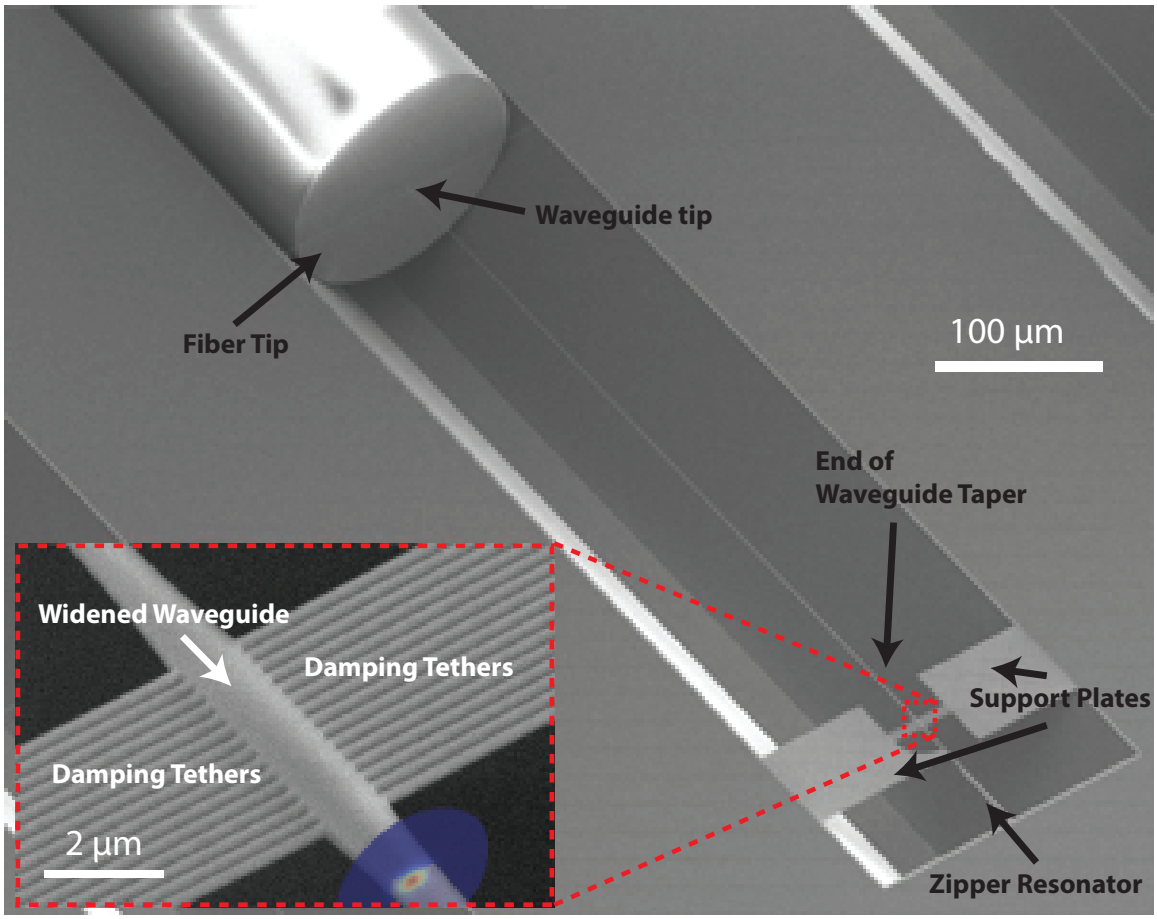

Figure 2.6: **Damping Tethers.** SEM image of a fiber-coupled device. The inset shows a detailed view of the set of 15, 150 nm support tethers spanning the two silicon nitride membrane plates and clamping the waveguide at the end of the taper region.

is later referred to as the test beam of the zipper resonator, as the experiment described in Chapter 3 uses the V-groove coupled waveguide structure as an optomechanical probe of the motion of the test beam. The nanobeams are separated by a 150 nm wide slot, which determines the resonance frequency of the shared optical mode. To aid in the fabrication of the narrow slot separation, which is difficult to etch in the silicon nitride films used here, the test beam is connected on either end to narrow flexible tethers of length 5 μm and width 150 nm. These tethers (Fig. 2.9) are defined at a small angle ($\sim 5^\circ$) from the test beam, and after fabrication bend to a new static position closer to the waveguide nanobeam, thereby shrinking the slot separation (from 250 nm to 150 nm).

2.1.2 Structural Clamping Constraints

The silicon nitride material used for zipper resonators is deposited at high temperature in a

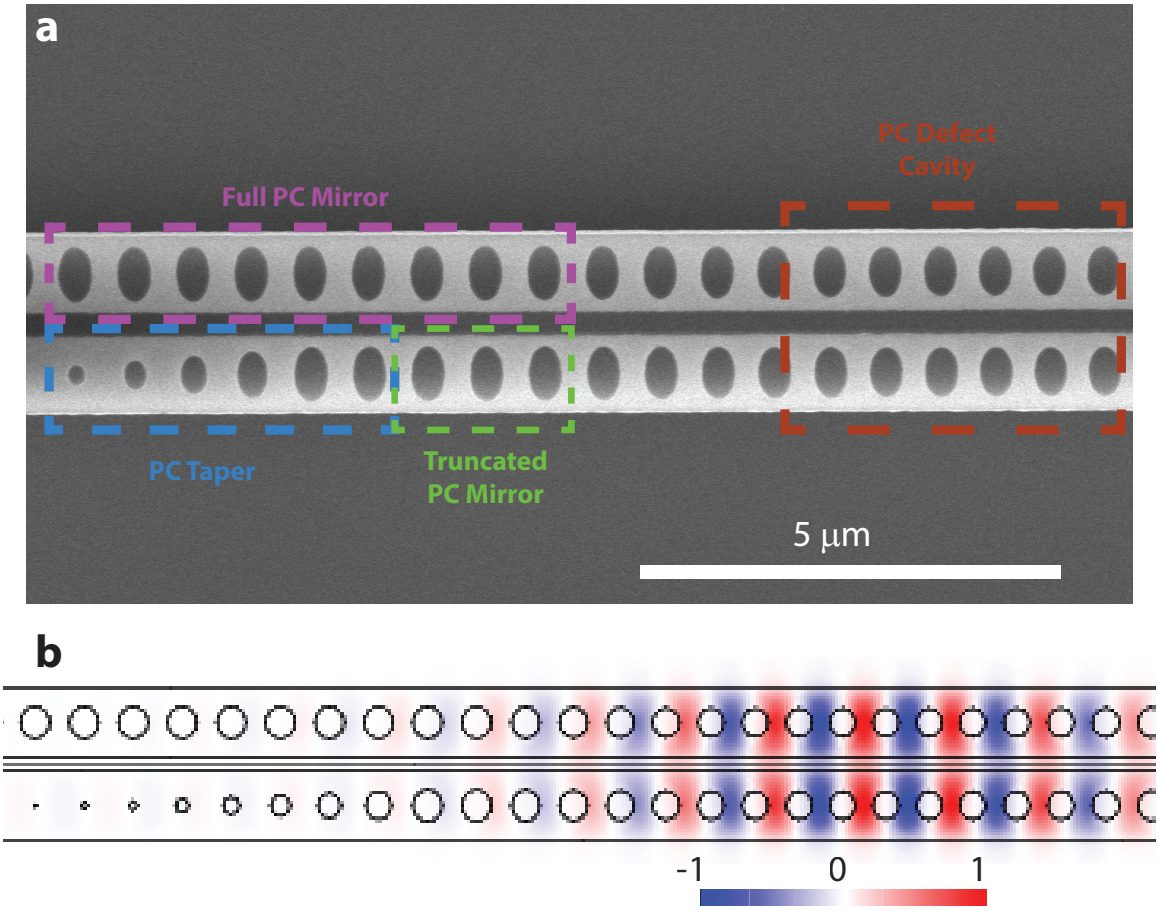

Figure 2.7: **Waveguide to Photonic Crystal Mirror Junction. a** SEM image of one half of the V-groove coupled zipper optomechanical resonator, with indications of relevant photonic crystal (PC) mirror and cavity sections. The bottom beam transitions to the waveguide taper mode converter to the left of the image. **b** FEM simulation of electric field in the y direction.

low-pressure chemical vapor deposition (LPCVD) process. As a result, at room temperature the silicon nitride film is tensile-stressed by the silicon substrate wafer. When the silicon substrate is removed from underneath the device layer, suspended features will strain towards clamping points. This material property, while useful for achieving excellent optical and mechanical quality in the optomechanical resonator, requires consideration in the structural design of the V-groove coupler.

Before suspension, the Si_3N_4 film normal stress is 800 MPa in magnitude. After suspension, however, particular device shapes and clamping arrangements can lead to significantly larger local stresses. For example, a large volume of suspended material will strain towards its clamping point, adding stress to any attached narrow sections. Stress of magnitude nearing the film tensile strength ($\sim$ 5 GPa) can cause breakages or low yield of device survival after fabrication. This is primarily a concern for the damping tether set, for which lengths of $< 10\,\mu$m typically break. A useful guideline

to designing structural supports is to avoid local stresses of greater than 1 GPa in simulation.

Either due to non-uniformity of the tensile stress in the z direction of the silicon nitride film or to the clamping asymmetry (film anchored to the silicon substrate below, but not above), the large membrane support plates bend out of the device layer plane after suspension. This bending (usually of order a few microns) can shift the z-position of the test beam by up to 200 nm (Fig. 2.8a), while only minimally bending the waveguide beam. The misalignment between the two beams causes both the optical quality factor and the optomechanical coupling of the resonator to be lowered significantly from their nominal simulation values. Adding a set of 6, 150 nm wide tethers connecting the membrane plate (on the side of the test beam) to the end of the V-groove (Fig. 2.9) pulls on the plate enough to compensate for the out-of-plane bending of the test beam, as shown in the edge-view SEM image of Fig. 2.8b.

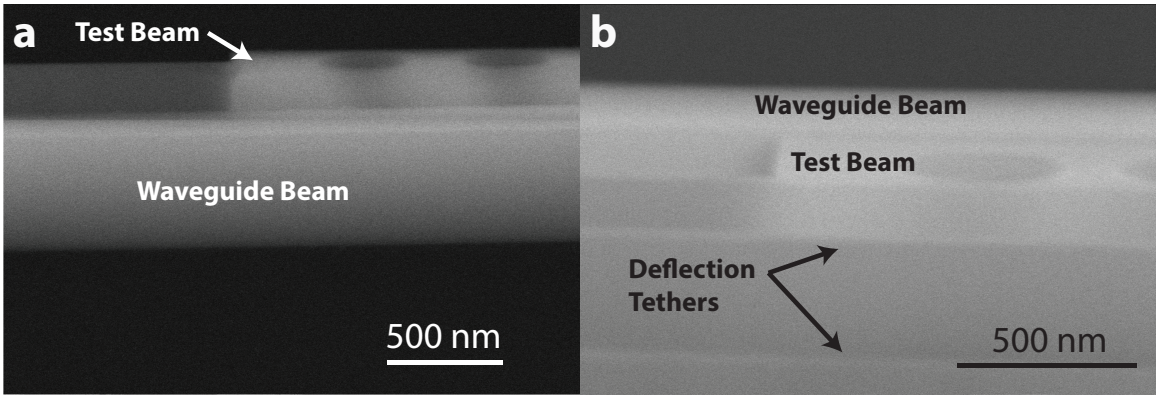

Figure 2.8: **Clamping Geometry. a** SEM image taken at an edge-view angle of a zipper device, without out-of-plane deflection tethers. The test beam in the background is seen to be flexed ~ 150 nm above the waveguide nanobeam in the foreground. **b** Edge-view SEM of a zipper device with 6, 150 nm wide deflection tethers. The test beam, this time imaged in the foreground, is observed to be level with the waveguide beam.

2.1.3 Process Steps

The major process steps in the fabrication of V-groove devices are shown in Fig. 2.10. Electron-beam lithography simultaneously defines the zipper resonator, tapered-waveguide mode-converter, and V-groove outline. This pattern is transferred from the electron-beam resist layer into the Si_3N_4 device layer using inductively-coupled plasma/reactive-ion etch (ICP-RIE). The devices are then suspended in a wet potassium hydroxide (KOH) base etch, which also etches the V-groove alignment feature. KOH etches (100) silicon crystal planes ~ 300 times faster than (111) planes, creating V-shaped or pyramidal features in the exposed areas of the silicon substrate. The sample is then cleaned using a sulfuric acid/hydrogen peroxide piranha etch, and dried using critical point drying. Table 2.1 and the following discussion provide the details of each fabrication step.

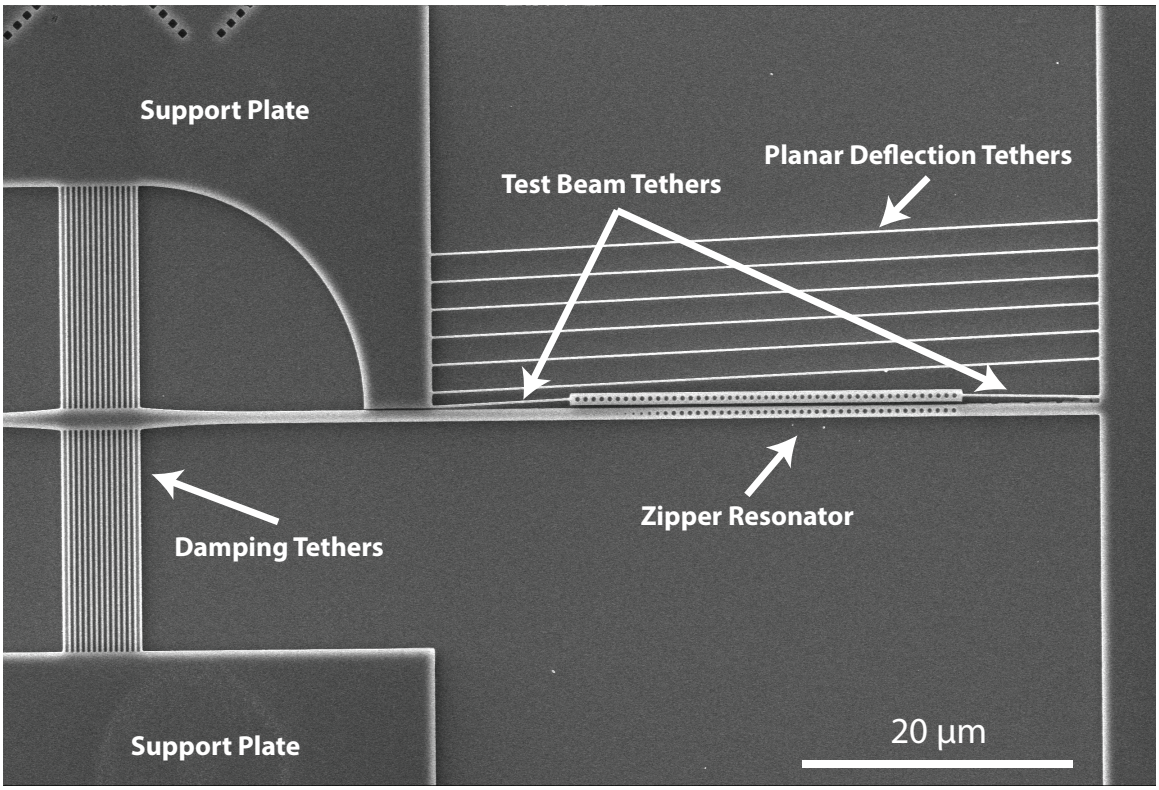

Figure 2.9: **Clamping Geometry.** SEM image of a device prior to suspension. In addition to the waveguide tip tether (not seen in this image), damping tether set, and test beam slot reduction tethers, a series 6 of tethers spanning the V-groove from a support plate to the groove end are used to prevent out-of-plane bending of the test beam.

The silicon nitride samples used in this work are purchased from Silicon Valley Microelectronics, which provides the wafer-scale LPCVD. A wafer is diced into 1 cm $\times$ 1 cm square chips by American Precision Dicing. Before beginning the fabrication process shown in Fig. 2.10, a chip is cleaned in acetone and isopropyl alcohol to produce a smooth sample surface. Electron-beam resist (Zeon Chemicals ZEP-520a) is then spin-applied to the chip at a rotational speed of 2000 rpm. The low spin speed results in a thick ($\sim$ 400 nm) resist layer, which is required for the Si_3N_4 plasma etch. Baking the sample at 180 °C completes the lithography preparation.

Electron-beam lithography is performed using a Vistec EBPG 5000+ system. When loading the sample onto a system cassette, the rotation of the sample with respect to the coordinate system of the EBPG must be minimized. This pre-alignment ensures that the electron-beam exposure defines V-groove shapes along crystal axes of the silicon substrate, and can be accomplished by rotating the sample such that a chip edge aligns to the crosshairs of the microscope alignment station.

Exposure of the device pattern utilizes the bulk-in-sleeve technique for generation large size-contrast features. Specifically, while the zipper resonator and waveguide taper portions of a device require high-resolution (2.5nm) exposure, the V-groove feature can be defined at low resolution. Due

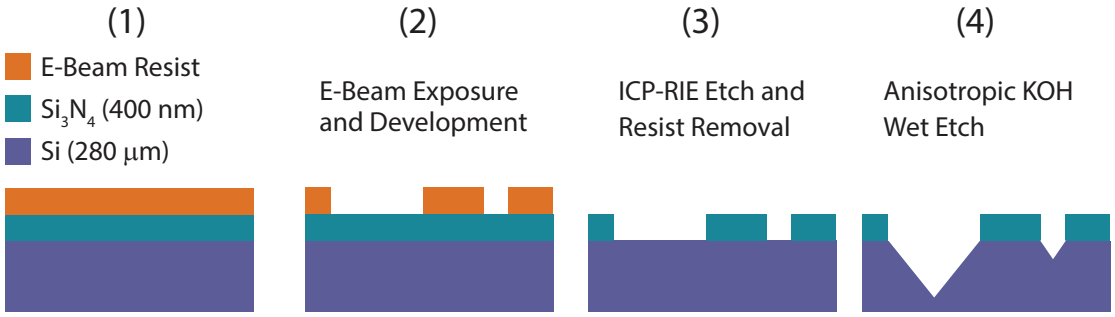

Figure 2.10: **V-Groove Fabrication Process.** Illustration (not to scale) of the significant fabrication steps for V-groove coupled devices.

Process Step	Sub-step	Parameter	Parameter Value	Duration
Clean Sample	Acetone Rinse	-	-	10 sec.
	IPA Rinse	-	-	10 sec.
	N_2 Nozzle Dry	-	-	10 sec.
Apply E-Beam Resist	Spin ZEP-520a	Spin Speed Spin Ramp	2000 rpm 1500 rpm/s	1 min.
	Hot Plate Bake	Temperature	180 °C	2 min.
E-Beam Lithography		Dose	170 μC/cm^2	-
E-Beam Development	ZED-N50	-	-	2 min. 30 sec.
	MIBK	-	-	30 sec.
	N_2 Nozzle Dry	-	-	10 sec.
ICP-RIE Nitride Etch		See Table 2.2		7 min. 10 sec.
Strip E-Beam Resist	ZDMAC	-	-	10 sec.
	Acetone Rinse	-	-	10 sec.
	IPA Rinse	-	-	10 sec.
	N_2 Nozzle Dry	-	-	10 sec.
Undercut	KOH	Concentration Temperature	30 % 72 °C	1 hour 40 min.
	H_2O $\times 2$	-		30 sec.
Piranha Clean	H_2SO_4:H_2O_2	Ratio Temperature	3:1 70 °C	10 min.
	H_2O $\times 2$	-	-	30 sec.
	Filtered IPA	-	-	-
Critical Point Dry		Bleed Time	10 min.	1 hour

Table 2.1: **V-Groove Process Parameters.** Listing of a chemical in a sub-step specifies submersion at room temperature of the sample in a beaker of the undiluted chemical, unless otherwise specified. Steps or sub-steps with a $\times N$ designation should be repeated for N iterations. IPA refers to Isopropyl Alcohol.

to the millimeter-scale size of the V-groove, the low-resolution coarse exposure saves significant tool time. The fine exposure (sleeve) defines a 4 μm outline of the photonic structure, while the coarse exposures (bulk) defines the remaining V-groove area. As these exposures occur at different times during the lithography process, an overlap in the patterns of > 1 μm ensures that tool positioning

Parameter	Parameter Value
RF Forward Power	23 W
ICP Forward Power	1000 W
DC Bias Voltage	78 V
C_4F_8 Flow Rate	22 sccm
SF_6 Flow Rate	12 sccm
Chamber Pressure	15 mTorr
Helium Backing Pressure	10 Torr
Helium Backing Flow Rate	5 sccm
Temperature	24 °C
Time Duration	7 min. 10 sec.

Table 2.2: **V-Groove ICP-RIE Etch Recipe.** Step parameters for the ICP-RIE silicon nitride etch in the Painter group Oxford Instruments Plasmalab 100 system.

errors do not produce exposure errors on the device.

After exposure, the sample is developed and loaded onto a carrier wafer for plasma etching. Silicon nitride can be etched using a silicon-type Bosch etch chemistry (C_4F_8/SF_6), albeit with only modest selectivity to ZEP-520a. A high-voltage-bias recipe was developed to etch sub-micron hole features of sufficient depth through the full Si_3N_4 thickness (Fig. 2.11a), the parameters of which are given in Table 2.2.

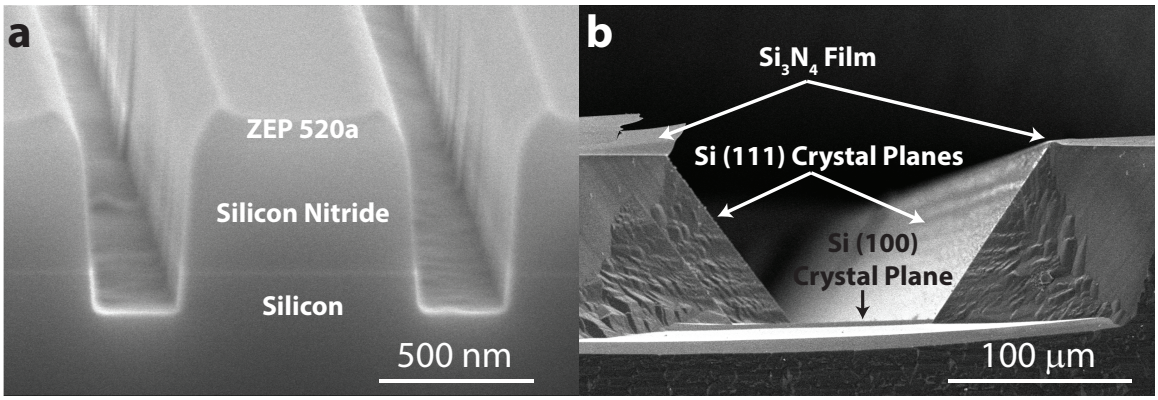

Figure 2.11: **V-Groove Geometry. a** SEM cross-section image of an etched hole pattern, prior to the removal of the ZEP-520a electron beam resist. **b** SEM edge image of a sample after the KOH liquid phase etch, defining a V-groove alignment feature along silicon (111) crystal planes.

The remainder of the fabrication process is comprised of liquid-phase etches. After suspension of zipper resonator devices, direct sample drying using nitrogen nozzle blowers will cause device collapse due to strong liquid surface tension forces on the microscale structures. To mantain an air gap between the zipper nanobeams, samples must not be allowed to dry during the following wet etch steps.

Silicon crystal (111) planes are oriented at a 54.7° angle from the (100) planes parallel to the sample surface. Determining the height at which a fiber will rest in an etched V-groove (Fig. 2.11b)

is then simply a geometric relation to the width of the exposed groove feature, as shown in Fig. 2.12. The etch rate of silicon in KOH heated to 74 °C is 0.5 μm/minute, so the etch duration must be greater than ~ 1.5 hours in order to define a deep enough groove such that the fiber rests on (111) planes rather than the bottom (100) plane. During this time, (111) planes etch back from the mask edge by 2 ± 0.3 μm, which is enough such that the extra width of groove must be accounted for in pattern generation. With careful attention to the KOH etch temperature and concentration, the $\pm$300 nm error in (111) etch length ensures that fiber misalignment in coupling produces less than 1 dB of loss due to mode mismatch.

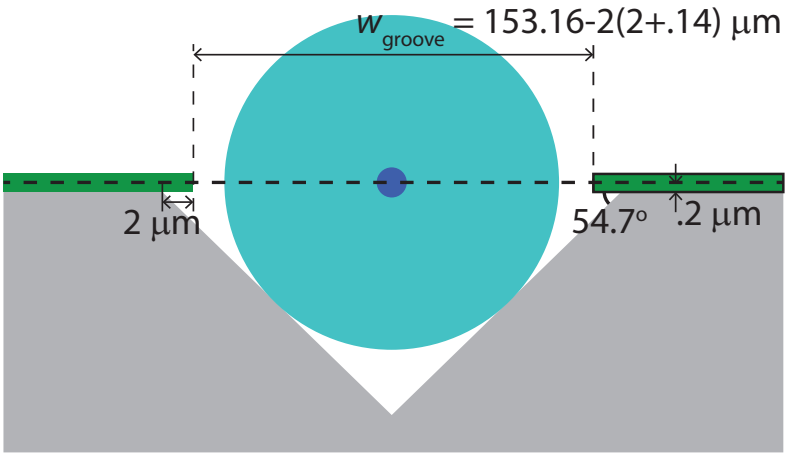

Figure 2.12: **V-Groove Geometry.** Illustration (not to scale) of the (111) crystal planes and the relevant V-groove sizing for optimal fiber alignment. The optimal width of the lithographically defined groove feature is $w = 148.88$ μm for the specific device parameters: 128 μm diameter fiber, 400 nm thick device layer, and 2 μm (111) plane etch distance.

After the KOH etch the sample is rinsed twice in water, then transferred to a piranha cleaning solution. The sample is then water-rinsed again, placed in filtered isopropyl alcohol, and loaded into a critical point drying tool. A critical point dryer pressurizes and heats the isoproyl alcohol in a trajectory that transitions from liquid to gas phase, but avoids crossing a phase boundary by passing the carbon dioxide critical point. This drying method avoids destructive surface tension effects on the sample, and is necessary for zipper resonators or other flexible slotted-type cavities. This step completes the fabrication process, and the sample is ready for fiber coupling.

2.1.4 Fiber-Coupling Procedure

A dedicated station was constructed for the fiber-coupling of V-groove devices (Fig 2.13). The sample is fixed to a chip holder with ultraviolet(UV)-curing epoxy (Dymax series OP-4-20632). The chip holder is also clamped in place to prevent jostling and misalignment during coupling. An SMF-28e optical fiber section is stripped of its polymer coating, cleaved, and placed in a fiber clamp mounted

to a 5-axis translation and rotation manual stage (Newport 561D-XYZ-LH and 561-TILT-LH). The length of coating-stripped fiber must be larger than the length of the V-groove between the edge of the chip and the silicon nitride waveguide tip, otherwise the fiber cannot be aligned for optimal efficiency.

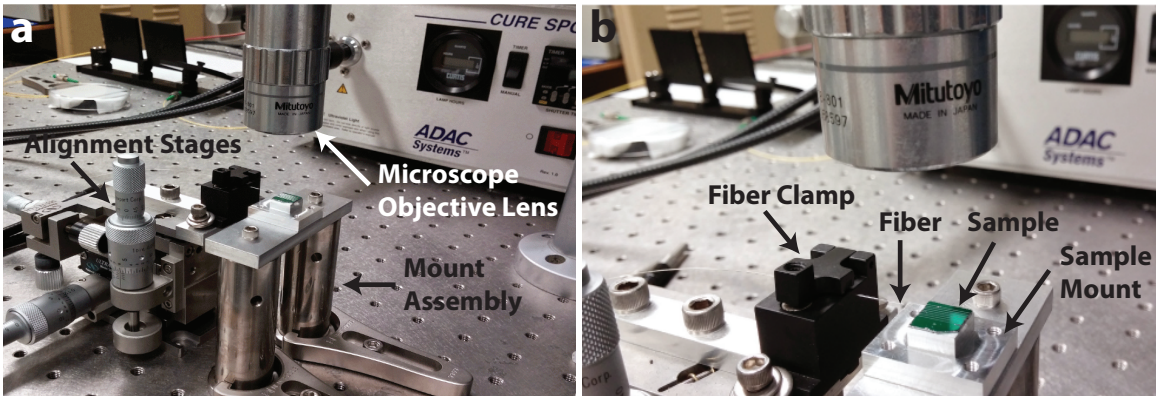

Figure 2.13: **V-Groove Fiber-Coupling Station.** Photographs of the V-groove coupling station, showing the 5-axis fiber positioning stages, mounted sample, and microscope orientation.

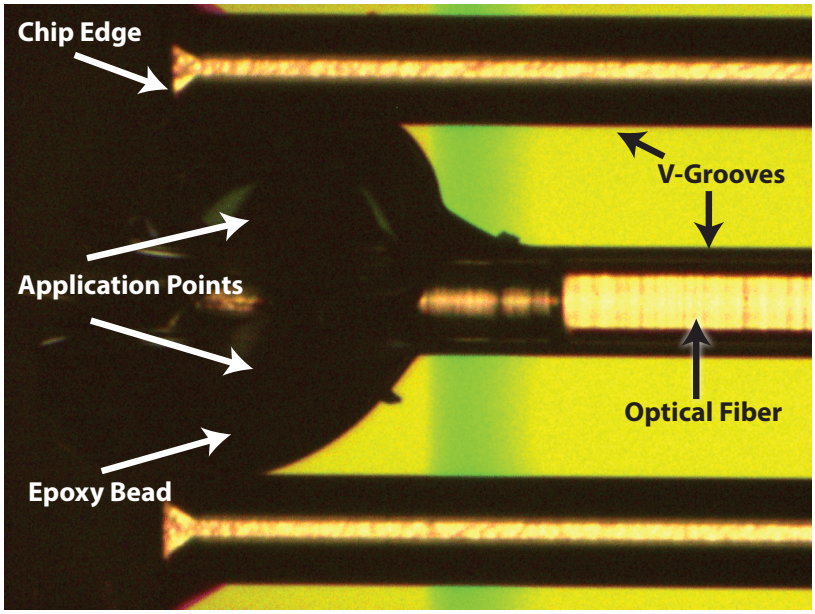

Figure 2.14: **Epoxied Fiber.** Microscope image in the coupling station, with V-groove, optical fiber alignment, and epoxy bead application points indicated.

2.1.5 Coupling Results

The rotation of the fiber in the x-y plane is first adjusted to match the V-groove orientation through the microscope imaging system. Then the fiber is tilted at a slight angle with respect to the sample surface, such that the cleaved tip is the closest part of the fiber to the sample in z. This ensures that the fiber tip comes to rest on the side-walls at the optimal height when lowered into the V-groove. The angle between chip and fiber should not exceed more than a few degrees however, since a large angle will complicate the epoxy step to follow.

After the angular alignment, the fiber can be lowered into the V-groove. The contact of the fiber with the V-groove walls will be apparent in the microscope image, as the pattern of light reflected from the bottom of the groove will stop changing as the fiber is lowered. For this purpose it is useful, although not essential, to leave a bottom flat section of the groove during fabrication, such that the "V" shape is not fully defined. Once the fiber has made contact, the tip should be moved forward in x towards the silicon nitride waveguide tip. FEM simulations show that separations between fiber and waveguide of $< 10\ \mu$m will produce high-efficiency coupling.

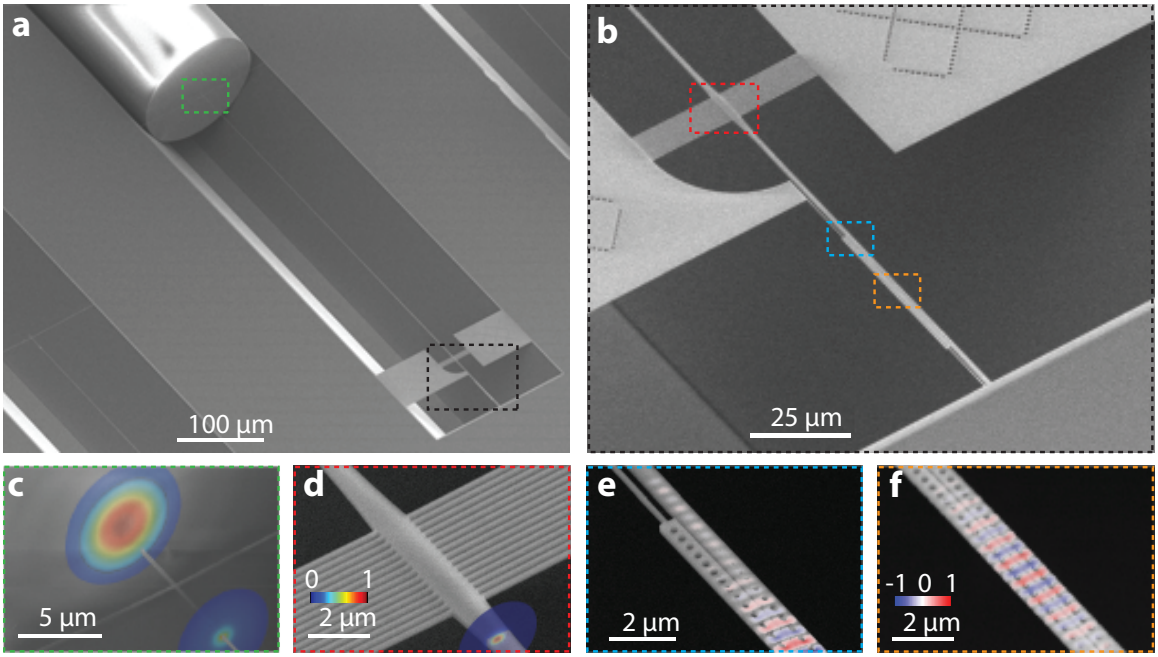

Figure 2.15: **Fiber-Coupled Device.** SEM images of the full fiber-coupled device (**a**) and zoomed insets of optical conversion junctions (**b-f**). Normalized FEM simulations of optical power are overlayed onto the fiber facet and silicon nitride waveguide at the fiber-to-waveguide junction (**c**), and the widened waveguide at the structural support tether section (**d**). **e** and **f** show overlays of FEM-simulated E_y at the photonic crystal input mirror and center of the zipper cavity, respectively.

Once the fiber is in position, it can be glued into place using fast-curing UV epoxy. A small amount of epoxy, daubed onto the end of a section of extra optical fiber, is appropriate for securely

fixing the fiber without causing extra epoxy to flow across sensitive areas of the sample. The epoxy is gently applied to the sample by hand on the edge of the V-groove. Placing the epoxy directly on the fiber can cause jostling and misalignment. Within $\sim$ 10 seconds of application the epoxy will flow down the groove, and should be cured with the UV lamp before it reaches the device. 10 seconds of curing time is sufficient to fully cure the epoxy. At this point the fiber will be rigidly mounted, and can be unclamped from the positioning stages. The epoxy joint can withstand light pulling of the fiber, although a secondary epoxy joint can be used to further secure the fiber to the sample mount.

A fully fabricated and fiber-coupled device is shown in the series of SEM images in Fig. 2.15. The other end of the optical fiber is spliced to a fiber optical circulator in a characterization test setup (Fig. 2.16). Scanning the wavelength of the external-cavity diode laser and measuring the reflected power from a device on a photodiode produces the reflection spectrum given in Fig. 2.17a. While the set of 3 sharp dips correspond to fundamental and second-order optical cavity modes of the zipper resonator [37], the broadband fringe pattern is a product of the fiber coupler. The pattern can be understood by recognizing that off-resonance from cavity modes, the zipper resonator functions as a high-reflectivity mirror. Cleaved optical fibers also reflect light with a small reflectivity $R \approx 3.5\,\%$. These two reflection source then create a weak Fabry-Perot-like optical cavity along the waveguide taper.

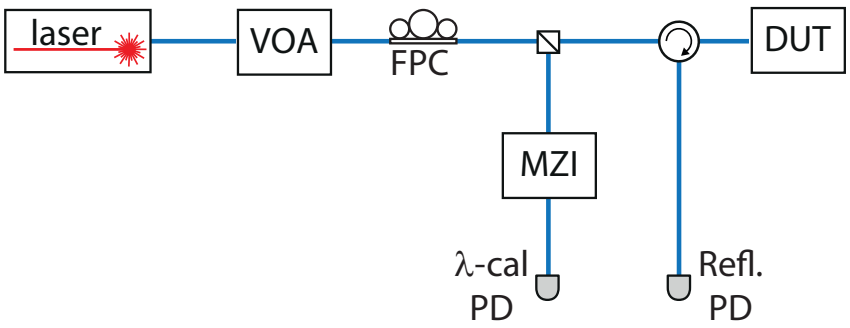

Figure 2.16: **Optical Characterization Apparatus.** The reflection spectroscopy setup uses a Variable Optical Attenuator (VOA) to control the laser power coupled to a device under test (DUT). A fiber polarization controller (FPC) matches the probe laser polarization to that of the device. An optical cirulator routes the device reflection to a photodetector (PD). A separate optical path of the setup sends the signal through a fiber Mach-Zehnder Interferometer (MZI), which produces an interference pattern for relative wavelength calibration.

While the fringe visibility could be diminished by using anti-reflection coated fiber facets, in initial characterization the fringe pattern in the reflection spectrum provides a convenient calibration of

the efficiency η_{cpl} of the fiber coupler. Fitting the visibility

$$V = \frac{\eta_{\mathrm{cpl}}(1-R)}{\sqrt{R}(1-\eta_{\mathrm{cpl}}^2)} \tag{2.3}$$

produces the efficiency as a function of wavelength in Fig. 2.17b, which is seen to lie only $\sim 10\,\%$ below the optimal simulation efficiency, with $\eta_{\mathrm{cpl}} = 74.6\,\%$ at the wavelength $\lambda = 1538\,\mathrm{nm}$ of the zipper mode of interest.

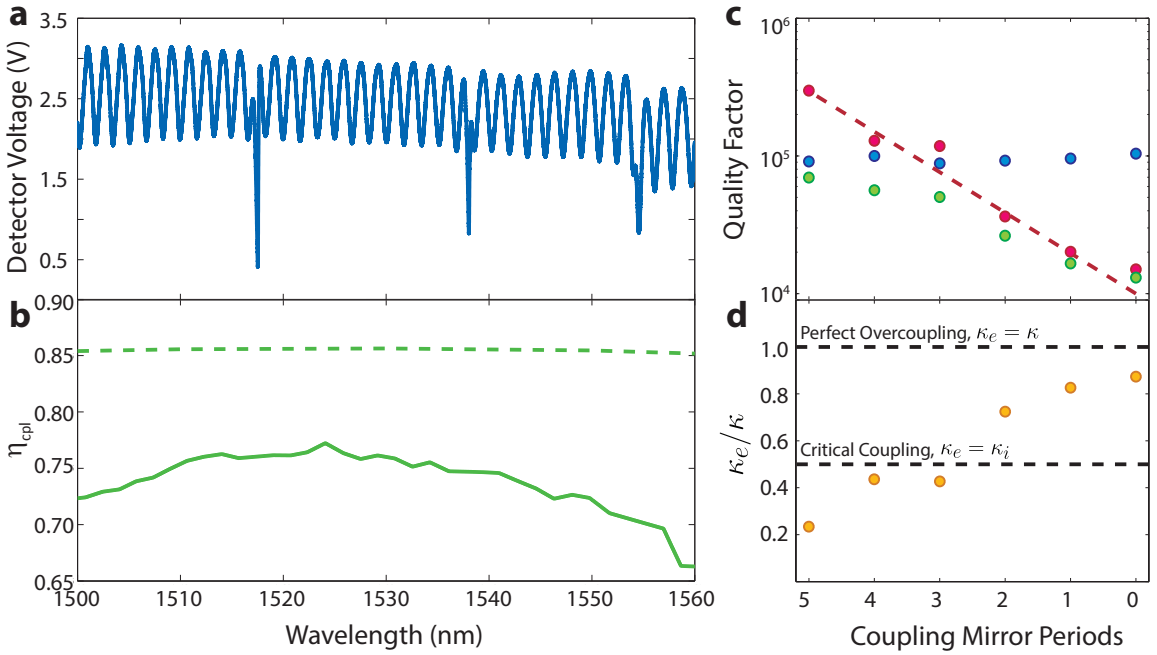

Figure 2.17: **V-Groove Optical characterization.** **a** Wideband reflection spectrum from a fiber-coupled device, showing sharp zipper resonance dips at fundamental and second-order mode wavelengths, as well as fringe patterns from the weak cavity between the photonic crystal and fiber facet. **b** The solid line shows η_{cpl} extracted from fitting the reflection plotted in **a**, while the dashed line shows the optimal simulation efficiency. **c** Intrinsic (blue), extrinsic (red), and total (green) optical quality factor as a function of the number of photonic crystal holes in the input coupling mirror. **d** Coupling depth $\kappa_{\mathrm{e}}/\kappa$ as a function of hole number, with undercoupling and overcoupling regions bounded by the dashed lines at the critical coupling and perfect overcoupling levels.

The coupling depth to the zipper cavity mode is determined by fitting the narrow-band wavelength dependence of the optically reflected intensity. While the bare Lorentzian lineshape of the zipper modes sometimes interferes with the broadband fringe pattern to create Fano lineshapes, accounting for these effects with a coupled-cavity model allows us to extract κ_{e} and κ_{i}. This analysis is performed for a series of devices, in which the number of coupler mirror-hole periods is varied (Fig. 2.17c,d). While the intrinsic quality factor Q_i is seen to remain constant along the mirror variation, the extrinsic quality factor Q_e decreases by more than an order of magnitude between 5 and 0 mirror holes, in good agreement with simulation. The total quality factor Q also transitions

from being limited by intrinsic loss to being limited by Q_e.

For the purposes of detection efficiency in an optomechanics experiment, the relevant measure of coupling depth is the ratio of extrinsic coupling rate to the total loss rate of the resonator, or κ_e/κ. The mirror variation tunes this ratio from the strongly undercoupled regime, where resonator loss of light is limited by parasitic scattering, to the strongly overcoupled regime, where the detection channel is the dominant cause of cavity radiation.

2.1.6 Low-Temperature Performance

A simple estimate of the expected thermal contraction of both the silicon substrate and the glass optical fiber shows that a device which is fiber-coupled at room temperature should remain aligned to within 50 nm when cooled to sub-Kelvin temperatures. The difference in linear expansion between the silicon wafer substrate and silicon dioxide optical fiber over the $L = 62.5$ μm fiber radius, and for a room temperature to milliKelvin temperature difference of $\Delta T = 293$ K, is $\Delta L = L\Delta T(\alpha_{\mathrm{TE,\,Si}} - \alpha_{\mathrm{TE,\,SiO_2}}) = 62.5$ μm$\times 293$ K$\times(2.6 \times 10^{-6}$ K$^{-1} - 5.6 \times 10^{-7}$ K$^{-1}) = 37$ nm. Although this crude approximation neglects the temperature dependence of the thermal expansion coefficient α_{TE}, the difference in thermal expansion between silicon and silicon dioxide glass has been seen to decrease with temperature [91], and the calculated 37 nm misalignment is likely an overestimate at cryogenic temperatures. This is tested with the sample previously measured at room temperature in Fig. 2.17a,b, mounted to the mixing chamber plate of a dilution refrigerator and cooled to sub-Kelvin temperatures. The optical spectrum at 10 mK (Fig. 2.18) shows a decrease in reflection, with $\eta_{\mathrm{cpl}} = 39\,\%$ in comparison to the room temperature efficiency of $\eta_{\mathrm{cpl}} = 74.6\,\%$. This $\sim 50\,\%$ decrease in efficiency has also been observed in certain arrangements of optical fiber within the dilution refrigerator, and is believed to stem from temperature dependent bending loss [92] of optical fiber spooled under tension. Further optimization of the cryogenic optical fiber paths (e.g., securing looped fiber sections with copper tape rather than tensioned spools) produced increased transmission efficiencies from $\sim 50\,\%$ to $\sim 95\,\%$, and thus the reflection loss observed in Fig. 2.18 would likely be mitigated in future testing.

2.1.7 Drawbacks

While the V-groove coupler is efficient and robust for cryogenic operation, a few drawbacks make it non-ideal for certain optomechanics experiments. Although the fabrication process is simple for silicon nitride devices such as zipper resonators, silicon nanobeams would require more advanced masking techniques to protect the device layer during V-groove etches. Since many of the goals of operating an optomechanical resonator at low temperature are to cool the mechanics to their quantum ground state, a high-mechanical-frequency structure such as the silicon nanobeam optomechanical

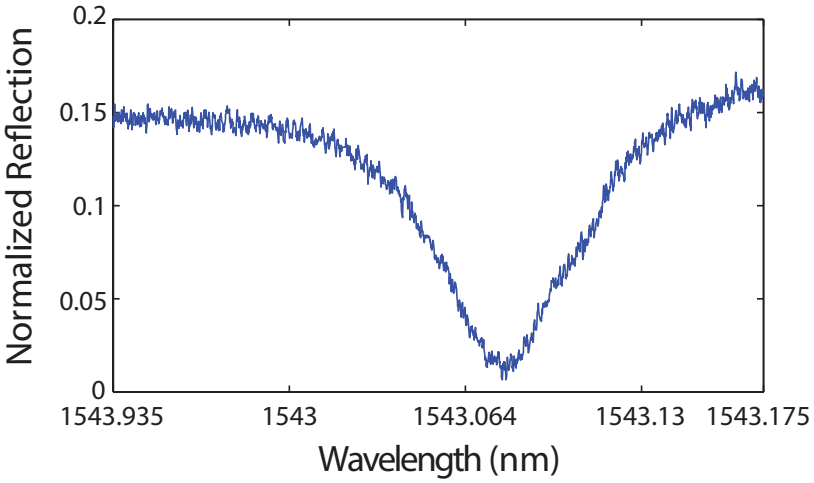

Figure 2.18: **V-Groove Cryogenic Reflection.** Narrow-band optical reflection spectrum centered about the fundamental optical mode of a V-groove coupled device at 10 mK. The decreased reflection from room temperature represents an approximatly 50 % reduction in η_{cpl}. In this case the reflection loss is found to arise from inefficiencies of the optical fiber paths within the dilution refrigerator prior to coupling to the sample.

crystal is desirable. Another drawback to V-groove couplers is the large sample-surface footprint required for fiber placement. This use of sample area limits the number of devices to $\sim$ 50 for a millimeter- to centimeter-scale chip, and decreases the probability of fabricating a high-quality resonator.

2.2 Silicon End-Fire

Similarly to the V-groove coupler, the end-fire method couples an optical fiber tip to a mode-conversion waveguide, which in turn couples to the optomechanical resonator. This coupling scheme is optimized for silicon-based devices. To increase the number of devices on a sample to which a fiber can couple, the fiber is not placed in a V-groove feature, but rather is dynamically positioned to particular devices with motorized translation stages.

2.2.1 Device Design

The following sub-sections describe the significant coupling junctions of end-fire coupled devices. Unlike the V-groove couplers described previously, the end-fire coupler design is constrained by certain optical and mechanical properties of silicon, the impact of which will be explained for each junction. The focus of this design section will therefore be less on the optimization of each feature (as was done for the V-groove coupler), and more on the parameter considerations that efficiently meet the dimensional constraints. The coupling performance obtained with a full optical simulation

of the structure will then be discussed and compared to realized devices in Sec. 2.2.4.

2.2.1.1 Waveguide Tip

Since the refractive index of silicon ($N = 3.48$) is significantly larger than that of silicon nitride ($N = 2$), the optical mode profiles supported by index waveguides are more confined and smaller in extent. While a 230 nm×400 nm Si_3N_4 waveguide cross section guides a mode with diameter of 10 μm, a Si waveguide with dimensions 230 nm×220 nm confines $\lambda = 1550$ nm light to a 2.5 μm mode profile. Rather than attempt to scale the waveguide width of a silicon taper tip to mode-match to an SMF-28 optical fiber mode (and thereby having larger sensitivity to dimensional error in fabrication), we chose to focus the launched fiber mode before coupling into the device. This is achieved using a lensed optical fiber tip purchased from OZ Optics Ltd. (part number TSMJ-X-1550-9/125-0.25-7-2.5-14-2), in which a spherical lens is laser carved into an SMF-28 fiber. The lens focuses light to a 2.5 μm spot size at a working distance of 14 μm. The focused laser spot is then coupled into the 230 μm ×220 μm cross-section silicon waveguide tip, as illustrated in Fig. 2.19a. This design consideration also plays into the following waveguide taper design.

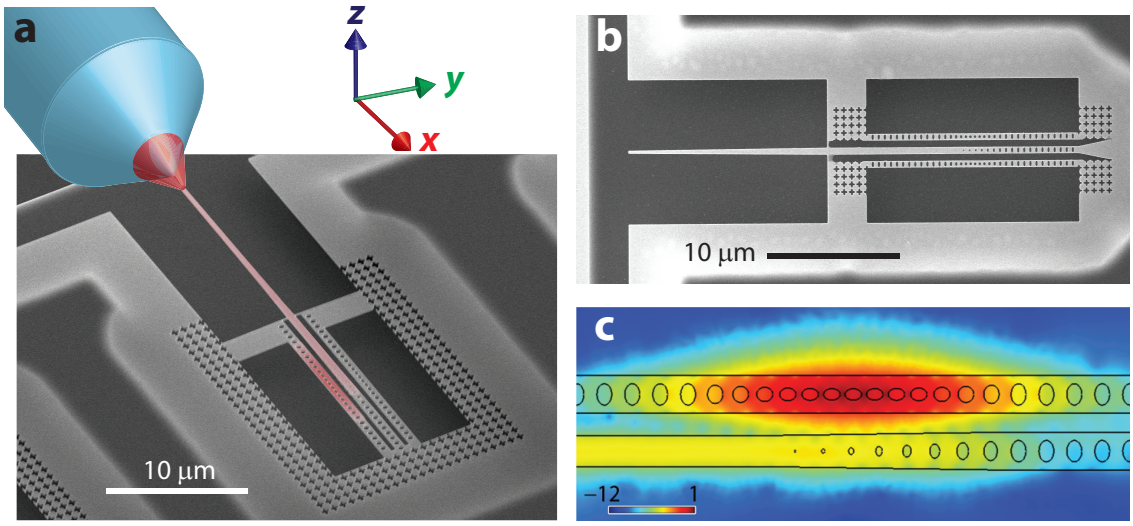

Figure 2.19: **End-Fire Coupler. a** Illustration (not to scale) of the lensed fiber end-fire coupled to a silicon nanobeam through a side coupled waveguide taper. **b** Top-view SEM image of the device, showing two nanobeam resonators coupled to a common coupler waveguide. **c** FEM simulation of optical power for a side-coupled nanobeam resonator, illustrating how light evanescently couples out of the cavity and into the waveguide for fiber collection and detection.

2.2.1.2 Waveguide Taper

After coupling into the silicon waveguide, the mode is then further confined by expanding the waveguide width in a similar fashion to the V-groove mode converter. Unlike the tensile-stressed silicon

nitride used for V-groove coupling however, the silicon film utilized here features small amounts of compressive stress. The structural tether supports in the silicon nitride device rely upon tensile stress to suspend high-aspect-ratio in the plane of the device layer. In silicon, these tethers would themselves bend under gravity, and cannot be used to support a long waveguide taper. For this reason the silicon waveguide taper is restricted to a length of 14 μm. Suspended features of larger extent result in bending to such a degree that the waveguide tip makes contact with the substrate wafer after fabrication, preventing efficient optical coupling. Although the waveguide taper is over an order of magnitude shorter than that of the V-groove device, the choice of focusing the launched fiber mode to a 2.5 μm laser spot (as discussed in the previous sub-section) assists in achieving a high-efficiency waveguide taper. Since the optical mode is already partially confined in the silicon at the waveguide tip, the waveguide can linearly expand from $w = 230$ nm to $w = 600$ nm over a 14 μm transition length, and yet only incur 1 dB of optical loss.

2.2.1.3 Support Tether

After expanding to a width of $w = 600$ nm, the central waveguide is supported by a tether of width 70 nm and length 350 nm. The tether itself is connected to suspended silicon membrane plates of area 4.3 μm $\times$ 2.7 μm. These membrane plates also support phononic crystal radiation shields and the side-coupled nanobeam resonators described in the following sub-sections.

2.2.1.4 Nanobeam Resonator

Unlike the V-groove coupler, the end-fire coupler uses evanescent coupling between the central waveguide and the nanobeam resonator [93], as shown in the simulation of Fig. 2.19. The 600 nm wide central waveguide supports a propagating mode that is slightly evanescent, and couples to a near-field nanobeam cavity analogously to tapered fiber coupling. This side coupling has the benefit over end-coupling (as used for the V-groove devices) in that κ_e is continuously tunable by the slot separation between the waveguide and nanobeam, rather than discretely tunable by mirror-period number. The side-coupling also enables two resonators to be coupled to a common waveguide, effectively doubling the number of devices on a sample accessible to the fiber and increasing the probability of attaining a high-quality resonator.

2.2.1.5 Photonic Crystal Mirror

Following the side-coupling region, the central waveguide transitions to a photonic crystal mirror through a series of seven holes, linearly increasing in dimension from 50 nm diameter to the nanobeam mirror hole height of 320 nm and width 279 nm. Twelve subsequent mirror holes then produce a near-unity-reflectivity photonic crystal mirror. In the analogy with fiber taper coupling, the photonic crystal mirror preserves the single-sided coupling scheme by preventing light that couples out of the

cavity resonance from propagating into another direction channel, and directing the signal back through the waveguide taper for collection by the optical fiber. Laser probe light far from a cavity resonance does not couple into either side-coupled device, and merely reflects from the mirror.

2.2.1.6 Acoustic Radiation Shield

At the ends of the nanobeam resonators, where they clamp on one device end to the silicon substrate and the other end to the membrane support plate, a 2-dimensional phononic crystal radiation shield is etched to provide high mechanical quality factor of the acoustic mode at low temperature. Coupling of the mechanical mode to the bulk silicon substrate is impeded by four such shield holes at each end of the resonator.

2.2.2 Process Steps

The fabrication process (Fig. 2.20 and Table 2.3) begins with electron-beam exposure of a 1-dimensional array of devices oriented on the edge of a rectangular exposed region between the waveguide tips and the edge of the chip. The rectangular exposed area defines a trench on the edge of the sample, allowing access to the optical fiber.

After transferring the device pattern into the silicon device layer using the etch parameters detailed in Table 2.4 and removal of the ZEP-520a resist layer, photoresist is applied to the sample surface for a second lithography step. The photoresist (Protek PSB sold by Brewer Science) is specifically resistant to KOH and tetramethylammonium hydroxide (TMAH), which are common silicon etchants. Masking the silicon devices in a protective layer of PSB (Fig. 2.22) allows use of KOH or TMAH for etching of the fiber-access trench without damaging the devices. The PSB is exposed in a Karl Suss MA-6 Mask Aligner tool in a rectangular pattern covering the silicon devices, with the edge extending less than 5 μm past the waveguide tips. Note that PSB is a negative tone photoresist, so the exposed area becomes the etch mask upon development. Maintaining the edge separation of < 5 μm is important for keeping the silicon substrate from encountering the optical mode launched from the lensed fiber, which causes optical loss in absorption and reduction of η_{cpl}.

The buried SiO_2 layer in the trench, exposed by the PSB, is etched using a C_4F_8 plasma in an RIE etch (Table 2.5). The sample is then submerged in 5 % concentration TMAH at 72 °C. At this temperature and concentration, TMAH etches silicon with high selectivity to both SiO_2 and PSB. After ~ 2 hours of etch time a trench of depth ~ 100 μm will be defined. The PSB is then stripped from the sample using a piranha etch, and the devices are undercut with a hydroflouric acid (HF) etch (Fig. 2.24). Two additional cycles of piranha and diluted HF etches are optional cleaning and silicon surface preparation steps for high quality resonators.

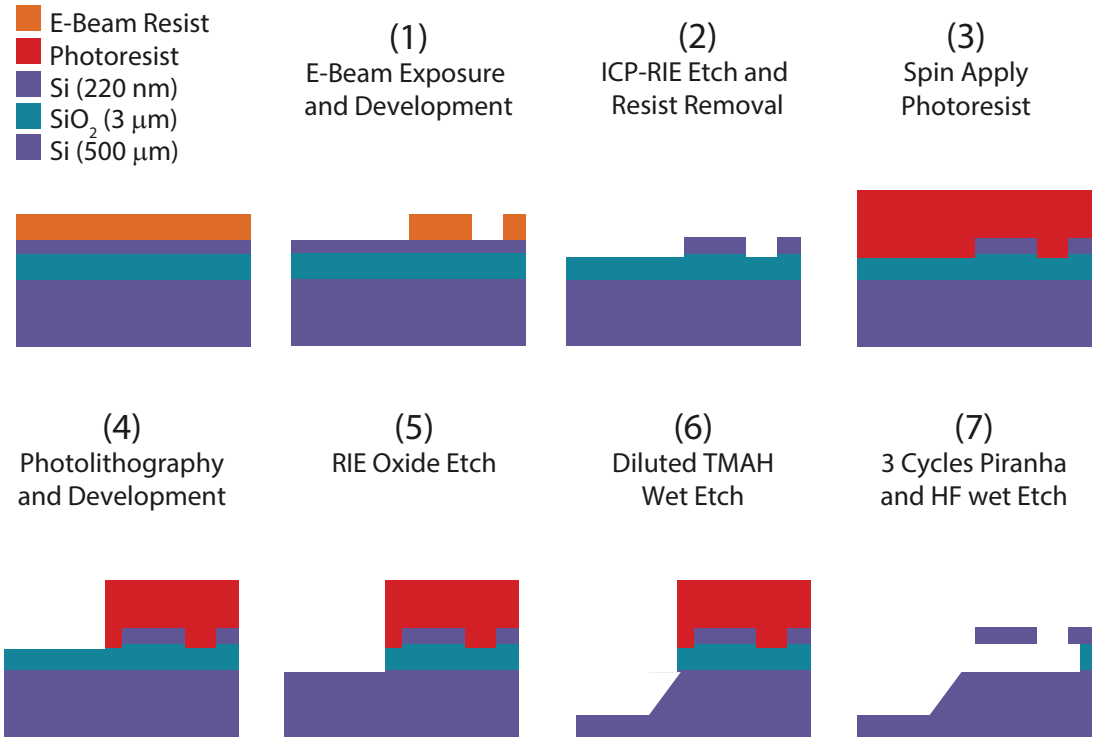

Figure 2.20: **End-Fire Fabrication Process.** Illustration (not to scale) of the significant fabrication steps for end-fire coupled devices.

2.2.3 Fiber-Coupling

In ambient room conditions an end-fire sample can be fiber coupled using motorized positioning stages. The coupling efficiency is robust to angular misalignment of tip/tilt and rotation to within 5°, enabling the use of manual goniometer and rotation stages. With a microscope imaging system, the lensed fiber is lowered to the approximate height of the device layer until a small optical reflection appears. Using the reflection signal as feedback, the fiber position is further adjusted in x, y, and z until the reflection is maximized.

2.2.4 Coupling Results

Coupling efficiency for end-fire devices ranges from $50 - 70\,\%$, occasionally reaching the optimal simulation $\eta_{\mathrm{cpl}} = 75\,\%$. A typical narrowband device reflection is shown in Fig. 2.26a, showing both high $\eta_{\mathrm{cpl}} = 63\,\%$ and high quality factor $Q_{\mathrm{i}} = 5 \times 10^5$. Variation across a set of devices of the gap width between the nanobeam resonator and the central coupling waveguide tunes the coupling depth $\kappa_{\mathrm{e}}/\kappa$ from strongly overcoupled to strongly undercoupled, as shown in Fig. 2.26b.

Process Step	Sub-step	Parameter	Parameter Value	Duration
Clean Sample		See Table 2.1		
Apply E-Beam Resist	Spin ZEP-520a	Spin Speed Spin Ramp	7000 rpm 2500 rpm/s	1 min.
	Hot Plate Bake	Temperature	180 °C	2 min.
E-Beam Lithography		Dose	230 μC/cm^2	-
E-Beam Development		See Table 2.1		
ICP-RIE Silicon Etch		See Table 2.4		7 min. 25 sec.
Strip E-Beam Resist		See Table 2.1		
Surface Preparation	NH_4OH:H_2O_2:H_2O	Ratio	1:1:40	3 min.
	N_2 Nozzle Dry	-	-	10 sec.
Apply Photoresist	Spin PSB Primer	Spin Speed Spin Ramp	2000 rpm 500 rpm/s	1 min.
	Hot Plate Bake	Temperature	110 °C	1 min.
	Hot Plate Bake	Temperature	220 °C	5 min.
	Spin PSB	Spin Speed Spin Ramp	2000 rpm 500 rpm/s	1 min. -
	Hot Plate Bake	Temperature	110 °C	2 min.
Photolithography	Soft Contact	Wavelength	365 nm	30 sec.
Post-Exposure	Hot Plate Bake	Temperature	110 °C	2 min.
Develop Photoresist (×6, or as needed)	Ethyl-Lactate	-	-	10 sec.
	N_2 Nozzle Dry	-	-	10 sec.
Post-Development	Hot Plate Bake	Temperature	200 °C	3 min.
ICP-RIE Oxide Etch		See Table 2.5		12 min.
Trench Etch	TMAH	Concentration Temperature	5 % 72 °C	2 hours
	H_2O ×2	-		30 sec.
Strip Photoresist	H_2SO_4:H_2O_2	Ratio Temperature	3:1 70 °C	10 min.
	H_2O ×2	-	-	30 sec.
Undercut	HF	-	-	2 min.
	H_2O ×2	-	-	30 sec.
Surface Termination (×2)	H_2SO_4:H_2O_2	Ratio Temperature	3:1 70 °C	10 min.
	H_2O ×2	-	-	30 sec.
	HF:H_2O	Ratio	1:10	2 min.
	H_2O ×2	-	-	30 sec.
	N_2 Nozzle Dry	-	-	10 sec.

Table 2.3: **End-Fire Process Parameters.** Listing of a chemical in a sub-step specifies submersion at room temperature of the sample in a beaker of the undiluted chemical, unless otherwise specified. Steps or sub-steps with a $\times N$ designation should be repeated for N iterations. IPA refers to Isoproply Alcohol.

2.2.5 Cryogenic Coupling Procedure

The end-fire coupling technique makes use of a few key design aspects to enable fiber coupling in cryogenic conditions. A particularly useful aspect of the sample arising from fabrication is the angle

Parameter	Parameter Value
RF Forward Power	16 W
ICP Forward Power	600 W
DC Bias Voltage	57 V
C_4F_8 Flow Rate	41 sccm
SF_6 Flow Rate	10 sccm
Chamber Pressure	15 mTorr
Helium Backing Pressure	10 Torr
Helium Backing Flow Rate	5 sccm
Temperature	20 °C
Time Duration	7 min. 25 sec.

Table 2.4: **End-Fire Silicon Plasma Etch Recipe.** Step parameters for the ICP-RIE silicon etch in the Painter group Oxford Instruments Plasmalab 100 system.

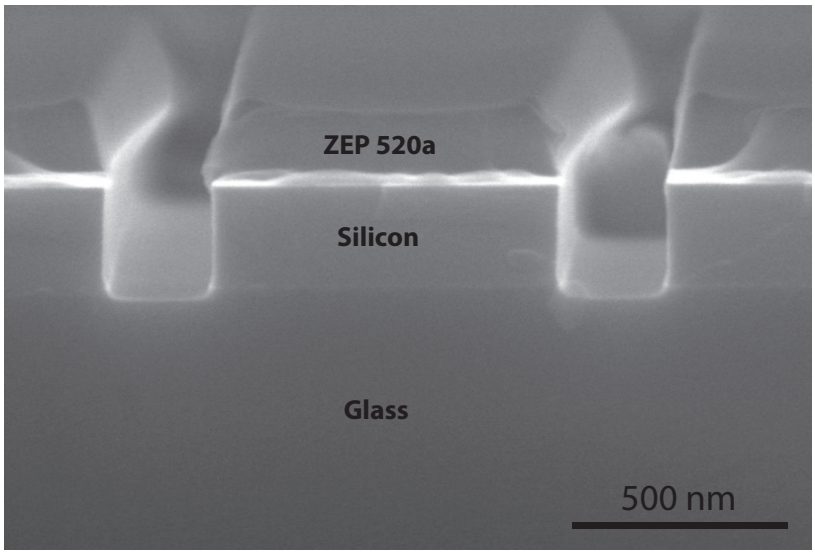

Figure 2.21: **ICP-RIE Etch.** SEM cross-section image of a plasma etched hole pattern, prior to the removal of the ZEP-520a electron beam resist.

Parameter	Parameter Value
RF Forward Power	150 W
ICP Forward Power	2200 W
DC Bias Voltage	155 V
C_4F_8 Flow Rate	70 sccm
O_2 Flow Rate	5 sccm
Chamber Pressure	8 mTorr
Helium Backing Pressure	5 Torr
Helium Backing Flow Rate	5 sccm
Temperature	15 °C
Time Duration	12 min.

Table 2.5: **End-Fire Oxide Plasma Etch Recipe.** Step parameters for the ICP-RIE silicon dioxide etch in the Kavli Nanoscience Institute Oxford Instruments ICP 380 system.

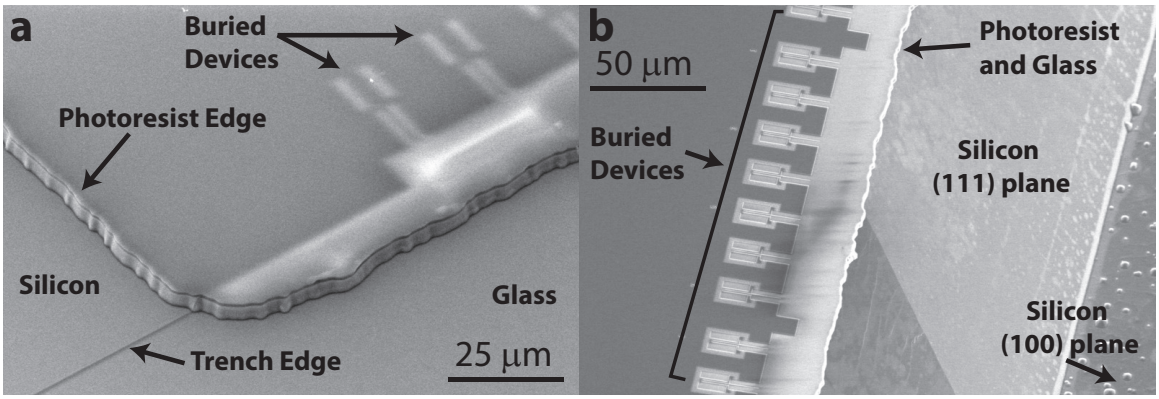

Figure 2.22: **Protective Photoresist Layer.** **a** SEM image after the application and exposure of the PSB photoresist protective mask. For illustrative purposes, in this image the mask extends $\sim 20\,\mu$m from the buried device edge, while in optimally fabricated devices this separation is $< 5\,\mu$m in order to avoid optical absorption in the silicon substrate. **b** SEM image of the trench feature after plasma etching the exposed glass and TMAH etching the silicon substrate. The devices are still buried by PSB photoresist on their top surface and glass on their bottom surface.

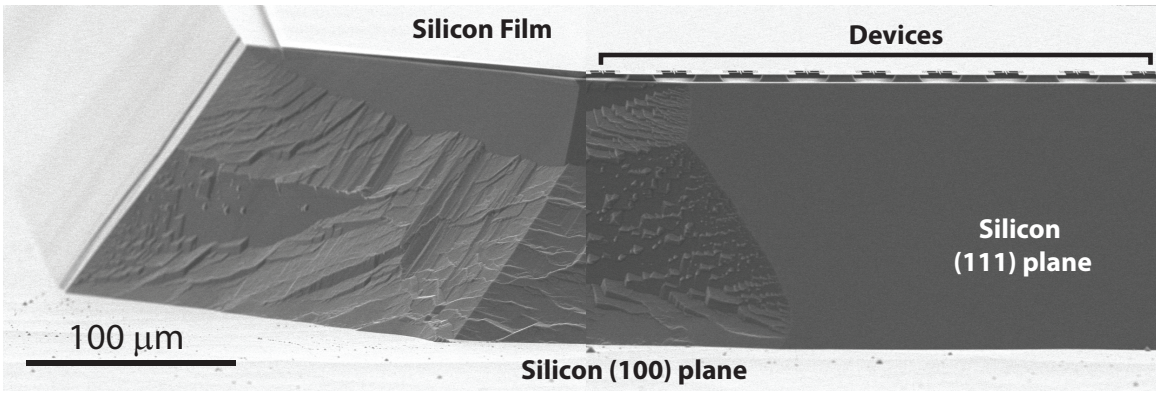

Figure 2.23: **Sample Mesa Feature.** A fully fabricated sample, with two SEM images stitched together to show the sample mesa feature surrounded by the optical fiber access trench.

of the trench walls defined during the anisotropic TMAH etch. Because of this angle, after light is launched from a lensed fiber oriented below the device layer height, the light reflected from the (111) plane trench wall is not recollected by the fiber, and the reflection signal measured on a photodiode is small. Similarly, when the fiber is oriented at a height above the device layer, there are no reflective surfaces. Therefore, when varying the z-position of the lensed fiber in sufficiently small increments ($\sim 1\,\mu$m), the optimal height can be determined by a maximum in optical reflection. This procedure enables fiber alignment without the use of an imaging system, greatly simplifying operation in a dilution refrigerator. In the fiber positioning system utilized here, the sample is secured to a gold-coated copper mounting block, which is fixed to the mixing chamber plate of a BlueFors BF-LD dilution unit. The fiber tip is mounted to the top of a 3-linear-axis stack of cryogenic nanopositioner

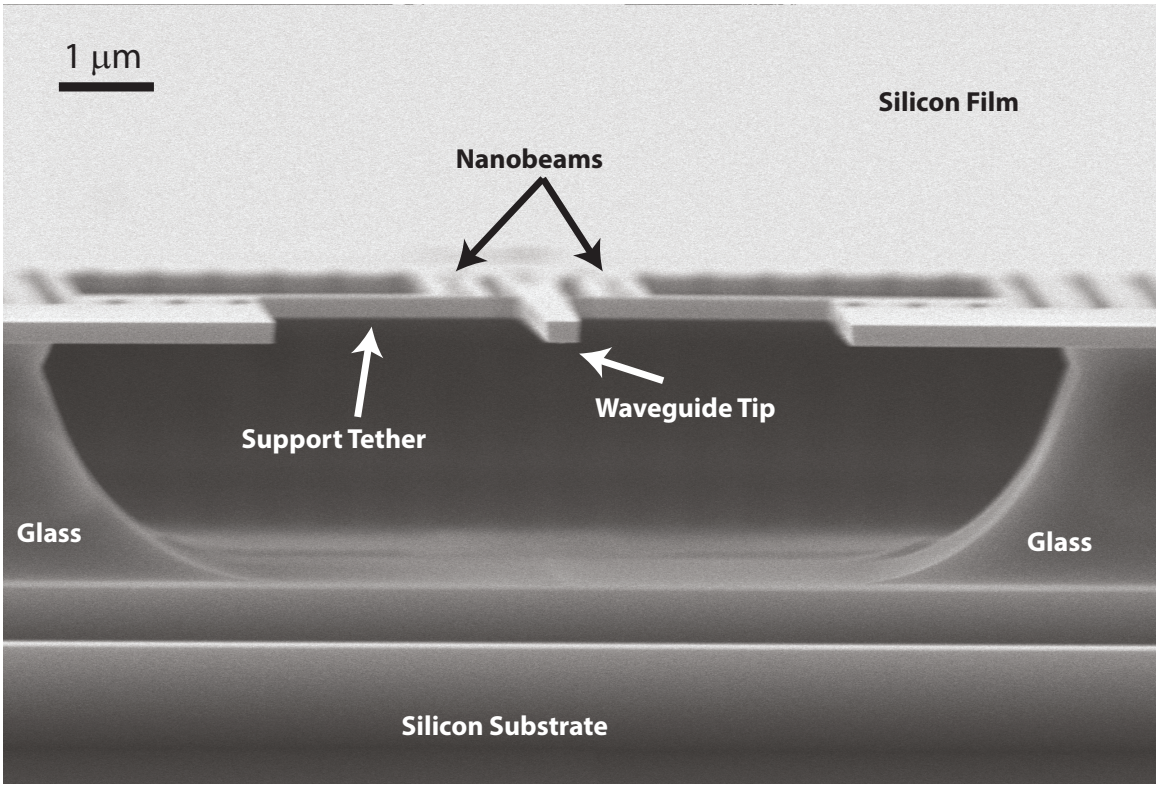

Figure 2.24: **Fabricated End-fire Device.** Edge-view SEM image of a fully fabricated device, showing the suspended nanobeam resonators and central waveguide taper.

stages (attocube ANPx101 series). The fiber extends less than 5 mm from the edge of the stage assembly; longer extensional lengths lead to cantilever-like motion of the fiber driven by motion in the cryogenic system (such as caused by pulse-tube cooler oscillations).

During initial fiber coupling, the aforementioned reflection maximum is only apparent with significant amounts of laser power ($> 1\,\mathrm{mW}$) and for x separations between fiber and device of $< 250\,\mu\mathrm{m}$. To facilitate the coarse x position of the fiber, a portable imaging system is used in a pre-alignment procedure. As it is undesirable to expose a high-quality device to ambient room conditions due to surface-adsorption of moisture and other contaminants, the pre-alignment quickly uses imaging feedback from the microscope assembly to coarsely position the fiber proximity to the sample, such that the following z-positioning procedure will successfully locate the device layer without image feedback. An example image of a pre-aligned fiber (positioned with the fiber retracted $200\,\mu\mathrm{m}$ in x and $200\,\mu\mathrm{m}$ in z) is shown in Fig. 2.27c.

After pre-alignment, the vacuum cans and radiation shields of the dilution refrigerator are put in place and the system is evacuated. The sample is then fiber-coupled by first locating the device layer in z, and then iteratively approaching the sample in x and further optimizing z as reflection increases. When device optical modes become apparent in reflection, optical polarization should

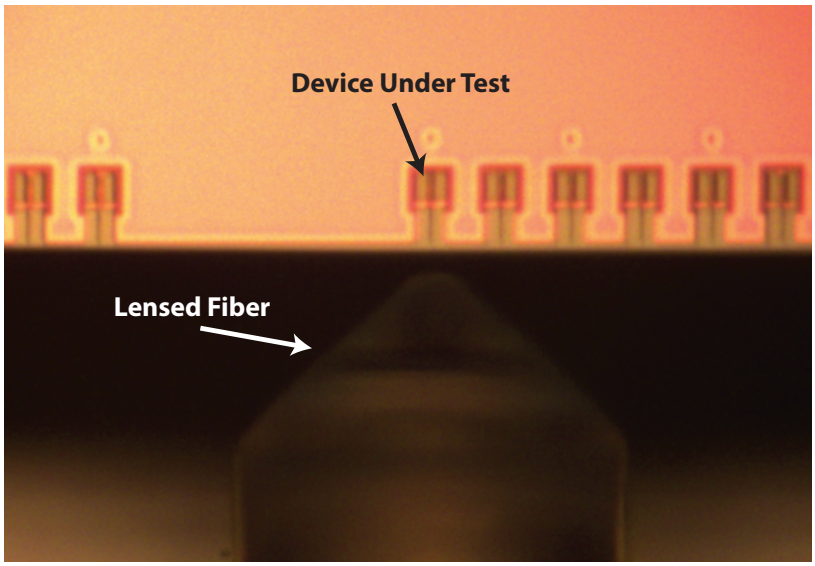

Figure 2.25: **Room Temperature End-Fire Alignment.** Microscope image obtained in the room-temperature fiber alignment station, showing a lensed fiber tip in optimal coupling position to a device.

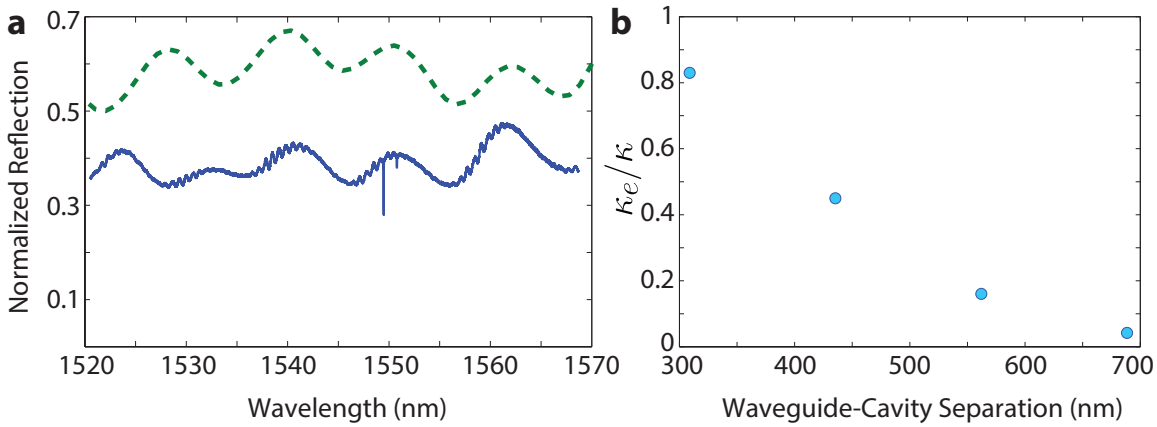

Figure 2.26: **End-Fire Optical Characterization.** **a** Normalized optical reflection spectrum measured after fiber coupling to a device at room temperature. The low-visibility wide-band fringe pattern is produced by a short optical cavity created between the photonic crystal mirror and the 1% reflectivity optical fiber lens. The sharp reflection dips at wavelengths $\lambda = 1550$ nm and $\lambda = 1551$ nm correspond to individual fundamental optical modes of each of the two side-coupled nanobeam resonators. The dashed green line shows the optimal reflection predicted by FEM simulation of the full device with the geometrical parameters given in the design section. **b** Tuning the separation gap between the nanobeam and central waveguide allows κ_e/κ to be tuned from overcoupled to undercoupled.

be adjusted to maximize coupling depth, and the y coordinate should begin to be iteratively tuned along with x and z. Eventually the maximum reflection will be reached at the optimal fiber position for a particular device.

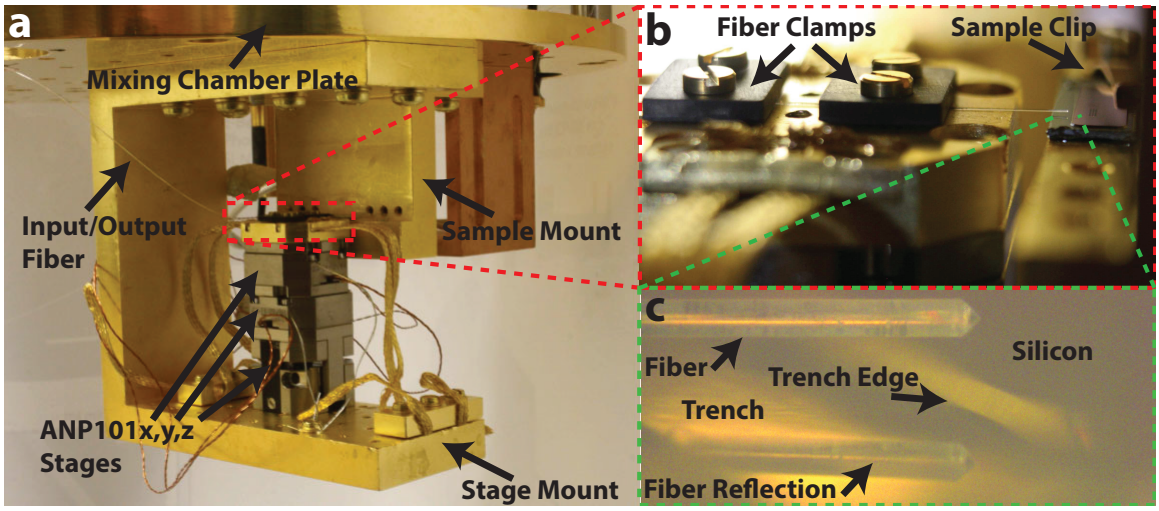

Figure 2.27: **Fiber Coupling in the Dilution Refrigerator. a** Photograph of the alignment stage and sample mount assembly beneath the mixing chamber plate of the BlueFors dilution refrigerator. **b** Detailed view of the fiber mount on top of the translation stage stack. **c** Microscope image obtained using the pre-alignment imaging system, showing the fiber raised 200 μm and retracted 200 μm from the optimal coupling position.

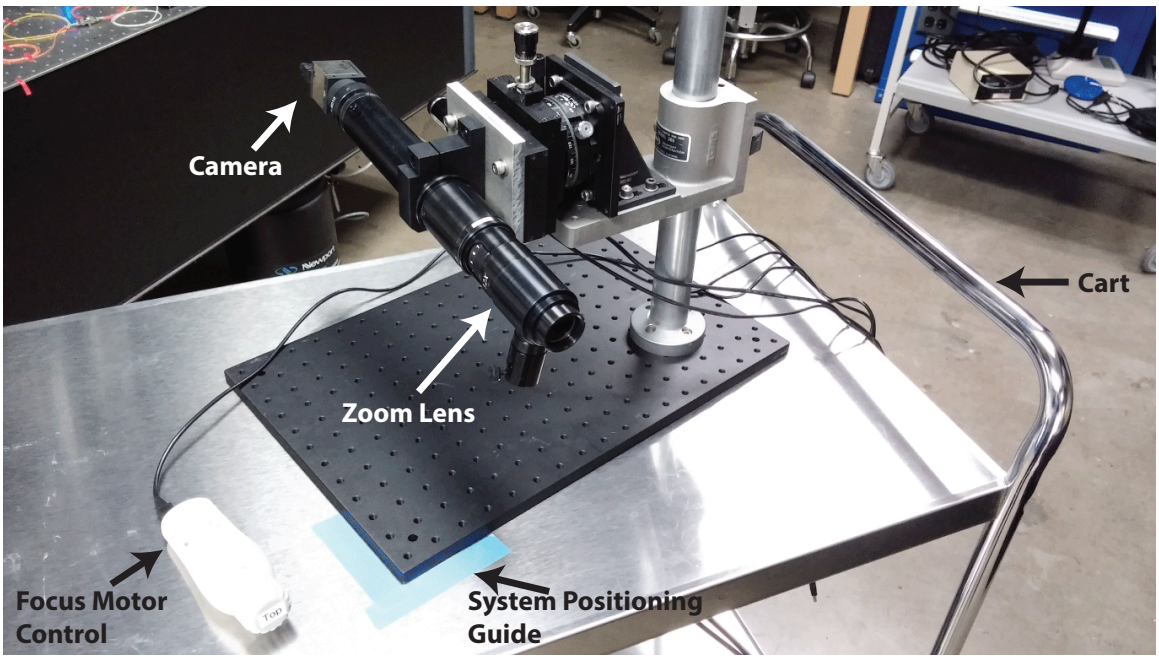

Figure 2.28: **Pre-alignment Imaging System.** The portable imaging system uses a Navitar 12x zoom lens and dynamic focusing to quickly locate the fiber coupling location to the sample under test. The cart is placed adjacent to the dilution refrigerator, while the electrical tape markings on the cart surface indicate the coarse position of the imaging system for viewing the sample.

Due to thermal contraction of the various mounting blocks in the fridge, the fiber should be retracted from the optimal coupling point before cooling down the system. A distance of 100 μm

has been found to sufficiently separate the sample and fiber to avoid harmful contacts, and is small enough in distance that the coupling procedure can be quickly repeated after the system reaches 4 K. Performing the fiber coupling before the dilution process begins is preferrable due to the fact that electrical actuation of the nanopositioner stages causes heating at sub-Kelvin temperatures. Thermal contraction is small between 4 K and 10 mK, so the fiber is aligned at 4 K and then the stages are fixed in position. An example narrow-band optical reflection spectrum measured after fiber-coupling to a device at 4 K is shown in Fig. 2.29. Grounding of the attocube nanopositioning stages results in extremely stable fiber placement, with alignment periods of up to two months showing no noticeable drift over time (indicated by a constant coupling efficiency).

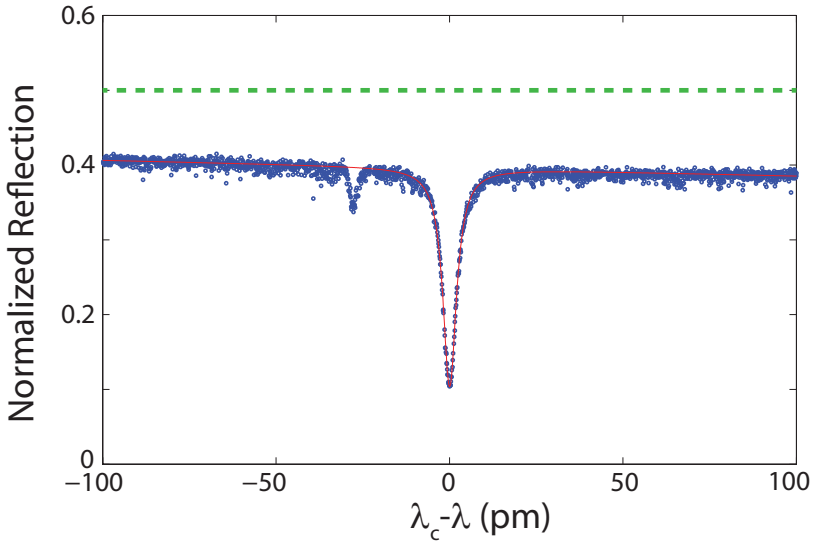

Figure 2.29: **Cryogenic Optical Characterization.** Narrow-band optical reflection spectrum from an end-fire device fiber coupled at 4 K. The normalized reflection is plotted in blue points, with a Lorentzian lineshape fit plotted in red. The dashed green line shows the optimal reflection predicted by FEM simulation of the geometrical parameters of the device under test.

Chapter 3

Near-Quantum-Limited Displacement Measurement

The precise monitoring of the motion of an object is an essential capability for a variety of tasks in both the classical and quantum domain. Classical force sensors such as accelerometers and gravitational wave observatories are limited by the sensitivity to displacement of a test mass [94–97], and applications in biosensing often depend on precise trajectory tracking of individual molecules [98]. Similarly, quantum state engineering using mechanical motion relies on efficiently resolving states of the system. The ability to achieve continuous, high-precision displacement readout for any of these applications ultimately hinges on the detection efficiency with which motion is measured.

Even for ideal, loss-less detection, however, the sensitivity to motion is bounded to a lower limit determined by quantum mechanical uncertainty relations [14, 16, 61]. Past this limit, termed the standard quantum limit (SQL) [34, 61, 62], increasingly precise measurements of a quantum observable are made at the cost of increasing disturbance the complementary observable. This trade-off results in measurement noise of at least the level of the oscillator zero-point fluctuations (ZPF). Nanoscale mechanical oscillators are capable of achieving excellent displacement and force sensitivity due to their small levels of ZPF, but such systems in the optical domain are limited to well above the SQL due to inefficiencies in collecting light from chip-based devices. In this chapter I will describe a near-quantum-limited position measurement of a V-groove-coupled zipper optomechanical resonator [99].

3.1 Standard Quantum Limit of Measurement

The Heisenberg uncertainty principle for observables pertaining to mechanical motion enforces a strict limit on the sensitivity with which an observable (such as position) can be measured before disturbing the complementary observable (momentum). However, a minimum uncertainty limit exists even for measurements of classical signals. While some techniques such as back-action eva-

sion [100, 101] can side-step the SQL, the continuous monitoring of position required for precision sensors is limited by the quantum mechanical properties of the transducer, in this case of light. Light, due to its particle nature, carries shot noise which scales linearly with optical power. In an optomechanical measurement of position, the optical shot noise within the resonator exerts force and drives mechanical motion. In the context of a passive measurement of position, this driven motion is considered as back-action noise.

The SQL arises from the fact that the linear scaling of back-action noise is opposite to the scaling of signal-to-noise ratio (SNR) in the transduced signal. An optomechanical measurement of position consists of measuring the intensity and phase shifts on the probe beam of light through Eqns. 1.4 and 1.5. The state of mechanical resonator is often measured for an arbitrary quadrature operator

$$\hat{X}_\theta = \hat{a}(t)e^{-i\theta} + \hat{a}^\dagger(t)e^{i\theta}. \tag{3.1}$$

The choice of quadrature angle θ determines the proportion of modulation signal due to intensity or phase shifts in the cavity radiation, and can be optimized for a particular set of experimental conditions. For any quadrature however, the modulation signal is proportional to the average mechanical mode occupancy $\langle n \rangle$, and is converted and amplified into electrical signals for spectrum analysis via photoelectric detection. In a practical measurement, the output photocurrent will include a noise floor in addition to the modulation signal, and the SNR limits the sensitivity of the measurement. In the formalism of noise power spectral density (NPSD), defined for an arbitrary operator $\hat{O}$ as $S_{OO}(\omega) = \int_{-\infty}^{\infty} d\tau e^{i\omega\tau} \langle \hat{O}^\dagger(\tau)\hat{O} \rangle$, the mechanical oscillator position NPSD

$$S_{xx}(\omega) = x_{\mathrm{ZPF}}^2 \gamma \frac{\langle n \rangle + 1/2}{(\omega_{\mathrm{m}} - \omega)^2 + \gamma^2/4} \tag{3.2}$$

is imprinted on the photocurrent NPSD

$$S_{II}(\omega) = 2\frac{G_{\mathrm{conv}}}{Z}\Big(S_{\mathrm{imp}}(\omega) + AS_{xx}(\omega)\Big) \tag{3.3}$$

through an optomechanical transduction constant A, photodetector conversion gain G_{conv}, and spectrum analyzer impedance Z. The noise floor of S_{II} is incorporated into an imprecision NPSD, S_{imp}, given by the inverse of SNR converted into units of optical power.

S_{imp} can be minimized (SNR improved) either by reducing classical sources of noise, such as that of amplifiers and oscillators in spectrum analyzers, or by maximizing the desired modulation signal. Assuming that the optomechanical coupling and optical collection efficiency are already optimized, the remaining path to increasing signal strength is by raising the power of the optical probe, producing a linearly proportional increase to the output. When extracting S_{xx} from S_{II} through Eqn. 3.3, increasing probe power then lowers the effective noise floor, S_{imp}, from the calibrated mechanical

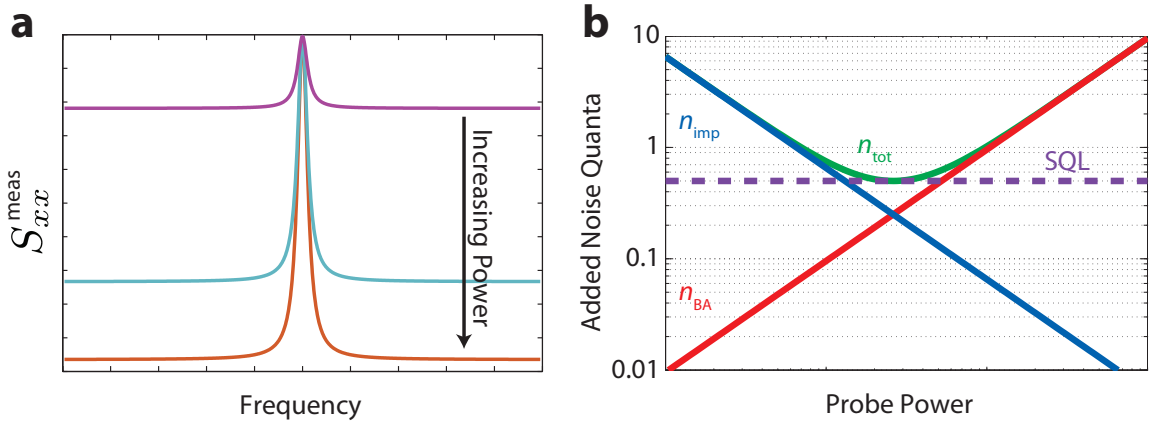

Figure 3.1: **Standard Quantum Limit.** **a** Illustration of the increase in SNR as input power is increased. The measured NPSD of position $S_{xx}^{\rm meas}$, as extracted from S_{II}, features a Lorentzian peak determined by its thermal occupancy and a noise floor that lowers in magnitude as the signal strength is increased. **b** Measurement sensitivity in units of added noise quanta as a function of probe power. The SQL is defined as the minimum added noise value for an ideal measurement.

response peak, as shown in the example spectra of Fig. 3.1a.

The added noise contributed to an optically resonant position measurement by the imprecision noise floor and by back-action are, in units of mechanical occupation number,

$$n_{\rm imp} = \frac{\kappa^2\gamma}{64 n_{\rm c} g_0^2 \kappa_{\rm e} \eta}, \tag{3.4}$$

$$n_{\rm BA} = \frac{4 n_{\rm c} g_0^2}{\kappa\gamma}. \tag{3.5}$$

These noise terms are plotted in Fig. 3.1b for the case of an ideal measurement, in which the total detection efficiency of cavity radiation $\eta = 1$ and the optical coupling is perfectly over-coupled with $\kappa = \kappa_{\rm e}$. The minimum total added noise $n_{\rm tot} = n_{\rm imp} + n_{\rm BA}$ occurs for the input probe power at which $n_{\rm imp} = n_{\rm BA}$. In the ideal case, these contributions are both equal to 1/4 quanta of noise, and the SQL occurs at $n_{\rm min} = 1/2$, equal to the zero-point fluctuations of the oscillator [14, 61]. For non-ideal measurements,

$$n_{\rm min} = (n_{\rm imp} + n_{\rm BA})_{\rm min} = \frac{1}{2\sqrt{\eta\kappa_{\rm e}/\kappa}}. \tag{3.6}$$

Although experiments in both the optical and microwave domains have brought the imprecision noise level down to below 1/4 quanta [62, 64], and recent microwave experiments have achieved a total added noise within a factor of 4 of the SQL [50], current state-of-the-art optical devices have been limited to $14-80$ times the SQL [33, 42, 51]. Such experiments are limited partly by technical noise (e.g., added noise from amplifiers), but a substantial amount of imprecision is introduced by poor quantum efficiency of the optical readout. In this regard, both the high efficiency and the

single-sided coupling of the V-groove fiber coupler are advantageous over methods such as fiber taper coupling to photonic-crystal-based optomechanical resonators.

3.2 Homodyne Spectroscopy

Due to the large optomechanical coupling of zipper cavity resonators, low optical probe power is imperative to avoid large back-action noise. Homodyne interferometry is an elegant experimental method for amplifying small amplitude signals while adding little excess noise. The interference of an optical signal beam with a strong local oscillator (LO) beam optically amplifies the signal prior to photodetection, which is desirable over electrically amplifying the photocurrent carrying excess photodiode noise. The two beams $\hat{a}_{\rm sig}$ and $\hat{a}_{\rm LO}$ are combined with a 50/50 beam splitter and the output ports are each detected on a photodiode. The field operator $\hat{a}_{\rm sig}$ emanates from the output of the optomechanical resonator, and $\hat{a}_{\rm LO}$ represents an LO beam derived from the same optical source as the signal beam, with power $\hbar\omega_{\rm c}|\alpha_{\rm LO}|^2 \gg \hbar\omega_{\rm c}|\alpha_{\rm sig}|^2$. Assuming that the quantum efficiencies of the two photodiodes are exactly equal and that the beam splitter is a perfect 50/50 coupler, the difference between the two photocurrents is

$$\hat{I}(t) = \hat{a}_{\rm sig}\hat{a}^{\dagger}_{\rm LO} + \hat{a}^{\dagger}_{\rm sig}\hat{a}_{\rm LO}. \tag{3.7}$$

Decomposing both LO and signal into noise and large coherent tones, and discarding terms second order or greater in noise operators,

$$\hat{I}(t) = |\alpha_{\rm LO}|\hat{X}^{\rm sig}_{\theta} + I_{\rm DC}\big(1 + 2{\rm Re}\big\{\xi(t)\big\}\big), \tag{3.8}$$

where $\xi(t) = \delta n(t) + i\delta\phi(t)$ includes fluctuations in intensity $\delta n(t)$) and phase ($\delta\phi(t)$) originating from the laser source, and the DC photocurrent component $I_{\rm DC} = 2|\alpha_{\rm sig}\alpha_{\rm LO}|\cos\theta$ is determined by shot noise of the LO as well as the phase difference between signal and LO [99, 102].

Eqn. 3.8 shows that large LO amplitude amplifies the measured quadrature signal $\hat{X}^{\rm sig}_{\theta}$ as well as raises the DC noise floor. Fortunately, the DC noise floor arising from shot noise of the LO does not obscure the signal proportional to $\hat{X}^{\rm sig}_{\theta}$, unlike other incoherent noise backgrounds. The LO power should thus be chosen such that the optically amplified signal is much larger than other electronic noise apparent in the measured spectrum. The fiber-based optical homodyne interferometer shown in Fig 3.2 accomplished this by splitting the source laser into a $\sim 1\,$mW LO and $\sim 1\,$nW signal beam. The LO propagates through an electrically-tunable fiber stretcher (FS), which imparts a variable time delay for phase control, before interfering with the signal beam, itself having circulated through and reflected from the device under test (DUT). The combined beams are detected on a balanced pair of photodiodes (BPD). The variable beam splitter (VBS2) used to combine the LO and signal

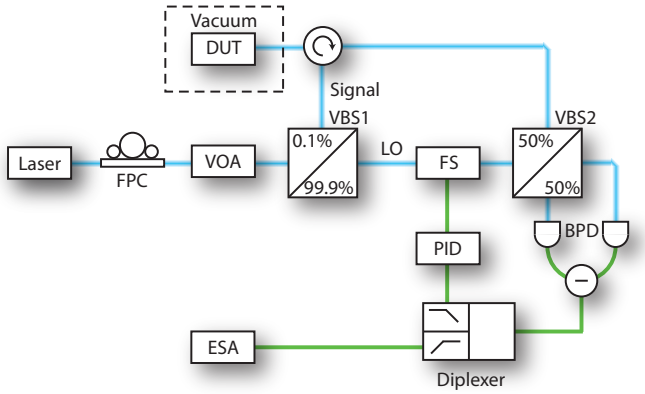

Figure 3.2: **Homodyne Interferometer.** Optical circuit for homodyne detection of mechanical motion. Abbreviations are defined as FPC: fiber polarization controller, VOA: variable optical attenuator, VBS: cariable beam splitter, DUT: device under test, LO: local oscillator, FS: fiber stretcher, BPD: balanced photodetector pair, PID: proportional-integral-derivative servo, and ESA: electronic spectrum analyzer.

beams has a tunable reflection/transmission ratio, which is used to adjust the amount of optical power incident on each photodiode. This adjustment balances the detection in the case of non-identical quantum efficiencies of each photodiode.

The difference current output of the BPD is filtered, or dediplexed, into low-frequency (< 200kHz) and high-frequency (> 200 kHz) components. The high-frequency signal is sent to an electronic spectrum analyzer (ESA), while the low-frequency component is used as the input to a proportional-integral-derivative (PID) servo module. The output of the servo is fed into the fiber stretcher, and closing of the servo loop results in a stable lock of the phase difference between signal and LO. The set-point of the PID lock then controls the quadrature angle of $\hat{X}_\theta$, and can be used to optimize the SNR of a given measurement.

3.3 Imprecision Measurement

As dynamic back-action (Eqn. 1.7) induced by optical pumping with a laser detuned from the cavity resonance is undesirable in the context of a passive position measurement, the following imprecision measurement uses resonant optical probing of the zipper resonator. Resonant detection also has a lower imprecision/back-action product limit than detuned measurements [50, 61, 63], further increasing the attainable sensitivity. The sample is placed in an evacuated environment to enable high mechanical quality factor by avoiding squeezed-film damping. The probe laser frequency is then positioned on resonance (Fig. 3.3) without frequency-locking to the cavity, as drift is found to be negligible over the time span of the measurement (~ 100 s). Tuning the LO phase via the FS, the SNR of the mechanical NPSD is maximized (corresponding to the phase quadrature angle).

With a probe power of 10 nW, $S_{II}(\omega)$ as transduced on the ESA is plotted in Fig. 3.4. The LO shot noise sets the noise floor of the spectrum (blue curve, measured with a blocked signal beam) to several dBm above the combined electronic noise of the BPD and RSA (orange curve, measured with blocked signal and LO beams).

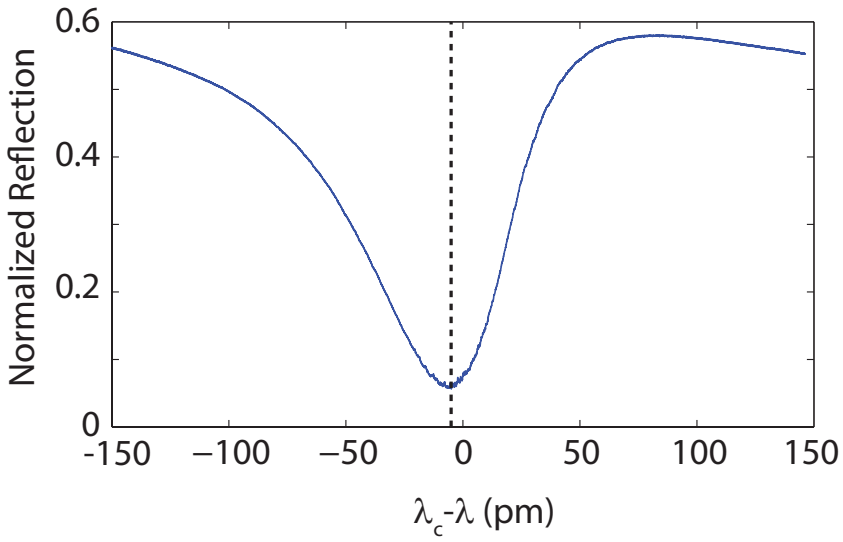

Figure 3.3: **Optical Spectrum.** Narrow-band optical reflection spectrum from the V-groove coupled device in vacuum, with the laser detuning used for the imprecision measurement indicated by the dashed vertical line.

The NPSD reveals a prominent resonance at $\omega = 3.3$ MHz, which is identified using FEM simulations as the fundamental in-plance mechanical mode of the test nanobeam. The optomechanical coupling rate of this mode, calibrated through the optical spring shift, is $g_0/2\pi = 350$ kHz. A second prominent resonance occurs at $\omega = 3.15$ MHz, which is identified as the fundamental in-plane mechanical mode of the waveguide beam, with a lower optomechanical coupling ($g_0/2\pi = 135$ kHz) owing to the small overlap between the mechanical and optical modes. Overlays of the prediced single-sided transduction spectra, calculated using the measured parameters of the optomechanical cavity and fiber coupler, show good agreement with the measured signal for both the test beam (dashed green curve) and the waveguide (dashed red curve). Other peaks at 3 MHz, 3.2 MHz, and 3.4 MHz do not correspond to any real mechanical motion of the beam, but rather are due to nonlinear transduction of the mechanics. Thermal Brownian motion of the beams, combined with the large optomechanical coupling, gives rise to a frequency shift of the optical mode that is a substantial fraction of the cavity optical linewidth, leading to harmonics in $S_{II}(\omega)$ at multiples of the sum and difference frequencies of the two mechanical modes [103]. The remaining small features in $S_{II}(\omega)$ are due to out-of-plane flexural modes of the structure, which are weakly transduced due to imperfect vertical symmetry.

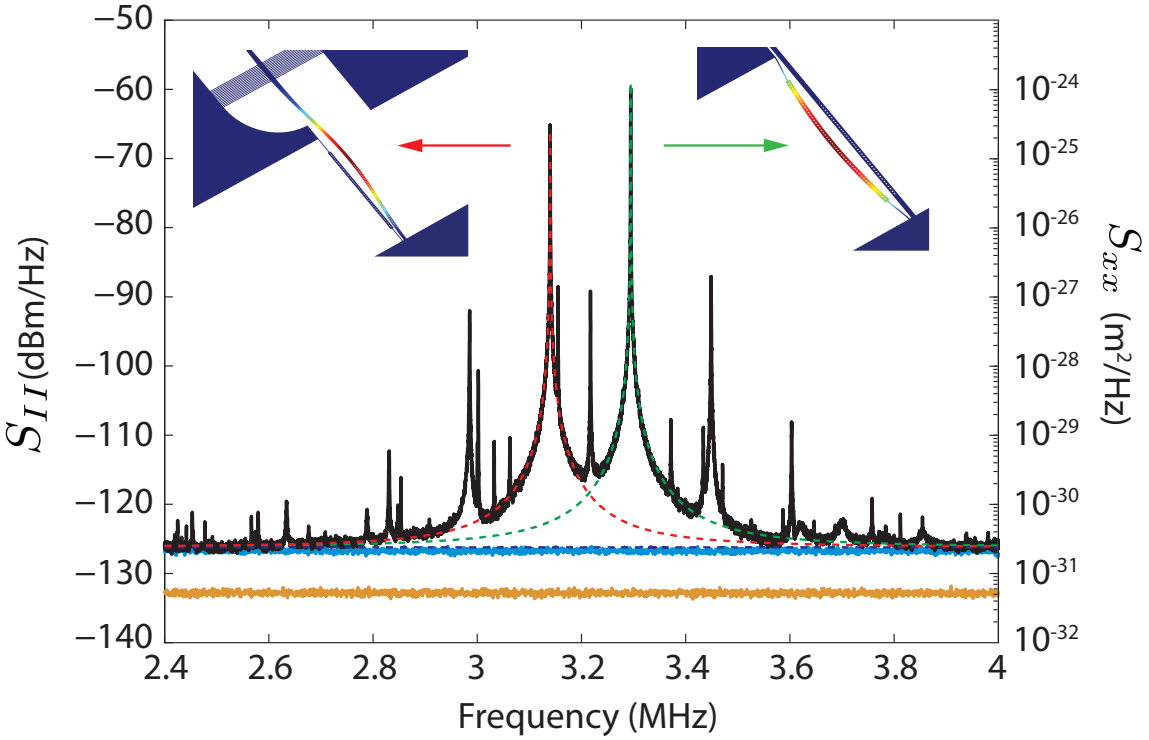

Figure 3.4: **Mechanical Spectrum.** Photocurrent NPSD $S_{II}(\omega)$ (solid black curve) measured on the ESA with 10 nW of input signal arm power. Optical shot noise (solid blue curve) sets the noise floor several dBm above electronic noise contributions (solid orange curve). The two peaks at 3.14 MHz and 3.3 MHz correspond to the first order mechanical bending modes of the waveguide and test beams, respectively. The dashed red and green curves diplay the calculated single-sided displacement NPSD of each mode, with the calculated imprecision noise floor shown in the dashed purple line. The insets show the FEM simulated mechanical bending mode profiles of each beam with their associated noise peaks indicated.

The remainder of this measurement focuses on the mechanical mode with the strongest transduction, the fundamental in-plane mode of the test beam with mechanical frequency $\omega_{\rm m} = 3.3$ MHz. The value of the single sided NPSD of displacement at the mechanical resonance frequency is given by $S_{xx}(\omega = \omega_{\rm m}) = 8x_{\rm ZPF}^2(\langle n\rangle + 1/2)/\gamma$, where $\langle n\rangle = n_{\rm th} + n_{\rm BA}$. For the fundamental in-plane mode the numerically computed effective motional mass is $m_{\rm eff} = 15$ pg, and the corresponding zero-point amplitude $x_{\rm ZPF} = 13$ fm. When the mechanical mode is well-resolved in $S_{II}(\omega)$, that is, when the contributions of nearby mechanical modes are negligible and the resolution bandwidth of the ESA is much less than $\gamma/2\pi = 150$ Hz, the spectrum can be converted into units of displacement by scaling $S_{II}(\omega = \omega_{\rm m})$ to the computed value of $S_{xx}(\omega = \omega_{\rm m})$.

The imprecision in units of quanta is determined here by referencing the measured background level to the height of the measured noise peak. That is, the number of imprecision quanta is equal to $(\langle n\rangle + 1/2)$ divided by the SNR of the resolved mechanical noise peak, so that an imprecision level

of $n_{\mathrm{imp}} = 1$ corresponds to the equivalent level of NPSD that would be produced at ω_{m} by a single phonon in the mechanical resonator. The background noise floor is taken from the average value of $S_{II}(\omega)$ from $2.4 - 2.6$ MHz, indicated by the relatively noise-free spectral region shaded gray in Fig. 3.5a.

To directly measure the additional phonon occupation due to back-action [104] it is necessary to determine the total phonon occupancy $\langle n \rangle$ by integrating over the full bandwidth of the mechanical mode. However, such a study is outside the scope of the work presented here, as the large thermal occupation at room temperature ($n_{\mathrm{th}} \approx 10^6$) dominates the signal over the comparatively small back-action n_{BA} produced by reasonable laser probe powers. For now the experiment is restricted to measuring the imprecision noise, and the backaction is assumed to be due only to the ideal radiation pressure term given in Eqn. 3.5. This assumption is supported by measurements of the properties of known noise sources such as technical laser noise, which is a common concern in optomechanical systems [46, 105, 106]. While in principle both intensity and phase noise of the laser can contribute to heating of the mechanical mode, for an optically resonant measurement of position in the sideband unresolved regime the phase noise does not contribute to back-action, and only intensity noise affects the mechanics. In this regime, the phase noise adds a small component to the imprecision noise floor. Measurements of the phase and intensity noise of the laser used in this study reveal no excess intensity noise and a flat frequency NPSD of $S_{\omega\omega} = 5 \times 10^3\ \mathrm{rad}^2$ Hz in the frequency range of interest. Consequently, for the probe powers used here, the excess back-action due to technical laser noise is negligible, and the phase noise contribution to the noise floor lies about 60 dB below the shot noise. As there exist additional, unknown sources of excess back-action in this measurement, the emphasis here is placed on the collection efficiency of the coupling scheme, and that back-action and noise-driven occupation levels are used only to compare the ideal quantum limits of the device to the SQL.

The spectrum exemplified in Fig. 3.4 is measured for a range of probe powers (Fig. 3.5a), and the extracted n_{imp} is plotted in Fig. 3.5b with calculations of imprecision (solid blue line), ideal quantum back-action (solid red line), and total (solid green line) noise quanta. Losses in the optical circuit from device to BPD comprise an experiment-specific apparatus efficiency of $\eta_{\mathrm{meas}} = 36\ \%$, while the fiber collection efficiency of intracavity photons $\eta_{\mathrm{CE}} = \eta_{\mathrm{cpl}}\kappa_{\mathrm{e}}/\kappa = 0.86 \times 0.7 = 0.52$. For comparison, systems in which ground-state occupancy of a single mechanical mode has been achieved have featured $\eta_{\mathrm{CE}} = 37\ \%$ [50] and $\eta_{\mathrm{CE}} = 9\ \%$ [42]. The combination of total detection efficiency with the electronic noise floor brings the imprecision level of the measurement to 2.8 times the ideal imprecision of a loss-less device (shown in the dashed blue line). The predicted total minimum added noise is thus $n_{\mathrm{min}} = 1.4$ phonons. This minimum total added noise can be compared to similar measurements of mechanical position in the optical [64, 104] and microwave [62] domains. The coupling scheme presented here compares favorably to the minimum total added noise of $n_{\mathrm{min}} \approx 3.2$ demon-

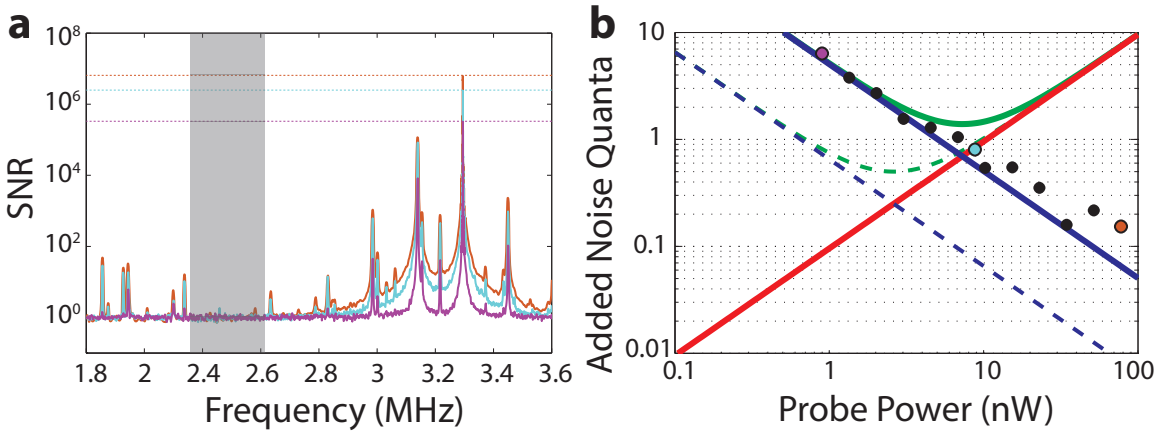

Figure 3.5: **Signal-to-Noise Ratio and Imprecision.** **a** Signal-to-noise ratio (SNR) of $S_{II}(\omega)$ measured with 880 pW (magenta), 8.6 nW (cyan), and 76 nW (orange) probe power from which the imprecision point of corresponding color is extracted in **b**. The dashed peak levels are referenced to the background level indicated by the gray shaded region. **b** Noise quanta versus probe power. Measurements of imprecision are plotted with calculated imprecision (blue), estimated back-action (red), and total (green) noise quanta, plotted in solid curves for the device under test and dashed curves for an ideal measurement.

strated with whispering-gallery-mode resonators [64], $n_{\mathrm{min}} \approx 0.82$ demonstrated with membranes in Fabry-Perot cavities [104], and $n_{\mathrm{min}} \approx 1.2$ demonstrated with microwave resonators [62].

Alternatively, one can compare to state-of-the-art ground state cooling experiments [42, 50, 51] where the occupation of the mechanical resonator is brought near or below a single phonon, and the quantum limits of the mechanical measurement become crucial. In such experiments, back-action is used to passively cool the mechanical resonator, and thus the relevant noise term is simply n_{imp}. In the red-detuned, sideband-resolved regime relevant for ground-state cooling, the imprecision cannot be made arbitrarily small by increasing the power, but rather has the asymptotic form $n_{\mathrm{imp}} = 1/(4\eta_{\mathrm{CE}}\eta_{\mathrm{meas}})$ in the limit of large intracavity photon number. Such a measurement using the V-groove coupling scheme would achieve $n_{\mathrm{imp}} = 1.34$, which lies well below the imprecision level previously demonstrated using similar nanoscale optomechanical cavities ($n_{\mathrm{imp}} = 20$) [42], and is comparable to the imprecision achieved in whispering-gallery-mode resonators ($n_{\mathrm{imp}} = 3.6$) [51] and microwave resonators ($n_{\mathrm{imp}} = 1.9$ [50]).

It is worth noting that improvements to η_{meas} of the optical circuit, such as higher efficiency photodiodes, can lower n_{min} to below 1 quantum. Another key application which benefits greatly from the improved collection efficiency demonstrated here is feedback damping of the mechanical motion [65, 107–110], which is fundamentally limited by the imprecision noise and could enable ground state cooling of sideband unresolved systems, such as the zipper resonator.

Chapter 4

Heterodyne Spectroscopy and Single Photon Detection

4.1 Mechanical Spectroscopy at milliKelvin Temperatures

The previous chapter reported a precision position measurement using homodyne interferometry and spectral analysis. A similar measurement, seeking to detect cryogenic cooling to motional ground states, was later performed at mK temperatures with an end-fire coupled silicon optomechanical crystal [111]. While this experiment is described in detail in the thesis of Seán Meenehan [27], a few key results will be summarized here due to their relevance in motivating single phonon counting measurements.

4.1.1 Heterodyne Interferometry

As explained in Section 2.2, a nanobeam optomechanical crystal is mounted to the mixing plate of a dilution refrigerator, and end-fire coupled to a lensed fiber tip at sub-Kelvin temperatures. The detection method is similar in principle to the homodyne interferometer of Chapter 3, but differs in that here the LO is frequency shifted from the probe signal beam by $\omega_{\rm m}/2\pi - 50\,\text{MHz}$. The high mechanical frequency ($\omega_{\rm m}/2\pi \sim 3.5\,\text{GHz}$) of the resonator lies will above the bandwidth of the balanced detector ($\sim 100\,\text{MHz}$), so the heterodyne interference generates a detectable beat note at the difference frequency of $\sim 50\,\text{MHz}$.

In the experimental apparatus of Fig. 4.1, the laser is tuned to the frequency of either the blue or red motional sideband of the nanobeam resonator. For sideband-resolved systems such as the nanobeam device, where $\omega_{\rm m} > \kappa$, resonant enhancement of sideband-scattered light produces the largest transduction of mechanical motion at laser detunings of $\Delta = \pm\omega_{\rm m}$. A small portion of the laser power is collected on a wavelength-meter (λ-meter), which feeds back on the piezoelectric actuator of the laser cavity to stabilize the laser frequency against drifts in time. The remaining laser power is split into signal and LO paths, where the LO is frequency shifted by an electro-optic

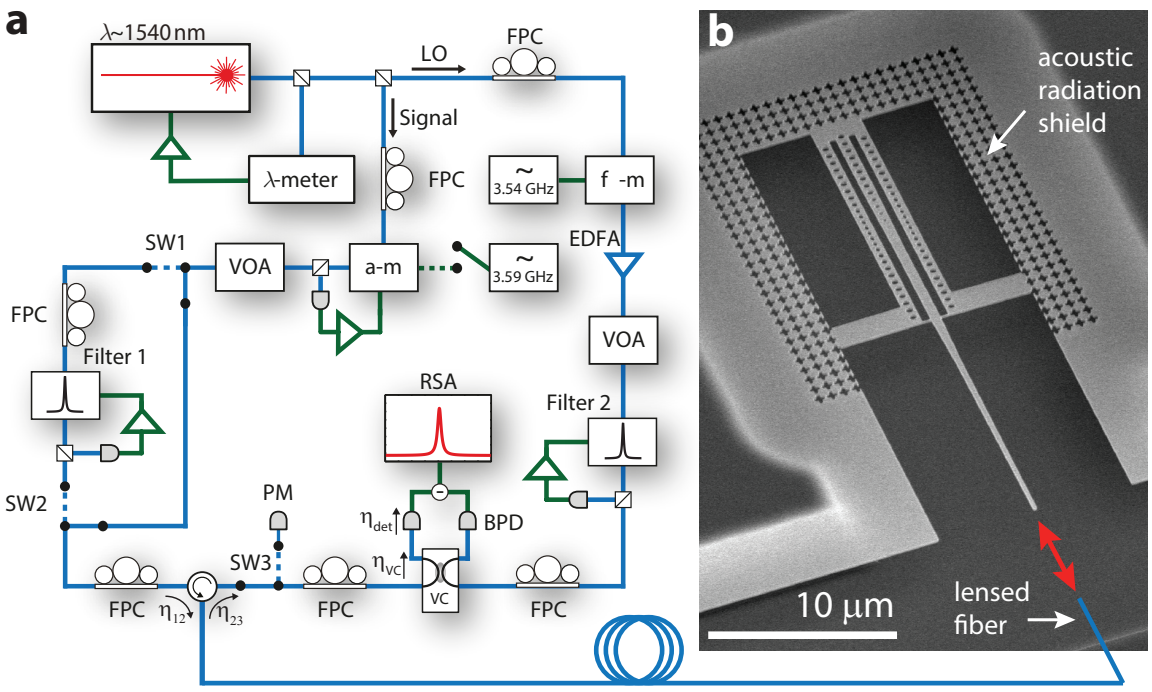

Figure 4.1: **Heterodyne Interferometer Setup.** **a** Diagram of the heterodyne interferometer for cryogenic spectum analysis of an end-fire coupled optomechanical crystal, shown in SEM in **b**. Abbreviations are defined as LO: local oscillator, λ-meter: wavelength meter, FPC: fiber polarization controller, f-m: electro-optic frequency modulator, a-m: electro-optic amplitude modulator, VOA: variable optical attenuator, EDFA: erbium-doped fiber amplifier, SW: optical switch, PM: power meter, VC: variable coupler, BPD: balanced photodiode, and RSA: real-time spectrum analyzer.

frequency modulator (f-m), itself driven by a signal generator at $\omega_m/2\pi - 50\,\text{MHz} = 3.54$ GHz. The LO is then amplified by an erbium-doped fiber amplifier (EDFA) and controlled in optical power by a variable optical attenuator (VOA). Of the multiple frequency components in the frequency-modulated LO spectrum, one tone is selected by filtering with a high-finesse Fabry-Perot filter (Micron Optics FFP-TF2). The resonance transmission band of the filter (bandwidth of 50 MHz) is tunable via electrical actuation of a piezoelectric motor. Either the higher- or lower-frequency first-order modulation sideband is selected by controlling the tuning voltage setpoint. A small optical pickoff of the transmitted power is directed to a photodiode, with the measured voltage used as the input to a proportional-integral-derivative (PID) servo feeding back on the filter setpoint. The higher (lower) frequency LO sideband is selected to generate the heterodyne beat note for laser probing of the blue (red) motional sideband.

The signal beam polarization and power are controlled before propagating to an optical circulator, which directs the input signal to the dilution refrigerator and nanobeam device (Fig. 4.1b). The reflection from the device propagates along the same fiber path before being circulated to a variable fiber coupler (VC), which combines the signal and LO beams. The VC outputs are detected

on a balanced pair of photodiodes (BPD) with the difference current measured on a real-time spectrum analyzer (RSA). The photocurrent NPSD $S_{II}(\omega)$ as transduced on the RSA is proportional to $S_{bb}(\omega) = \langle n \rangle \gamma / ((\omega - \omega_{\mathrm{m}})^2 + \gamma^2/4)$ through the optomechanical system parameters and the detection efficiency of intracavity photons $\eta_{\mathrm{meas}}\eta_{\mathrm{cpl}}\kappa_{\mathrm{e}}/\kappa$. Calibration of these parameters then enables mechanical thermometry through integration of the NPSD to extract the proportional average phonon occupation $\langle n \rangle$.

Cailbration of the detection efficiency begins with measuring the optical tranmission of the circulator from port 1 to port 2 ($\eta_{12} = 88\,\%$) and from port 2 to port 3 ($\eta_{23} = 84\,\%$). These values, measured once when the optical components are connected and do not change, are used to determine the reflection efficiency of the device and the overall detection efficiency of the heterodyne setup. To measure device reflection efficiency, the laser is tuned off-resonance from the optical mode (where the device should act as a near-perfect mirror) and a continuous-wave signal of input power P_{in} is sent into port 1 of the circulator, leading to a power $\eta_{12}P_{\mathrm{in}}$ exiting port 2 of the circulator. The optical losses incurred in the path from port 2 to the device under test are accumulated into the efficiency factor η_{cpl}, which includes signal loss in the fiber path through the dilution refrigerator and fiber coupling losses in the end-fire coupler of the device. These losses are incurred twice in reflection back to the circulator, so a power of $\eta_{\mathrm{cpl}}^2\eta_{12}P_{\mathrm{in}}$ propagates back to the circulator, and $\eta_{23}\eta_{\mathrm{cpl}}^2\eta_{12}P_{\mathrm{in}}$ emerges from port 3. An optical switch (SW3) is used to send this signal to a power meter (PM), and thus the coupling efficiency is determined to be

$$\eta_{\mathrm{cpl}} = \sqrt{\frac{P_{\mathrm{PM}}}{\eta_{23}\eta_{12}P_{\mathrm{in}}}} = 34\,\%. \tag{4.1}$$

The remaining heterodyne setup efficiency includes the intrinsic quantum efficiency of the BPD, the alignment of polarization between the LO and the signal, and the degree to which the LO power overcomes electronic noise of the detector. This is measured by using an amplitude modulator (a-m) in the signal path to create a calibration tone of known power which can be transduced on the RSA. The probe laser is tuned off resonance from the optical cavity and signal sidebands are produced by modulating at the mechanical frequency. The optical switches SW1 and SW2 are used to route the signal through a tunable filter to select a single sideband, which is sent through the device and to the detection electronics. The power P_{cal} in this sideband is directly measured on the PM at SW2, and switching to the BPD produces the photocurrent NPSD:

$$S_{II}(\omega) = S_{\mathrm{dark}} + \frac{G_{\mathrm{conv}}^2}{Z} S_{\mathrm{SN}}^2 \left(1 + \frac{\eta_{\mathrm{meas}} S_{\mathrm{cal}}(\omega)}{\hbar\omega_{\mathrm{o}}}\right), \tag{4.2}$$

where G_{conv} is the conversion gain of the BPD, Z is the RSA impedance, S_{dark} is the electronic NPSD of the detector, $S_{\mathrm{SN}} = \sqrt{2\hbar\omega_{\mathrm{o}}P_{\mathrm{LO}}}$ is the optical shot-noise NPSD arising from P_{LO} of LO

optical power at frequency ω_o, and S_{cal} is the NPSD of the signal, for which $\int_{-\infty}^{\infty} S_{cal}(\omega)\frac{d\omega}{2\pi} = P_{cal}$. The total noise floor $S_{noise} = \frac{G_{conv}^2}{Z} S_{SN}^2 + S_{dark}$ is measured with the signal beam blocked, and S_{dark} is measured independently with both signal and LO beams blocked. When referenced back to the PM, the calibration tone picks up losses incorporated into η_{meas}, extracted as

$$\eta_{meas} = \frac{\hbar\omega_o}{P_{cal}} \int_{-\infty}^{\infty} \frac{S_{II}(\omega) - S_{noise}}{S_{noise} - S_{dark}} \frac{d\omega}{2\pi} = 72\,\%. \tag{4.3}$$

This, combined with the measured device coupling efficiency, yields the overall measurement efficiency η used for calibrated mechanical thermometry as

$$\eta = \eta_{cpl}\eta_{23}\eta_{meas} = 20\,\%. \tag{4.4}$$

Mechanical spectroscopy is first performed at 4 K in order to calibrate the optomechanical transduction. The coupling rate g_0 is determined by observing the dependence of the mechanical linewidth on intracavity photon number n_c for both red ($\Delta = \omega_m$) and blue ($\Delta = -\omega_m$) laser-cavity detunings, as shown in Fig. 4.2a. Above a threshold value of $n_c > n_{thr} \approx 1.5$ (near the power where $\gamma_{OM} = -\gamma_i$), optical amplification and self-oscillation of the mechanical resonator occurs for blue detuning. Below this input power, the optomechanical damping γ_{OM} can be found from the difference between the red and blue detuned linewidths. A linear fit of the derived γ_{OM} versus n_c yields a coupling rate of $g_0/2\pi = 840$ kHz. Using this value, along with the previously calibrated optical detection efficiency, the mechanical mode occupancy versus n_c is determined from the area under the resonant part of the measured NPSD (Fig. 4.2b and c). At high n_c, the mechanical mode is seen to be cooled for red detunings, whereas at low n_c, $\langle n \rangle$ saturates to a constant value in good agreement with the prediction of thermalization at 4 K.

As the dilution refrigerator is lowered into the sub-Kelvin range, a very different dependence of measured occupancy and linewidth on optical probe power is observed. The trend with probe power of $\langle n \rangle$ does not follow the expected optomechanical response, which should show linear cooling at high power and saturation to the ambient thermal bath temperature at low power. Rather, a series of heating and cooling trends occurs. Furthermore, measurements at different dilution refrigerator base temperatures seem to only minorly affect $\langle n \rangle$, as shown by the converging of the data sets for $T_f = 10$ mK and 650 mK above $n_c = 1$. These effects suggest an optical heating mechanism which scales with probe power in some fashion. This explanation is verified by performing thermometry on resonance ($\Delta = 0$), which in the absence of an additional thermal effect should show constant $\langle n \rangle$ with probe power. Instead, $\langle n \rangle$ scales as $n_c^{1/4}$, as shown in the inset to Fig. 4.3a. The 1/4 power law is consistent with 3-dimensional thermal conductivity and linear optical absorption, where the thermal power $P_{heat} = An_c$ for some coefficient A. Then since thermal power is related to thermal conductivity G_{3D} as $P_{heat} = \int G_{3D} T^3 dT$, it follows that the temperature of the nanobeam (and

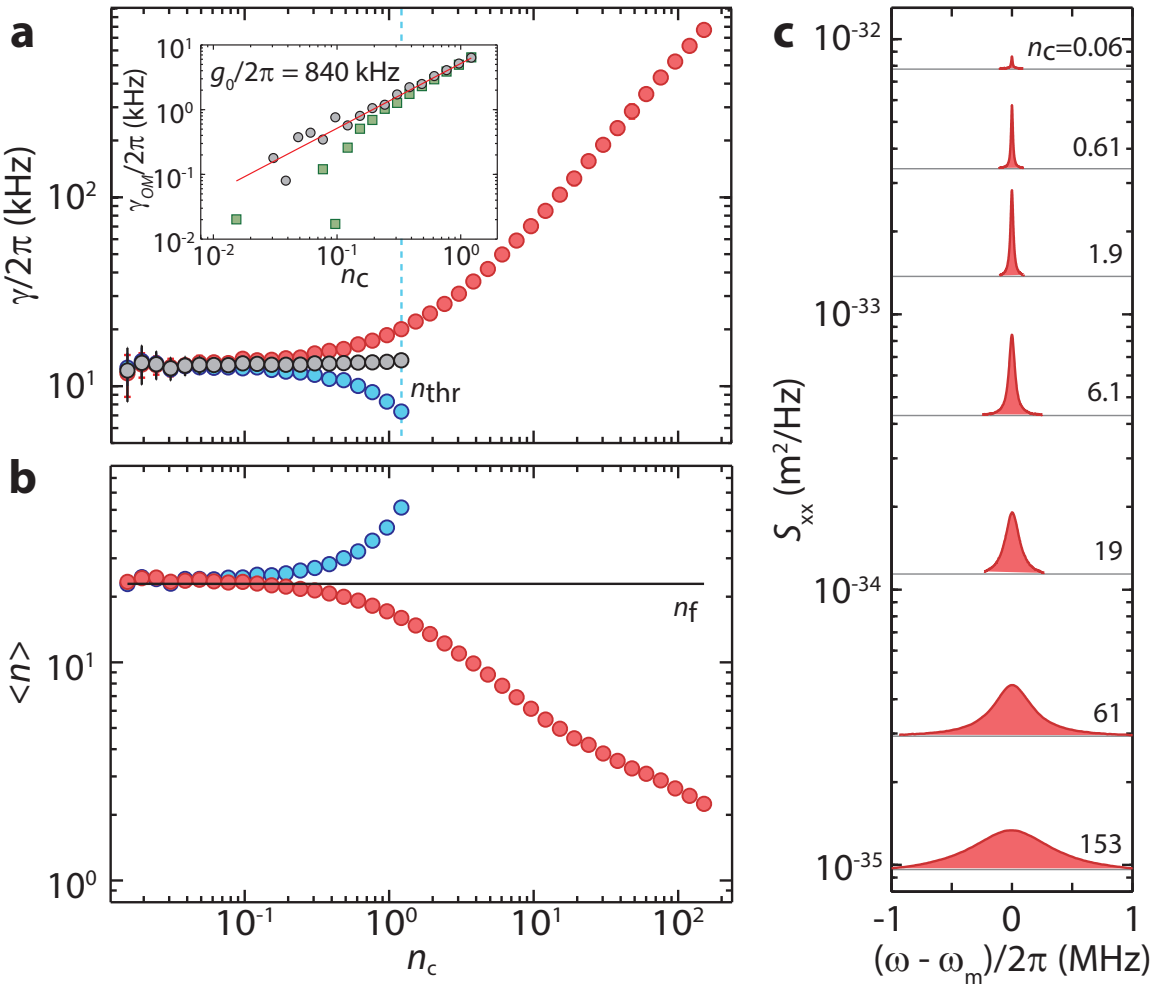

Figure 4.2: **4 K Spectroscopy. a** Measured mechanical linewidth γ for $\Delta = \omega_{\rm m}$ (red) and $\Delta = -\omega_{\rm m}$ (blue) at a dilution refrigerator temperature of $T_{\rm f} = 4$ K. The vertical blue dashed line indicates the threshold $n_{\rm c}$ beyond which the mechanical resonance self-oscillates for $\Delta = -\omega_{\rm m}$, resulting in a 40 dB increase in the mechanical signal level. Black circles indicate the values of $\gamma_{\rm i}$ obtained by taking the average of the detuned data. The inset shows $\gamma_{\rm OM}$ determined by subtracting $\gamma_{\rm i}$ from the red-detuned γ (circles) and from the cooperativity $C = 4G^2/\kappa$ using the calibrated $\langle n \rangle$ (squares). A linear fit (red line) yields $g_0/2\pi = 840$ kHz. **b** Calibrated mechanical mode occupancy $\langle n \rangle$ versus $n_{\rm c}$. Blue and red circles are measured with blue and red laser detunings, respectively. The mode occupancy $n_{\rm f}$ corresponding to $T_{\rm f} = 4$ K is indicated by the black solid line. **c** Series of red-detuned NPSD for a range of $n_{\rm c}$. Here the NPSD is plotted as $S_{xx} = x_{\rm ZPF}^2 S_{bb}$, where $x_{\rm ZPF} = 4.1$ fm is the zero-point amplitude of the mechanical breathing mode.

therefore $\langle n \rangle$) deviates from the dilution refrigerator bath temperature $T_{\rm bath}$ as $T = T_{\rm bath} + \frac{A}{G_{\rm 3D}} n_{\rm c}^{1/4}$.

Accounting for the dependencies of $\langle n \rangle$ and γ on $n_{\rm c}$ requires a model which includes the generation of a second thermal phonon bath, at an elevated temperature $T_{\rm p}$ and occupation $n_{\rm p}$. A plausible microscopic model (Fig. 4.4) of this hot phonon bath is the excitation of silicon-surface defect states [115, 116] through optical absorption. In its decay, the defect electron emits THz frequency phonons, which in turn either radiate quickly at rate $\gamma_{\rm THz}$ out of the phononic radiation shield,

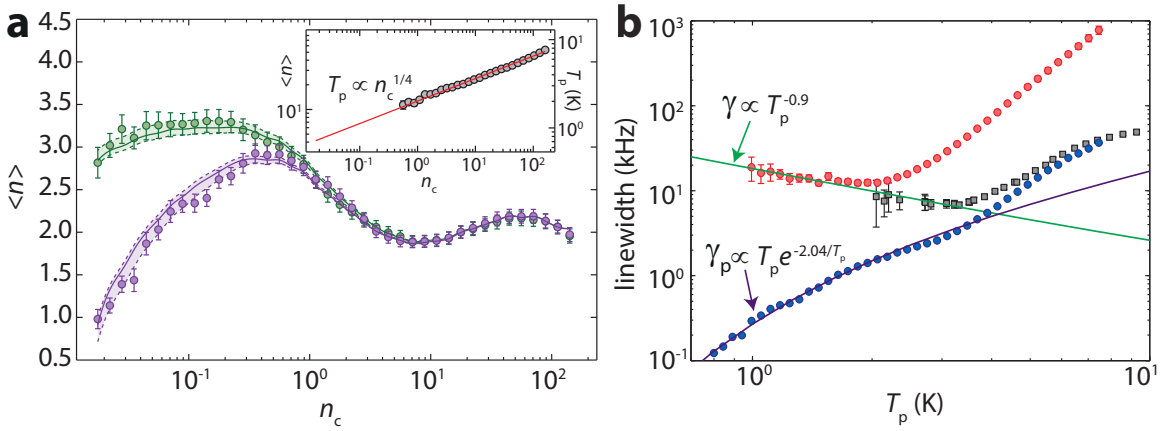

Figure 4.3: **Sub-Kelvin Occupation and Frequency Response. a** Average phonon occupation $\langle n \rangle$ measured with a red-detuned ($\Delta = \omega_m$) laser probe as a function of intracavity photon number n_c. Occupation measured with the dilution refrigerator operating at base temperatures of $T_f = 10$mK and 650 mK is shown in the purple and green points, respectively. The shaded regions enclosed by the dashed curves represent the variation in the fit of the optomechanical and thermal model for bare mechanical damping rate $\gamma_0 = 306 \pm 28$ Hz. The inset shows $\langle n \rangle$ measured with a resonant ($\Delta = 0$) probe as a function of intracavity photon number n_c. A power law fit of the observed optical heating trend shows that the hot phonon bath temperature $T_p \propto n_c^{1/4}$. In **b** the mechanical linewidth is plotted versus T_p, which is converted from n_c using the resonantly-determined power law scaling. The total linewidth γ measured at red-detuning (red circles) shows optomechanical damping at high power, but does not flatten to the intrinsic damping rate γ_i at low power. Rather, γ exhibits a $T_p^{-0.9}$ trend, suggesting frequency jitter caused by two-level tunneling states (TLS) [112–114]. The resonantly measured γ (gray squares) is limited at high power by the damping generated by the hot phonon bath γ_p, model values for which are plotted in purple circles.

or anharmonically decay into GHz frequency phonons which are long-lived in the device. These phonons then populate the mechanical mode at a rate γ_p proportionally to the optical power.

The mode occupation is therefore coupled to the distinct baths illustrated in the phenomenological model Fig. 4.4, based upon the following microscopic picture. The long-lived breathing mode is weakly coupled at rate γ_0 through the phononic crystal radiation shield to the exterior dilution refrigerator environment. Locally the mode is coupled via phonon-phonon scattering at rate γ_p to the optically generated high frequency phonons within the acoustic cavity. We parametrize the couping of the mechanical resonator to the separate thermal baths by decomposing the mechanical damping rate into $\gamma = \gamma_0 + \gamma_p + \gamma_{OM}$, where the dilution refrigerator bath (effective occupancy n_f) couples at rate γ_0, the optical-absorption-induced bath (temperature T_p and occupancy n_p at ω_m) couples at rate γ_p, and the intracavity laser field (effective zero-temperature bath for red-detuning) couples at rate γ_{OM}. The resulting average mechanical mode occupation is then given by $\langle n \rangle(n_c) = [\gamma_0 n_f + \gamma_p(T_p) n_p(T_p)]/[\gamma_0 + \gamma_p(T_p) + \gamma_{OM}(n_c)]$, where $T_p(n_c)$.

The utility of an optomechanical resonator for the preparation of nonclassical mechanical states relies on simultaneously achieving the thermal ground state and large coherent coupling between

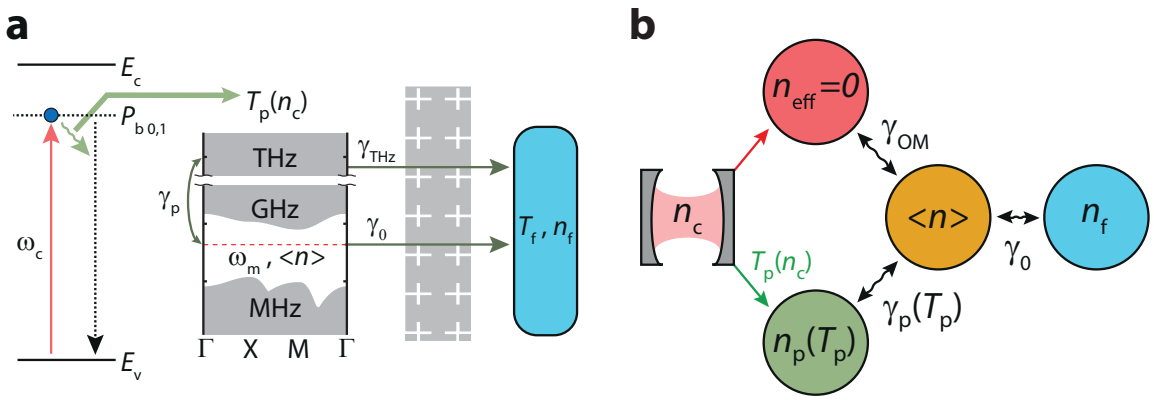

Figure 4.4: **Thermalization Model.** **a** Proposed microscopic model of the observed optical absorption heating. On the left, an example electronic band diagram shows the excitation of a valence band electron to a silicon defect state with near-infrared laser light in the cavity near frequency ω_c. The decay of this electron emits a THz frequency phonon, which itself decays according to the adjacent example mechanical band diagram. While THz phonons escape the device rapidly through the phononic crystal radiation shield at rate γ_{THz}, the portion of phonons that anharmonically decay into GHz frequency phonons are long-lived in the mechanical band-gap of the device. The population of the mechanical defect mode in this band diagram occurs at rate γ_{p}, which in turn depends on n_{c} through the optical population of the hot phonon bath. The cavity phonons are then weakly coupled to the dilution refrigerator environment, decaying through the radiation shield at rate γ_0. **b** Schematic representation of the phonon baths coupled to the mechanical resonator and the optical field.

photons and phonons. Specifically, the cooperativity parameter $C = \frac{\gamma_{\mathrm{OM}}}{\gamma_{\mathrm{i}}} > 1$ is required for high-fidelity quantum operations. The levels of optical absorption discovered in this initial milliKelvin domain experiment are such that intracavity photon numbers as low as $n_{\mathrm{c}} = 10^{-2}$ heat the device to $\langle n \rangle > 1$. Conversely, $C = 1$ occurs at $n_{\mathrm{c}} = 10^{-1}$.

Overcoming the steady-state absorption heating in the $C > 1$ regime requires either structural device development to improve thermal conductivity, or laser probing with a non-continuous-wave (CW) excitation. While some optomechanical crystal resonators have been demonstrated in two-dimensions [117], which would provide an order of magnitude increase to thermal dissipation, these structures feature lower g_0 than nanobeams and are more challenging to fabricate. Pulsing of a the laser probe beam to low duty-cycle, on the other hand, is simple to achieve with commercial optical modulators. Additionally, when paired with single-photon detection of the cavity output, pulsed-probe excitation allows for a variety of quantum state engineering experiments, such as heralding of phonon Fock states [25, 26] and entanglement of spatially-separated mechanical modes [19, 118].

4.2 Single-Photon Detection and Time-Domain Response

While pulsed-probe measurements can be analyzed in the frequency domain by gating the acquisition of a spectrum analyzer, it is significantly more computationally efficient to measure and count photon arrival times on a detector. Furthermore, with appropriate apparatus layouts, photon counting can be used to map the coherence of the acoustic field onto the cavity radiation, effectively phonon counting and allowing for more sophisticated correlation spectroscopy of the mechanics. This section will describe the phonon counting process, while the following chapter will detail second-order correlation measurements of mechanical states. An experiment combining phonon counting with pulsed-probe excitation at milliKelvin temperatures can be found in Ref. [27].

In the sideband-resolved regime, detuning the probe laser to $\Delta = \pm\omega_{\mathrm{m}}$ results in selective cavity enhancement to the Stokes or anti-Stokes motional sidebands. In terms of phonon dynamics, a blue-detuned probe photon at $\Delta = -\omega_{\mathrm{m}}$ emits a phonon into the mechanical resonance, while a red-detuned photon ($\Delta = -\omega_{\mathrm{m}}$) absorbs a phonon in order to resonate with the optical cavity. These two Raman scattering processes are illustratted in a Feynmann-like diagram superimposed on mode profiles in Fig. 4.5a,b.

For each detuning experiment, the cavity radiation consists of two frequency components: an unscattered probe reflection with the original Δ frequency, and a Raman-scattered component at $\Delta = 0$. While a frequency-domain measurement can separate these two components, operation in the time-domain requires spectral filtering of the Raman-scattered light from the probe reflection in order to extract the modulation signal. This is accomplished using two high-finesse Fabry-Perot filters (Micron Optics FFP-TF2) tuned to the cavity wavelength. Each filter has a bandwidth of 50 MHz, which is large enough to pass the mechanical signal having linewidth $\gamma_{\mathrm{i}} = 3\,\mathrm{MHz}$ (at room temperature) without causing spectral distortion. The free spectal ranges of the filters are 20 GHz, further allowing for high extinction of $A > 80\,\mathrm{dB}$ of the probe beam at $\Delta = \pm\omega_{\mathrm{m}} = \pm 2\pi \times 5.6\,\mathrm{GHz}$ relative to the peak transmission at $\Delta = 0$.

After filtering, the light is directed to a superconducting nanowire single photon detector (SPD) operating at 700 mK in a dilution refrigerator. The SPDs used in this work [119] were provided by the Superconducting Materials and Devices Group at the Jet Propulsion Laboratory (JPL). These SPDs are uniquely suited for this work in that they feature extremely high quantum efficiency (up to 93 %) and very low dark count rate ($< 10\,\mathrm{Hz}$), allowing for high sensitivity. Further details of the SPD operation in the phonon counting experiment can be found in Section 4.3.

As each detection of a cavity photon on the SPD was generated by a Raman scattering event in the optomechanical crystal, photon detection heralds either the creation or annihilation of a single phonon, effectively phonon counting. This can be rigorously shown by considering the linearized equations of motion (Eqns. 1.2, 1.3) in the Fourier domain (and rotating frame at a red-detuned

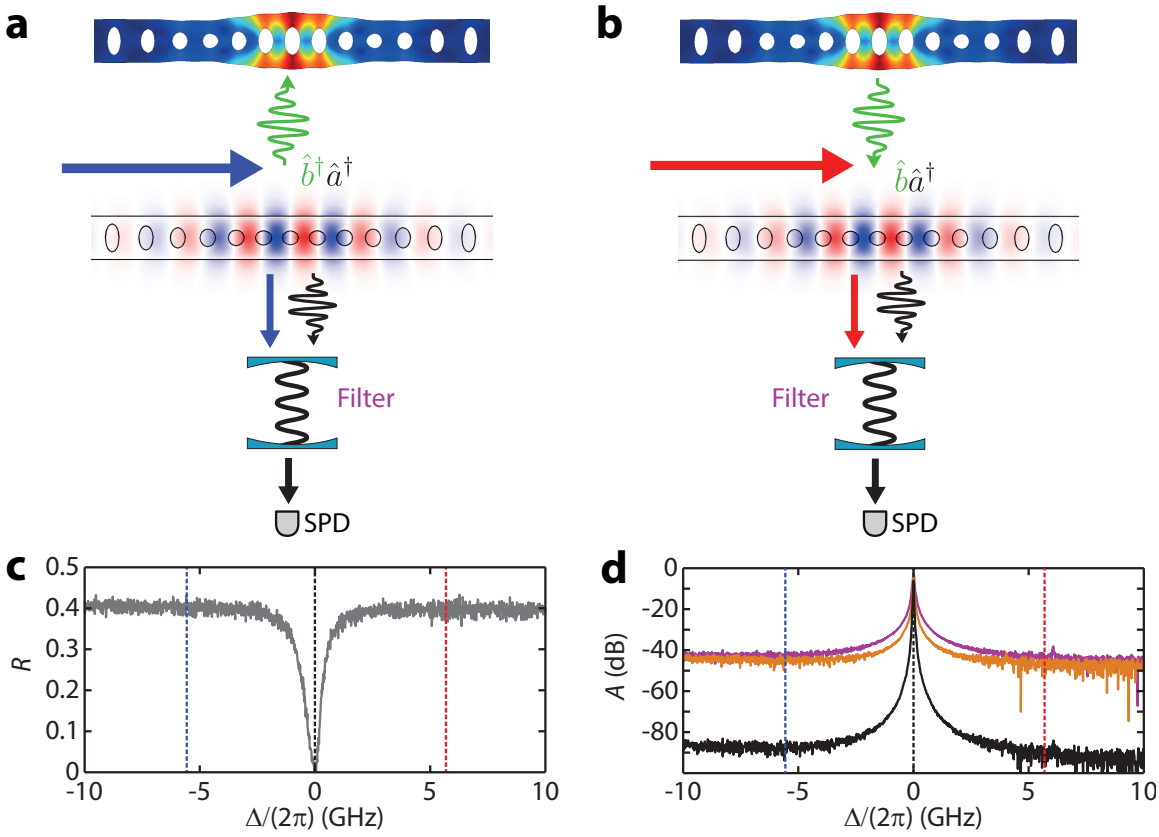

Figure 4.5: **Single Phonon Counting Diagram.** **a** Blue-detuned ($\Delta = -\omega_\mathrm{m}$) and **b** red-detuned ($\Delta = \omega_\mathrm{m}$) phonon counting diagram. FEM simulations of displacement (top) and optical electric field (below) illustrate the optomechanically enhanced phonon emission and absorption processes, with green arrows representing phonons, and blue, red, and black arrows representing light at detunings $\Delta = -\omega_\mathrm{m}$, $-\omega_\mathrm{m}$, and 0, respectively. These light frequencies are indicated in the dashed vertical lines on the device optical reflection spectrum **c** and the filter transmission spectra **d**. The filter attenuation factor A is shown for each of the two Fabry-Perot filters in the purple and orange curves, while the total attenuation of the filters in series is shown in the black curves.

pump frequency with $\Delta = \omega_\mathrm{m}$), in which the optical cavity output annihilation operator

$$\hat{a}_\mathrm{out}(\omega) = \left(1 - \frac{\kappa_\mathrm{e}}{i(\Delta-\omega)+\kappa/2}\right)\hat{a}_\mathrm{in}(\omega) - \frac{\sqrt{\kappa_\mathrm{e}\kappa_\mathrm{i}}}{i(\Delta-\omega)+\kappa/2}\hat{a}_\mathrm{i}(\omega) - i\frac{\sqrt{\kappa_\mathrm{e}n_\mathrm{c}}g_0}{i(\Delta-\omega)+\kappa/2}\hat{b}(\omega), \qquad (4.5)$$

where $\hat{a}_\mathrm{in}(\omega) = \alpha\delta(\omega) + \hat{a}_\mathrm{vac}(\omega)$ for a steady-state coherent optical field component α and pump vacuum noise $\hat{a}_\mathrm{vac}(\omega)$. Additional vacuum noise admitted via intrinsic loss channels is included via $\hat{a}_\mathrm{i}(\omega)$. Note that for a blue-detuned pump ($\Delta = -\omega_\mathrm{m}$), the acoustic annihilation operator $\hat{b}(\omega)$ is replaced in Eqn. 4.5 by $\hat{b}^\dagger(\omega)$. In general there will be a small correction to $\hat{a}$ due to the counter-rotating terms in the interaction ($\hat{b}^\dagger$ or $\hat{b}$ for $\Delta = \pm\omega_\mathrm{m}$, respectively). However, this term will be reduced by the sideband resolution ratio $\kappa/2\omega_\mathrm{m}$, and thus its contribution to any photon counting measurements will scale as $(\kappa/2\omega_\mathrm{m})^2$. As this quantity is less than 1 % in the devices under study

here, these terms can be safely neglected.

As $\hat{b}(\omega)$ is sharply peaked around $\omega = \omega_{\mathrm{m}}$, the strong optical pump at $\omega = 0$ is filtered by the attenuation factor A as previously described. The additional optical noise, assumed to be white Gaussian noise, cannot be filtered out in this way. However, in the case that the optical noise is pure vacuum noise it will not contribute to any photon counting events. Thus, for the purposes of photon counting the output optical field can be written post-filtering as

$$\hat{a}_{\mathrm{out}}(t) \approx \frac{2\sqrt{\kappa_{\mathrm{e}} n_{\mathrm{c}}} g_0}{\kappa} \hat{b}(t) = \sqrt{\frac{\kappa_{\mathrm{e}}}{\kappa}} \sqrt{|\gamma_{\mathrm{OM}}|} \hat{b}(t), \tag{4.6}$$

which shows explicitly that in this linearized regime, photon counting is equivalent to phonon counting.

Detection of light at other frequencies is treated as noise, and limits the sensitivity of the phonon counting scheme. A useful parameterization of the sensitivity is the amount of noise proportional to the signal generated by a single phonon in the optomechanical crystal. This noise equivalent phonon number n_{NEP} can also be interpreted as the mechanical occupation that would produce an SNR of 1. For phonon counting of mechanics in the quantum regime, it is thus desirable to achieve $n_{\mathrm{NEP}} \ll 1$.

To obtain n_{NEP} we measure independently the sideband count rate $\langle n \rangle \Gamma_{\mathrm{SB}}$ with the probe detuned to $\Delta = \pm\omega_{\mathrm{m}}$, and the noise count rate Γ_{noise} with $\omega_{\mathrm{m}} < |\Delta| < 2\omega_{\mathrm{m}}$. By detuning the probe far from a sideband frequency harmonic, the Raman scattered signal is strongly suppressed by the optical cavity and the remaining filter transmission corresponds mostly to the unscattered probe beam. The filter cavity is also tuned by the same offset to replicate the attenuation factor A realized during phonon counting. The total noise rate is a combination of the SPD dark count rate and the probe beam photon flux rate $\Gamma_{\mathrm{noise}} = \Gamma_{\mathrm{dark}} + A\eta\dot{N}_{\mathrm{probe}}$, where η is the total setup transmission efficiency from the cavity, including the SPD quantum efficiency of 70%. The deep sideband resolution of the device under test, where $\kappa/2\pi = 817\,\mathrm{MHz} \ll \omega_{\mathrm{m}}/2\pi = 5.6\,\mathrm{GHz}$, allows the probe photon flux rate to be approximated as $\dot{N} = n_{\mathrm{c}}(\Delta^2 + \kappa/4)/\kappa_{\mathrm{e}} \approx n_{\mathrm{c}}\omega_{\mathrm{m}}^2/\kappa_{\mathrm{e}}$. Since Raman-scattered photons are generated at a rate of γ_{OM}, the sideband count rate at the SPD is simply $\Gamma_{\mathrm{SB}} = \frac{\kappa_{\mathrm{e}}}{\kappa}\eta|\gamma_{\mathrm{OM}}|$. The ratio $n_{\mathrm{NEP}} = \Gamma_{\mathrm{noise}}/\Gamma_{\mathrm{SB}}$ is then given by

$$n_{\mathrm{NEP}} = \frac{\kappa^2 \Gamma_{\mathrm{dark}}}{4\eta\kappa_{\mathrm{e}} n_{\mathrm{c}} g_0^2} + A\left(\frac{\kappa\omega_{\mathrm{m}}}{2\kappa_{\mathrm{e}} g_0}\right)^2. \tag{4.7}$$

The presence of g_0 in the denominator of both terms of Eqn. 4.7 makes clear the benefits of the cavity enhanced optomechanical coupling to sensitivity, in contrast with the large optical power requirements of photon correlation spectroscopy of particulate motion [120] and stimulated Brillouin scattering of bulk acoustic modes in optical fibers [121–123]. At low power, the first term of Eqn. 4.7 set by the SPD dark count rate limits the sensitivity, while at high power the level of bleed through

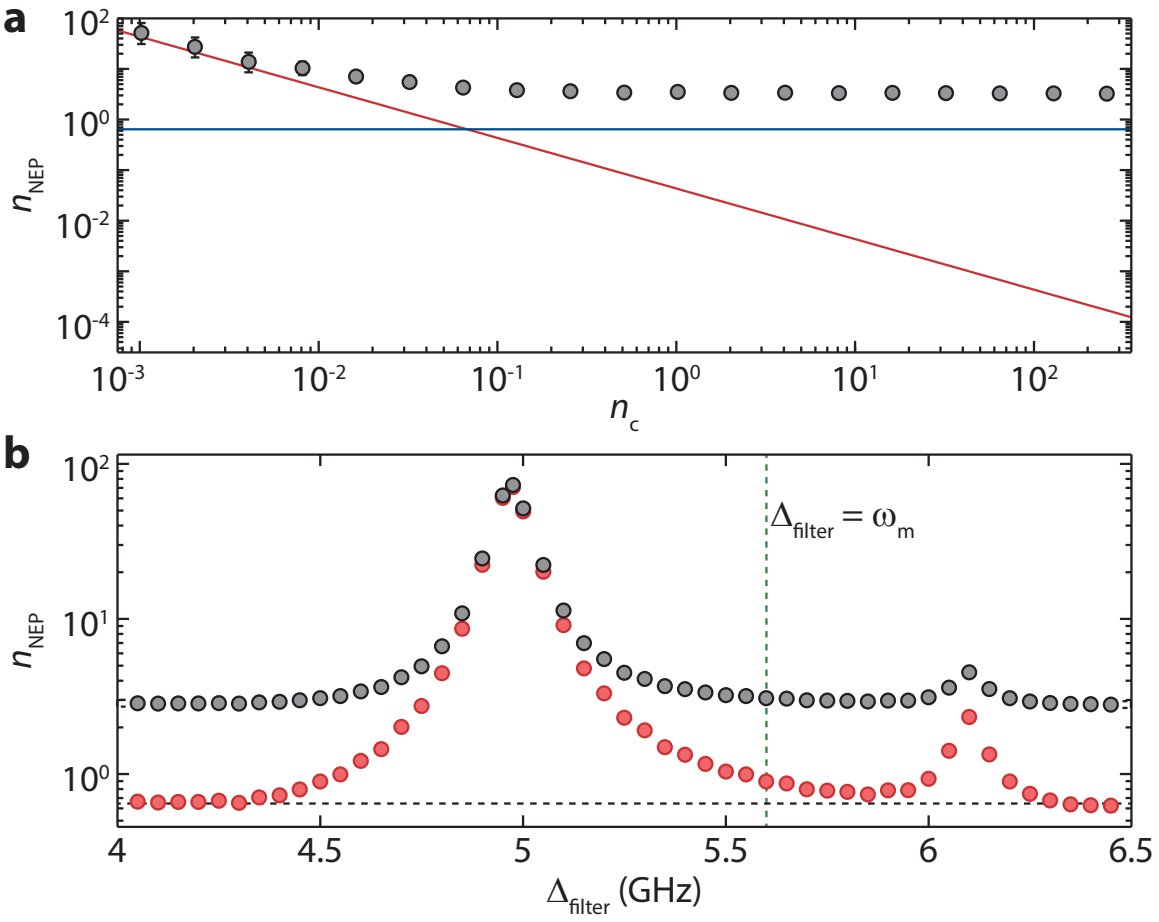

Figure 4.6: **Phonon Counting Sensitivity.** **a** Noise-equivalent phonon number n_{NEP}, measured with two sideband filters, as a function of n_{c} is plotted in gray circles, while solid lines represent calculations of the dark count contribution term (red) and probe transmission through the filters (blue). **b** n_{NEP} measured at $n_{\mathrm{c}} = 65$ as the frequency of the filter transmission is varied with respect to the laser line. Gray and red circles show the sensitivity obtained before and after the addition of a C-band bandpass filter, respectively. The dashed horizontal line represents the expected sensitivity for $n_{\mathrm{c}} = 65$ in the absence of laser noise.

of the probe beam limits n_{NEP} to a minimum value. Fig. 4.7a shows the measured sensitivity with the calculated contributions from both noise contributions. While the low power end, limited by detector dark count, follows the expected trend, the high power n_{NEP} levels off to 3.5 phonons, well above the value of 0.65 phonons predicted by calibration of cavity parameters and the filter extinction A (Fig. 4.5d).

An investigation of the detuning dependence of the filter transmission (Fig. 4.7b) reveals that the high-power discrepancy in n_{NEP} lies in laser noise. Phase noise in commercial external cavity diode lasers, such as the New Focus TLB-6700 Velocity laser used here, is known to vary both in magnitude and spectral distribution [46]. By adjusting the filter frequency relative to the laser line frequency, the light generated by phase noise can be isolated and observed to feature two prominent

peaks near 5 GHz and 6.1 GHz. In between these peaks at $\Delta = \omega_m$, another source of noise adds a flat background well above the dark count rate of the SPD. Since this background does not depend on Δ, it must correspond to light with wavelength far from spectral selectivity of the filters, such as broadband spontaneous emission of the laser source. Further filtering using a band-pass filter with bandwidth of 10 nm in wavelength successfully removes this background, and brings n_{NEP} near the expected sensitivity level. Further detail on spectral filtering and SPD dark count rates can be found in Appendix 4.3.

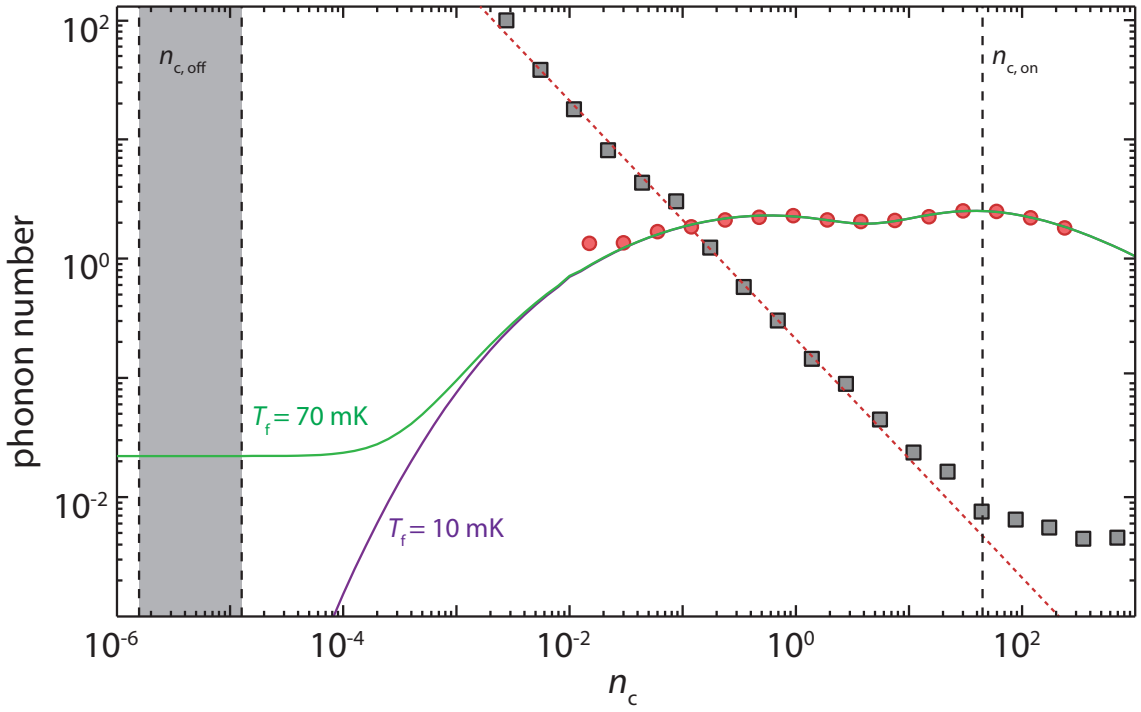

Figure 4.7: **Sensitivity to Pulsed Laser Probe.** Noise equivalent phonon number n_{NEP} (gray squares) and phonon occupancy $\langle n \rangle$ (red circles) measured with a red-detuned ($\Delta = \omega_m$) continuous-wave probe versus intracavity photon number n_c. The dotted red line shows the calculated SPD dark-count contribution to n_{NEP}. Solid green and purple lines represent a thermal model fit to $\langle n \rangle$, extrapolated to low n_c for dilution refrigerator thermalization temperatures of $T_f = 70$ mK and 10 mK, respectively. Pulse state photon numbers allowing for sensitive motional ground state detection are indicated by the regions enclosed by $n_{c,off}$ and $n_{c,on}$.

The addition of a third series filter increases $A > 120$ dB, as shown in Fig. 4.7. At this level of extinction, the high power-limited sensitivity allows for detection of mechanics deep in the motional ground state with $n_{NEP} = 5 \times 10^{-3}$. Superimposing the sensitivity with the CW phonon occupation shows the relevant operation of the phonon counter for quantum state detection and preparation. While the phonon counter requires $n_c > 10$ to reach excellent sensitivity, an extrapolation of the thermal model given by Fig. 4.4 gives a range of $n_c < 10^{-3}$ for the device to thermalize deep in the ground state. Pulsing of the laser probe between these two photon numbers, with a duty cycle

heavily favoring an off-state photon number $n_{\mathrm{c,off}} < 10^{-4}$, allows for quick, sensitive measurement of the mechanics in their ground state at an on-state photon number $n_{\mathrm{c,on}} = 45$ [27].

4.3 Characterization of Noise in Superconducting Nanowire Single Photon Detectors

4.3.1 Theory of Operation

Single photon detectors are crucial tools for a host of scientific and engineering applications, ranging from sensing of extremely low levels of light in biological and chemical compounds [124–126] to quantum information processing and communication protocols [127–129]. Devices such as photomultipler tubes and single-photon avalanche detectors have long been mainstays of single photon detection at visible light wavelengths, but suffer from poor quantum efficiency and high dark count noise in the near-infrared spectrum [129]. In particular, material defects in III-V compound semiconductors with sufficiently small bandgap to absorb 1550nm light (such as InGaAs) cause electron tunneling detections, raising the DCR to > 10 kHz, orders of magnitude larger than that of higher material quality visible absorbers such as silicon. While sophisticated detector structures and gating electronics can reduce DCR to ~ 100 Hz, the quantum efficiency is still limited to $< 20\,\%$ [130].

Many of the performance challenges in III-V semiconducting photodetectors are being met by an emerging class of devices based on superconducting thin films. Biasing of a superconducting film slightly below its critical transition current density j_{c} (and temperature well below the critical temperature T_{c}) creates a small but stable optical absorption energy gap [131]. The absorption of a photon, with sufficient energy to break apart enough Cooper electron pairs to create a local current density higher than j_{c}, then creates a region of normal conductivity in the film. Transition-edge sensors (TESs) operate based on this principle, with a superconducting film of materials such as tungsten (W) connected to a superconducting quantum interference device (SQUID), which measures the temperature change upon absorption of a photon [132]. TESs achieve both high quantum efficiency ($50 - 90\,\%$) and low dark count rate ($< 10\,\%$) Hz, but suffer from poor timing properties such as large jitter time and reset time [129].

Beyond TESs, recent advances in the fabrication of superconducing thin films have enabled superconducting SPDs of even higher quality. In particular, patterning of the film into a narrow wire, with rectangular cross-section $5 \times 20 - 50$ nm, results in the creation of a completely resistive wire region from an initial photon absorption event [131]. This process is depicted in Fig. 4.8, where an initial photon absorption in a superconducting nanowire SPD (SNSPD) takes a local section of the wire into the normal state. As this section undergoes Joule heating, the "hot spot" expands across the wire width as the surrounding current flux is increased above j_{c} and hot electrons travel through

the wire. Eventually the resistive state encompasses the full wire cross section, and a voltage gradient is created. Before the hot spot re-thermalizes, the photon absorption creates a current spike which can be measured with a resistive load across the wire. SNSPDs fabricated from such superconducting materials as NbN and NbTiN feature simultaneously low dark count rate and excellent timing properties, although initial difficulties in optical coupling and in fabricating uniformly narrow wires limited achievable system detection efficiencies to $< 40\,\%$ [133] grain boundary defects in these polycrystalline films also negatively impacted the yield of high quality devices. Sustained development of optical coupling and deposition methods has improved yields to near unity in multi-pixel arrays [134] as well as boosted detection efficiencies to between 70 % and 80 % [135, 136].

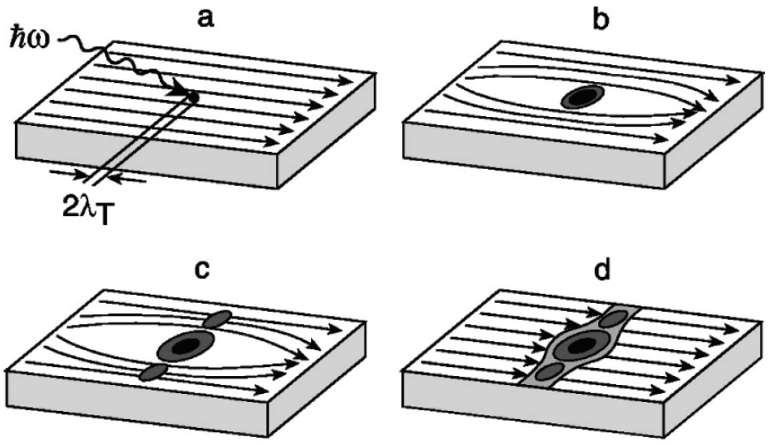

Figure 4.8: **SNSPD Hot Spot Formation.** Reprinted with permission from [131]. Copyright 2001, AIP Publishing LLC. Illustration of the hot spot formation in an SNSPD. **a** Absorption of a photon in the current-biased wire (charge flow represented by arrows). **b** Breaking of Cooper pairs forms a local resistive region, which rises in temperature due to Joule heating. **c** As surrounding areas of the wire are heated by the hot spot and current flowing around the hot spot is further confined, the critical current density is exceeded in transverse directions of the wire, and the hot spot expands. **d** Eventually the hot spot spans the wire cross section, and the resistive section impedes current flow.

The Optoelectronic Manufacturing Group at the National Institute of Standards and Technology (NIST) has recently turned to amorphous tungsten silicide (WSi) as a promising alternative to niobium-based films for SNSPDs [137]. The homogeneous disordering of WSi is thought to increase the robustness to structural defects as well as allow for integration with reflective substrates for cavity-enhanced absorption. Due to its lower critical temperature, WSi wires as wide as 150 nm support hot spot formation for near-infrared light, with an extended range of bias current for which the quantum efficiency is saturated (albeit at the cost of lower operation temperatures). In collaboration with JPL, these detectors have been embedded in a reflective optical film stack and precision-aligned to an optical fiber ferrule, resulting in system detection efficiency of 93 % and $DCR < 1$ kHz [119].

4.3.2 SPD Setup for Phonon Counting

Two WSi SNSPD devices [119] were supplied by Francesco Marsili and Matthew Shaw of JPL to the Painter group for integration in optomechanical phonon counting experiments. They were installed on the still-stage plate of a BlueFors BF-LD dilution unit, a photograph of which is shown in Fig. 4.9. The two SNSPD assemblies (each consisting of a detector chip wire bonded to an SMP breakout receptacle and aligned to a zirconia sleeve for fiber coupling) are mounted on copper blocks for thermalization to the still temperature of ~ 700 mK. As the critical temperature of WSi SNSPDs is 2.5 K, still temperatures of < 1 K are required for biasing the detectors with a current that is below the temperature-dependent critical current, yet large enough to saturate the quantum efficiency.

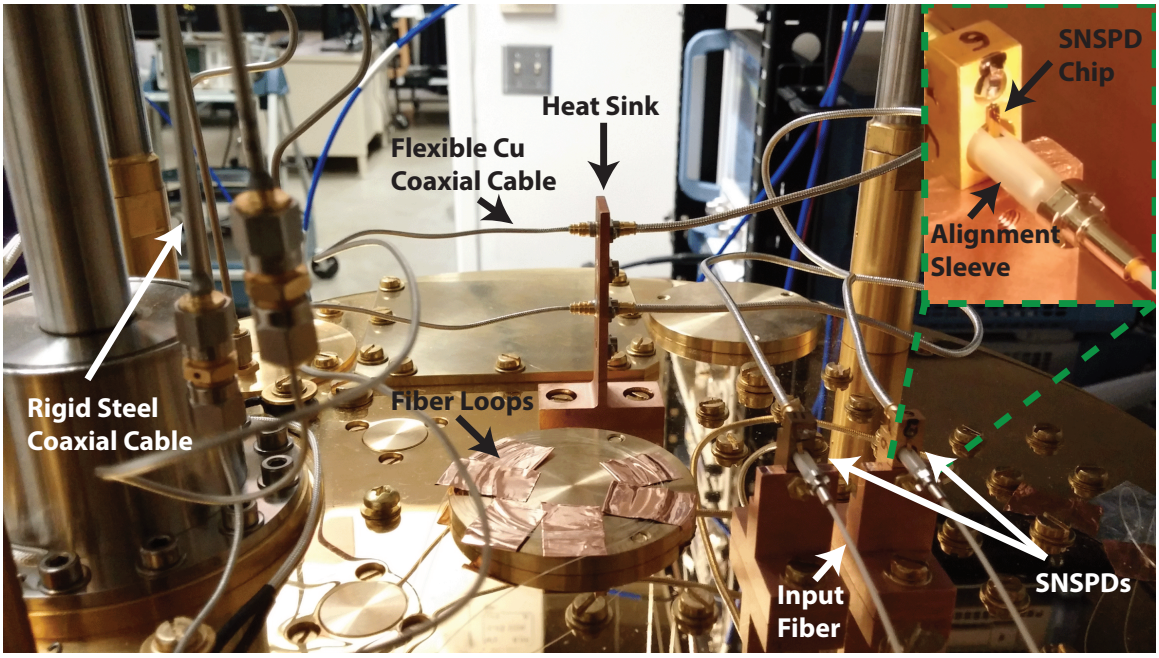

Figure 4.9: **Optical and Electrical SPD Layout.** Photograph of the BlueFors still plate, with SNSPDs, optical fiber inputs, coaxial cable inputs, fiber spools, and electrical heat sink indicated. The inset shows a detailed view photograph of an SNSPD, with the SNSPD chip aligned to an input fiber flat-polished ferrule via a zirconia ferrule.

The SMP electrical outputs of the SNSPDs are connected to flexible copper coaxial cables (Pasternack PE36164) which connect to SMA-connectorized rigid stainless steel coaxial cables (Micro-Coax UT-085-SS) running through hermetically sealed feed-throughs (Huber-Suhner 34-SMA-50-0-3/111-N) at each cryogenic stage to a custom cryogenic amplifier board provided by JPL. The amplifier board is mounted to the 50 K cryogenic stage, and splits the SPD input cable into a DC bias circuit and an RF readout circuit. The DC leads consist of 34 AWG twisted pair wires, and are soldered to two series low-pass filters (Mini Circuits SLP-1.9+ and VLFX-80) which couple through a vacuum feed-through to room-temperature. BNC connectors were used at room temperature to connect the

DC lines to a custom DC current source consisting of a voltage-divided battery pack (2 commercial 1.5 V "AA" batteries in series with 100 kΩ – 10 MΩ potentiometer-tunable series resistance) sourcing 0.5 – 30 μA. The RF circuit is amplified at 50 K by 28 dB (Sirenza SGL-0622Z) before running through semi-rigid beryllium/stainless-steel coaxial cable to the room-temperature vacuum feedthrough. At room temperature the signal is amplified by another 40 dB (Mini Circuits ZKL-1R5+) before connecting to the Picoharp 300 TCSPC module. A time trace of a voltage pulse after amplification (acquired on a high-speed oscilloscope) is shown in Fig. 4.10. When the current bias is positive, a positive-voltage pulse is generated as in the figure. Since the Picoharp 300 triggers on negative voltage falling edges, the signal is inverted with a Picoquant SI100 passive inverter module prior to input to the TCSPC module. When the current bias is flowed the other direction in the DC circuit to produce a negative current (as in much of the following description), the negative-voltage pulse does not need to be inverted and the SI100 is omitted.

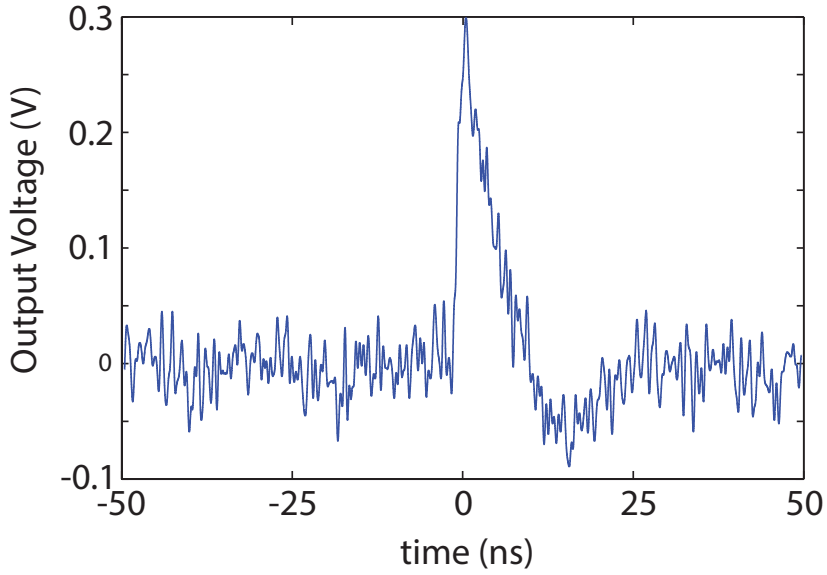

Figure 4.10: **Output Voltage Pulse.** Oscilloscope time trace of a voltage pulse from an SNSPD photon detection, operating with a positive current bias and after cryogenic and room-temperature amplification.

While the cryogenic feed-throughs establish an electrical and thermal connection between the cable outer conductors to the dilution refrigerator ground, the center conductor must be separately thermalized to avoid room-temperature head loads on the SNSPDs. This is achieved with hermetic feed-throughs (Fairview Microwave SC5292 and SC5316) soldered to a heat sink copper mount. These feed-throughs use a glass bead as a dielectric separation between inner and outer conductors, thus allowing thermal, but not electrical, contact between the center conductor and the still plate.

Optical fiber coupling to the detectors are made with a flat-polished ferrule connector. The ferrule is slid into a zirconia alignment sleeve until it makes light physical contact with the detector

chip. In this position the fiber is optimally aligned to the SNSPD for high-efficiency illumination of the detector. At low temperature, the thermal contraction of the alignment sleeve maintains optimal alignment [138]. The other end of the connectorized fiber is spliced to a dedicated fridge fiber, which runs from the still through each cryogenic stage to a room-temperature fiber feed-through consisting of a $\sim 250\,\mu$m diameter hole drilled through a teflon ferrule. The teflon ferrule is compressed in a Swage-lok tube fitting to maintain a vacuum seal.

4.3.3 Dark Count Reduction

Initial calibration of the SNSPDs at JPL showed system detection efficiencies (with respect to optical power coupled into the input fiber) of $\sim 80\,\%$, while the dark count rate was repeatedly shown to vary between $1 - 10$ Hz for current biases with saturated quantum efficiency. However, this dark count rate was measured in conditions with either the input fiber capped at room temperature to block stray light from illuminating the SPD, or with room lights switched off. As the phonon counting experiments of this work required the SPDs to be coupled to a larger optical setup, further calibration of the dark count rate was required after installation in the Painter group BlueFors dilution refrigerator and integration to the phonon counting apparatus (Fig. 5.3).

After installation of the SNSPDs, the system detection efficiency was found to be $\sim 70\,\%$, while $DCR = 300 - 500$ Hz for current biases achieving that efficiency (Fig. 4.11). The reduction in detection efficiency is believed to stem from temperature-depended bending loss in the cryogenic optical fiber paths, as has been observed in previous experiments [111]. While the reduced system detection efficiency is still high enough to enable high phonon counting sensitivity (low n_{NEP} as defined by Eqn. 4.7), the dark count rate would require significantly large probe power to reach $n_{\mathrm{NEP}} < 1$, making deep ground state occupancy difficult to detect. As electrical noise was ruled out by isolating the SPD circuitry from other instrumentation, the deviation in measured DCR from the intrinsic DCR of $1 - 10$ Hz is attributable to photon counts caused by background light illuminating the SPDs.

4.3.3.1 Mid-IR Optical Attenuation

The optical fiber paths connecting the SPDs to the room temperature setup carry not only the ~ 1550 nm, near-infrared light used in the experiment, but also longer wavelengths of light produced by thermal black-body radiation at 300 K. The cyan and blue data points of Fig. 4.11 show the SPD count rate when the input fiber is connected to the room temperature setup, with the laboratory fluorescent ligths switched on and off, respectively. While a combination of visible and infrared light leaking into the input fiber before it enters the dilution refrigerator raises the background count rate to $> 10^4$ Hz, switching off the visible portion emitted by the room lights only reduces the count rate to $300 - 500$ Hz. The dependence of count rate on bias current I_{bias}also follows a similar turn

on shape as the illuminated case, indicating that the counts are indeed due to detection of light at other wavelengths.

One way to attenuate the amount of light with wavelength > 1625 nm, of which black-body radiation would primarily be composed, is to take advantage of wavelength-dependent macrobending loss in optical fiber [92]. As the Corning SMF-28e fiber used in this work is optimized for transmission at 1550 nm, it can be bent with radius of 10 mm while only attenuating light at that wavelength by 0.5 dB. Longer wavelength light, on the other hand, incurs greater loss (1.5 dB at 1625 nm), as the angle of reflection of the propagating mode between the fiber-core/cladding interface falls below the critical angle of total internal reflection, and a portion of the mode transmits into the cladding at each reflection event. The red and magenta points of Fig. 4.11 show that the longer wavelength light in the mid-infrared spectrum is reduced by almost an order of magnitude by 5, 1.5 inch diameter fiber loops just prior to the SPD (indicated in Fig. 4.9), while the near-IR and visible illumination incurs little attenuation.

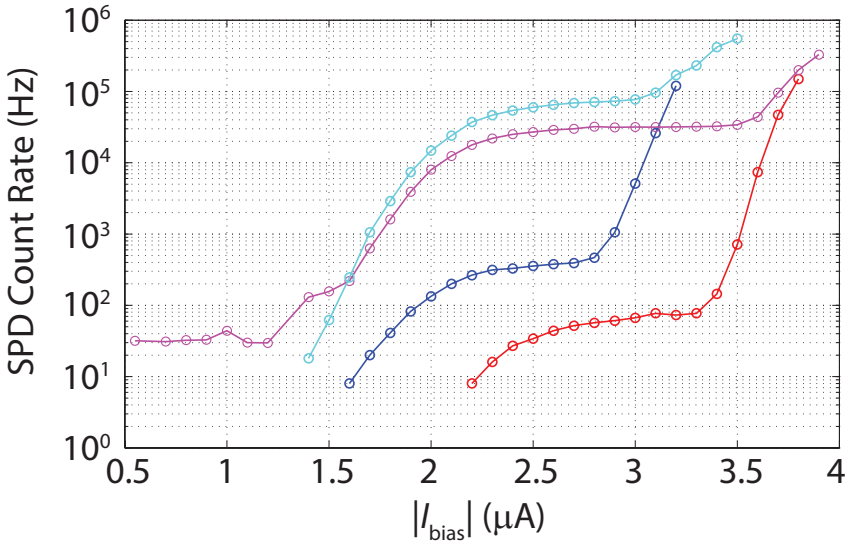

Figure 4.11: **SPD Dark Counts with Fiber Loops.** Comparison of detector performance with no looping of the input optical fiber (blue, cyan) and 5, 1.5 inch diameter fiber loops (red, magenta). Even with no laser optical input (attenuators set to blocked state) room light coupling into fiber unions in the laboratory raises the count rate to $> 10^4$ Hz (cyan, magenta) in the response region of the current bias curve, while room lights were kept off for the blue and red points.

4.3.3.2 Stray Light Reduction

Although the fiber loops greatly attenuate the impact of mid-IR illumination, the remaining $DCR = 70$ Hz still exceeds the internal SPD dark count rate and has the dependence on I_{bias}, indicating photodetection events. The impact of stray light within the dilution refrigerator was investigated by enclosing the SPDs in a radiation shield, as shown in Fig. 4.12. The shield blocks light emanating

either from laboratory light leaking into the dilution unit or from black-body radiation of different temperature stages within the fridge from propagating to the SPD, and results in lowering the DCR to $30 - 40$ Hz (Fig. 4.13).

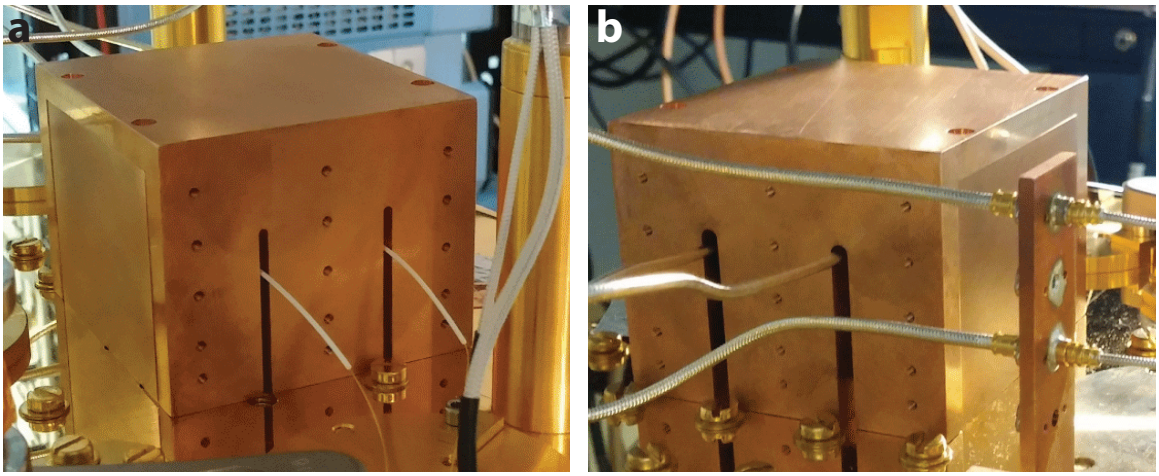

Figure 4.12: **Stray Light Shield.** Photograph of the radiation shield enclosure with **a** input fiber and **b** coaxial cable access to the SPDs.

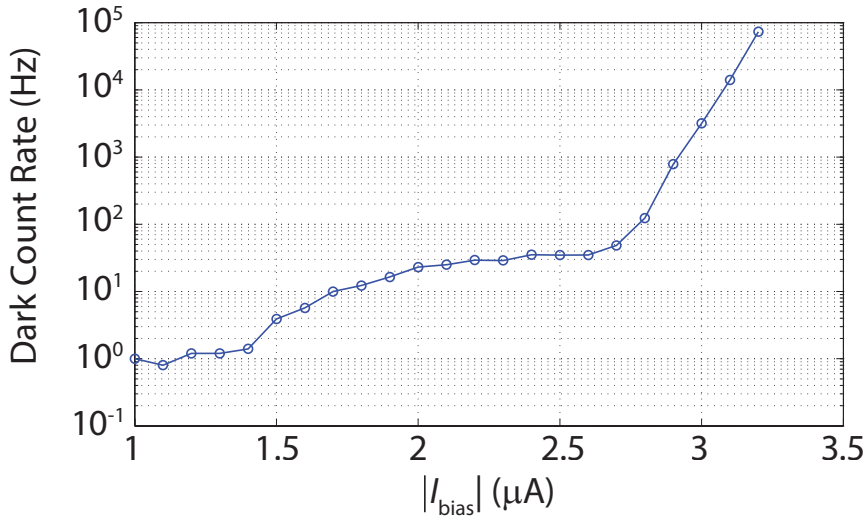

Figure 4.13: **SPD Dark Counts with Stray Light Shield.** Dark count rate measured with room lights off and with SPD shielding enclosure.

Following the installation of the radiation shield, further filtering of mid-IR light was attempted by transmitting the input light through a coarse wavelength division multiplexer (CWDM, JDS Uniphase FWS-A00220002) mounted to the still plate of the dilution refrigerator. The CWDM, with a transmission wavelength pass band of $1528 - 1610$ nm, connects to the input fiber between

the fiber loops and the SPD in order to filter any remaining long-wavelength light. Interestingly, while the DCR did not decrease appreciably from the result obtained with the radiation shield, unplugging and ferrule-capping the room-temperature optical fiber from the experimental phonon counting setup decreased the DCR to $\sim 1-2$ Hz. Recovering this intrinsic SPD dark count rate indicated that light sources from within the dilution refrigerator and from room-temperature blackbody radiation had been eliminated, and that the remaining excess count rate stemmed from an excess light source within the phonon counting apparatus.

4.3.3.3 Near-IR Optical Attenuation

After accounting for visible, mid-IR, and stray light within the dilution refrigerator, the remaining near-IR portion of the excess background count rates was investigated. A combination of two Micron Optics narrow-band Fabry-Perot filters and a 10 nm bandwidth band-pass filter on the input fiber prior to the dilution refrigerator successfully reduce the dark count rate to < 10 Hz, as shown in Fig. 4.14. The band-pass filter, not originally used in the optical setup shown in Fig. 5.3, was found to be necessary to reduce light at wavelengths outside of the ~ 50 nm range of the Fabry-Perot filters. Combining the two Fabry-Perot filters then results in a wavelength bandwidth < 50 MHz of transmitted input light to the SPDs. As discussed in the previous section, a combination of laser phase noise and a broad spontaneous emission spectrum are believed to be the source of the excess near-IR light, thus requiring the narrow-band and wide-band filtering described here.

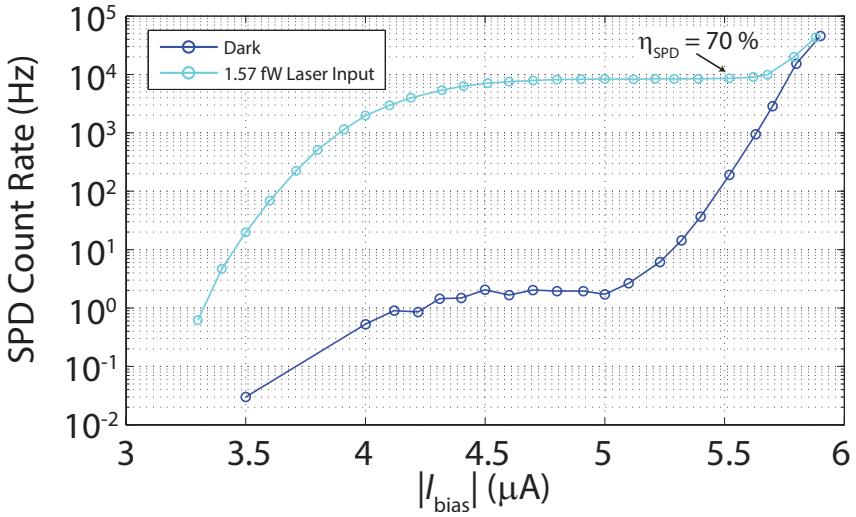

Figure 4.14: **SPD Dark Counts with Filtered Input.** Blue points show the SPD dark count rate with shielding, room lights off, and optical filtering of the input channel with two high-finesse Fabry-Perot filters and one 10 nm bandwidth band-pass filter. The cyan points were taken with the attenuator set to produce 1.57 fW of laser power incident on the SPD. The efficiency curve levels off to 70 % before reaching the critical current, while dark counts only reach ~ 2 Hz.

Chapter 5

Phonon Correlation of a Self-Oscillating Mechanical Resonator

This chapter describes the use of the phonon counting technique in characterizing the coherence of a nanomechanical resonator. As sideband photons are produced by Raman scattering from an acoustic field with a certain time evolution, it follows that the associated photodetections display the same time evolution. Therefore, extending the phonon counting technique of Chapter 4 to two single photon detectors and performing intensity interferometry on sideband light, the second order degree of coherence of the acoustic field can be measured. The second order coherence displays qualitative differences between distinct physical states, and here is used to observe the evolution of an optomechanical crystal as the mechanical resonator undergoes a parametric instability formally equivalent to that of a laser threshold condition.

5.1 Intensity Interferometry

The case of a radiant optical field incident upon two spatially-separated photodetectors, with individual photodetection probabilities P_1 and P_2, is an interesting one [139]. Absent some field-interference generating element such as a beam splitter, one might naïvely assume that the lack of phase information would preclude determining the time evolution, and therefore coherence, of the radiation source. However, when one considers the joint probability of photodetection $P(r_1, t_1; r_2, t_2)$ at times t_1, t_2 and position r_1, r_2 for detectors 1 and 2, respectively, $P(r_1, t_1; r_2, t_2) \neq P_1 P_2$, since it cannot be assumed that the average incident intensity at each space-time point are independent. Rather, the incident intensities are correlated by their common radiation source, which can be measured through the correlation of the two photocurrents. This effect was first observed for visible light in landmark experiments by Hanbury Brown and Twiss [140, 141], and has since proved to be an invaluable tool for determining the physical nature of light sources.

5.1.1 Historical Background

Although the Hanbury-Brown-Twiss experiment, in conjunction with the invention of the laser, played a critical role in the advent of modern optics [142], its original purpose was to measure the angular extent of visible stars. Stellar angular diameters are so small that they appear as point sources in telescopes [139]. Michelson showed that the use of large-baseline interferometers installed on the input of telescopes could successfully resolve stellar diameters down to 0.02 arcseconds [143, 144], which was the state of the art for half of a century. Much like the optical homodyne and heterodyne measurements described in the preceding chapters, the Michelson interferometer relies on interference of the electric field of the incident light to generate a high-SNR modulation signal. In the astronomical case, the modulation takes the form of a spatial fringe pattern in the interfered light waves collected by two spatially separated mirrors. The angular diameter of the star under study is then determined from the minimum mirror separation at which fringes are visible. The Michelson interferometer eventually is limited in its sensitivity to very small stellar diameters by feasability considerations in constructing large and stable mirror base-lines. Small length changes of the telescope arms cause significant fringe variation, as does atmospheric turbulence [139].

The alternative of Hanbury Brown and Twiss was to perform intensity interferometry, rather than field interferometry. In this scenario, the two spatially-separated mirrors are replaced by telescopes mounted to photodetectors [141]. The photocurrents from each measurement location are then correlated electronically, with resulting stellar diameter sensitivities of sub-0.01 arcseconds. In early demonstrations of the apparatus [140], a mercury arc lamp emitted a beam of light which was split into two equal paths, each detected on a photomultiplier. The distance of one of these photomultipliers from the beam splitter was varied, and a variation in coincidence counts was observed in which the correlation decreased as the length change between the detection optical paths was increased. This result, termed “bunching”, sparked intense debate in the optics community, although radio astronomers accepted the finding based on wave interference principles [142]. The controversy surrounding the Hanbury-Brown-Twiss (HBT) effect was due to several simultaneous misunderstandings of the quantum and statistical nature of light and radiation sources. Chief among these confusions was the assumption that the lamp source emitted a coherent beam of light, in which no correlations should be observed. In fact, a coherent beam of light would only be realized in 1960 with the first demonstration of a laser [7]. Contemporary researchers believed that Hanbury Brown and Twiss observed intensity fluctuations of their radiation source, and sought to nullify the correlations by attenuating the light beam in such a way as to produce a single photon preceding the beam splitter [145]. While this rival experiment observed no correlations as hoped, it made another fundamental error in the understanding of light in assuming that the indivisibility of a photon would produce the desired effect. What was not well understood at the time was that a thermal source of photons, attenuated to produce on average a single photon at a time in the apparatus, is not the

same as a single photon number state. Purcell played a key role in avoiding many of the fallacious arguments used by both sides of the debate, and attributed the bunching effect to the statistical distribution of the optical spectrum [146]. While Purcell did in fact correctly identify the correlations as arising from the thermal radiation nature of the mercury arc lamp, this would only be completely understood and resolved by the full characterization of optical coherence by Glauber [147, 148].

5.1.2 Correlations in Light

While astronomical applications of intensity interferometry are concerned with spatial coherence across the transverse dimensions of a light source, temporal coherence is particularly useful for identifying the physical state of the light source. Semiclassically, the first and second order normalized temporal coherence functions of an electromagnetic field are defined through ensemble averages of the electric field $\boldsymbol{E}(r,t)$ as [149],

$$g^{(1)}(\tau) = \frac{\langle E^*(r,t)E(r,t+\tau)\rangle}{\langle E^*(r,t)E(r,t)\rangle}, \tag{5.1}$$

$$g^{(2)}(\tau) = \frac{\langle E^*(r,t)E^*(r,t+\tau)E(r,t)E(r,t+\tau)\rangle}{\langle E^*(r,t)E(r,t)\rangle^2}. \tag{5.2}$$

In the case that these fields are ergodic, the ensemble averages of Eqns. 5.1, 5.2 are equivalent to time averages. Further, disregarding the spatial coherence in order to drop the position variable and expressing $g^{(2)}(\tau)$ in terms of optical intensity $I = |E(r,t)|^2$,

$$g^{(2)}(\tau) = \frac{\langle I(t)I(t+\tau)\rangle}{\langle I(t)\rangle^2}. \tag{5.3}$$

Finally in terms of the fully quantized electromagnetic field, the optical intensity is proportional to the quantum mechanical expectation value of photon number, with $I(t) \propto \langle \hat{a}^\dagger(t)\hat{a}(t)\rangle$. Following the treatment of Glauber [148], evaluation of the correlation function using photodetectors, which apply the photon annihilation operator $\hat{a}$ to the state of the light, begins with considering the transition matrix element between initial ($|i\rangle$) and final ($|f\rangle$) optical states $\langle f|\hat{a}|i\rangle$. The probability of this transition sums the square of this matrix element over all possible final states, with

$$\sum_f |\langle f|\hat{a}|i\rangle|^2 = \sum_f \langle i|\hat{a}^\dagger|f\rangle\langle f|\hat{a}|i\rangle \tag{5.4}$$

$$= \langle i|\hat{a}^\dagger\hat{a}|i\rangle, \tag{5.5}$$

since $\sum_f |f\rangle\langle f| = 1$ by the completeness of the Hilbert space. Similarly, the joint probability of two detections separated in time

$$\sum_f |\langle f|\hat{a}(t+\tau)\hat{a}(t)|i\rangle|^2 = \sum_f \langle i|\hat{a}^\dagger(t)\hat{a}^\dagger(t+\tau)|f\rangle\langle f|\hat{a}(t+\tau)\hat{a}(t)|i\rangle \tag{5.6}$$

$$= \langle i|\hat{a}^\dagger(t)\hat{a}^\dagger(t+\tau)\hat{a}(t+\tau)\hat{a}(t)|i\rangle. \tag{5.7}$$

This property of photodetection puts the operators into what is referred to as normal ordering, where creation operators are all grouped to the left of annihilation operators in expressions. The normalization of Eqn. 5.7 gives

$$g^{(2)}(\tau) = \frac{\langle \hat{a}^\dagger(t)\hat{a}^\dagger(t+\tau)\hat{a}(t+\tau)\hat{a}(t)\rangle}{\langle \hat{a}^\dagger(t)\hat{a}(t)\rangle^2}. \tag{5.8}$$

5.1.2.1 Thermal Source

Chaotic sources of light have the property [139, 149]

$$g^{(2)}(\tau) = 1 + |g^{(1)}(\tau)|^2, \tag{5.9}$$

and thus all of the coherence information is contained in the first order correlation. For a field obeying Lorenztian statistics, with spectral distribution $I(\omega) = |I|\frac{\gamma}{\pi(\gamma^2/4+(\omega-\omega_0)^2)}$ of linewidth γ around a central frequency ω_0, the first order correlation is proportional to the Fourier transform of the spectrum [139, 149, 150], with

$$g^{(1)}(\tau) = e^{-\gamma|\tau|}. \tag{5.10}$$

Therefore at zero time delay, $g^{(2)}(\tau = 0) = 2$, while at long time delays detections are independent with $g^{(2)}(\tau \to \infty) = 1$. This bunching of coincidence counts is the effect observed in the initial HBT experiment [140].

5.1.2.2 Classical Coherent Source

A purely coherent optical wave oscillates at a single frequency ω_0. In other terms, the optical spectrum of such a tone is represented by a δ-function with zero linewidth. The lack of statistical fluctuations thus implies that

$$g^{(2)}(\tau) = g^{(1)}(\tau) = 1 \tag{5.11}$$

for all τ.

5.1.2.3 Quantum Coherent Source

The quantum coherent state is defined as a state $|\alpha\rangle$ which is an eigenvalue of the photon annihilation operator [147], with

$$\hat{a}|\alpha\rangle = \alpha|\alpha\rangle. \tag{5.12}$$

Since Eqn. 5.12 holds for all times, Eqn. 5.8 is solved simply by applying the field operators to the coherent state, and

$$g^{(2)}(\tau) = \frac{\langle\alpha|\hat{a}^\dagger(t)\hat{a}^\dagger(t+\tau)\hat{a}(t+\tau)\hat{a}(t)|\alpha\rangle}{\langle\alpha|\hat{a}^\dagger(t)\hat{a}(t)|\alpha\rangle^2} = \frac{\alpha^2\langle\alpha|\hat{a}^\dagger(t+\tau)\hat{a}(t+\tau)|\alpha\rangle}{\alpha^4} = \frac{\alpha^4}{\alpha^4} = 1. \tag{5.13}$$

This is the state approached by light emitted by conventional optical lasers above their threshold excitation, as will be discussed further in this chapter.

5.1.2.4 Single Photon Source

For a radiation source which emits a single photon at a time, such as an excited two-level atom, it is clear that two photons cannot be detected simultaneously in an HBT apparatus. In this case,

$$g^{(2)}(\tau = 0) = 0, \tag{5.14}$$

while at longer times the second order correlation rises to 1, as photons may be detected which were emitted at different times. This antibunching phenomena, which has no basis in classical theory, was first observed in resonance fluorescence of sodium atoms [151], and unequivocally confirmed the non-classical nature of light. Antibunching in second order correlation continues to be a critical tool in determining the quality of quantum emitters for quantum information purposes [127, 128], such as trapped ions [152], quantum dots [153], and nitrogen-vacancy diamond defects [154].

5.2 Acoustic Intensity Interferometry

Combining Eqns. 4.6 and 5.8 shows that the measurement of Fig. 4.5 maps acoustic coherence onto the sideband photon optical coherence as

$$g^{(2)}(\tau; \Delta = \omega_\mathrm{m}) = \frac{\langle\hat{b}^\dagger(0)\hat{b}^\dagger(\tau)\hat{b}(\tau)\hat{b}(0)\rangle}{\langle\hat{b}^\dagger(0)\hat{b}(0)\rangle^2}, \tag{5.15}$$

$$g^{(2)}(\tau; \Delta = -\omega_\mathrm{m}) = \frac{\langle\hat{b}(0)\hat{b}(\tau)\hat{b}^\dagger(\tau)\hat{b}^\dagger(0)\rangle}{\langle\hat{b}(0)\hat{b}^\dagger(0)\rangle^2}, \tag{5.16}$$

where $t = 0$ has been chosen because of the stationarity of the states under consideration and for simplicity. It is an interesting aside to note that the blue-detuned case of Eqn. 5.16 produces

anti-normally-ordered expectation values, which are not often observed in laboratory experiments. Anti-normal-ordering is produced when detections correspond to emission rather than absorption, in this case of the phonon in the optomechanical resonator. Mandel termed such an arrangement as a "quantum counter" for photons, as opposed to the absorptive photoelectric effect in photodetection. While quantum counters are generally not as useful as photodetectors [139], some proposals for reversible quantum measurement processes rely on detecting anti-normally-ordered correlations [155, 156].

Just as light can exhibit the distinct bunching, non-bunching, and anti-bunching phenomena for the states described in Secs. 5.1.2.1-5.1.2.4, so can the acoustic field of the nanomechanical resonator. For parametrically weak optomechanical interactions, the localized mechanical mode is in a thermal state determined by the environmental bath temperature and should exhibit bunching in the correlation function. A large coherent oscillation of the resonator can be induced by the amplification process of blue-detuned pumping [17, 157] in a situation analogous to a laser oscillation [158], which should produce uncorrelated sideband light. Finally, when the mechanical resonator begins in its quantum ground state and is optomechanically prepared into a phonon number state, anti-bunching should occur [25, 26]. In the following room-temperature experiment, phonon correlations are observed for thermal states and coherent-like displaced thermal states of the nanomechanical resonator.

5.2.1 Phonon Laser Theory

In a conventional laser [159–161], an optical cavity is resonant (or nearly resonant) with the energy difference between two electronic states. Electrons which are externally pumped from the lower energy ground state to the higher energy excited state will decay with a certain probability back down to the ground state. This decay either involves the spontaneous emission of a photon or occurs through non-radiative scattering mechanisms such as phonon emission. However, when a sufficiently large number of electrons are populated into the excited state, an initial spontaneous photon emission will stimulate emission from the other electrons. The transition rate of this stimulated emission heavily favors a frequency and phase overlap with the triggering photon, and thus the stimulated light oscillates coherently in the cavity. As these photons resonate in the optical cavity, they continue to stimulate further emission, and thus exhibit non-linear optical gain of the intracavity field. At high enough external pump power such that the optical gain is equal to the total optical loss in the system, the laser is said to be at threshold. Above threshold the optical gain eventually clamps due to saturation of carrier density, and the output power returns to a linear dependence on input power [161].

A similar situation can be arranged for the acoustic field of an optomechanical resonator, in this case with photons taking the place of electrons as carriers transitioning between two energy levels.

The blue-detuned ($\Delta = -\omega_{\rm m}$) motional sideband functions as the excited state, while the optical cavity resonance frequency is the ground state as illustrated in Fig. 5.1. Blue-detuned pumping produces both amplification of the mechanical mode and optomechanical stiffening, with $\gamma_{\rm OM} = -4G^2/\kappa$. The threshold condition, analagous to the balancing of gain and loss in a conventional optical laser, occurs when $\gamma_{\rm OM} = -\gamma_{\rm i}$, or equivalently, $C = 1$. At threshold the net mechanical damping $\gamma = \gamma_{\rm i} + \gamma_{\rm OM} = 0$ and the oscillator undergoes self-oscillation [17, 157, 162] with a large coherent amplitude. Implementations of acoustic self-oscillation in a harmonically-trapped ion have extended the analogy with a conventional laser by showing that phonon emission is indeed stimulated in this regime [163]. Another optomechanical system consisting of two coupled microtoroids achieved a complete mapping of two-level laser electronic transitions to distinct optical supermodes [164]. Yet another experiment utilizing an optical cavity formed from two distributed Bragg reflectors etched into silicon, one of which being connected to a doubly-clamped microbeam, showed very good agreement with a laser rate equation model for phonons, allowing for the parameterization of phonon laser gain, stored energy, slope efficiency, and saturation power [165].

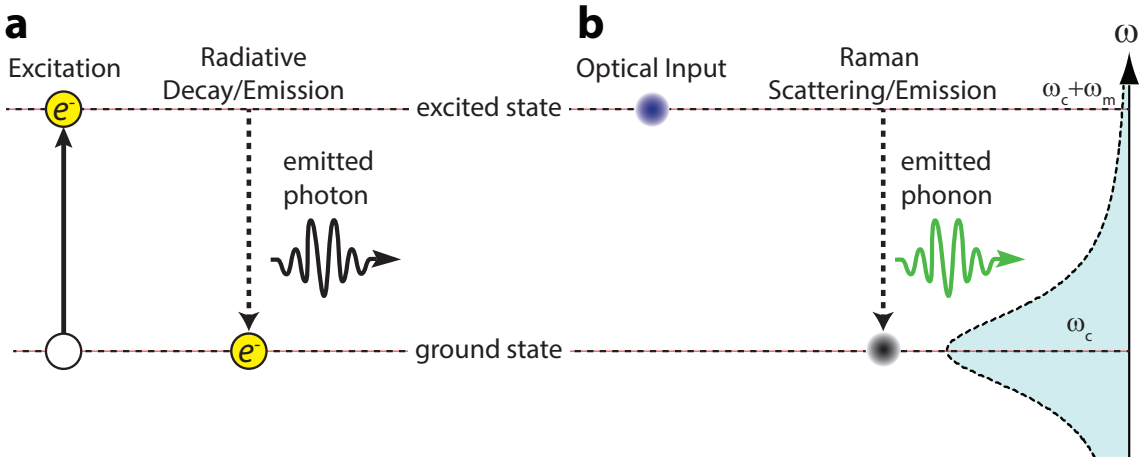

Figure 5.1: **Acoustic Analogue of a Conventional Laser. a** Diagram of a two-level conventional optical laser, with an external excitation process shown for an electron pumped from the ground electronic state to an excited state, and a radiative emission process through either spontaneous or stimulated emission. **b** Diagram of a phonon laser, with an excitation process consisting of an optical input at $\Delta = -\omega_{\rm m}$, and a phonon emission process due to Stokes scattering of the input photon. An example optical spectrum is shown in the dashed Lorentzian curve with respect to the vertical frequency axis, to illustrate the Stokes scattering process resulting in phonon emission.

The following treatment of the limit-cycle oscillation regime of an optomechanical resonator closely follows the anaylses of Refs. [166, 167]. Considering only the classical, complex amplitudes α and β of the quantum operators $\hat{a}$ and $\hat{b}$, respectively, the Langevin equations of motion (Eqns. 1.2

and 1.3) can be rewritten as

$$\dot{\alpha} = -\Big(i\Delta + \frac{\kappa}{2}\Big)\alpha - ig_0\alpha(\beta + \beta^*) - i\Omega + \xi_\alpha, \tag{5.17}$$

$$\dot{\beta} = -\Big(i\omega_\mathrm{m} + \frac{\gamma}{2}\Big)\beta - ig_0\alpha^*\alpha + \xi_\beta, \tag{5.18}$$

where $\Omega = -i\sqrt{\kappa_\mathrm{e}P_\mathrm{in}/\hbar\omega_\mathrm{c}}$ represents the input laser drive with power P_in and ξ_α (ξ_β) is a stochastic noise term proportional to the optical (acoustic) vacuum noise input of Eqn. 1.2(Eqn. 1.3). In the parameter space of interest to this work, where $\gamma \ll \kappa$, the acoustic dynamics vary slowly on the time scale of the optical cavity. Assuming a time-evolution for the acoustic phase-space limit cycle of the form $\beta(t) = \beta_\mathrm{c} + Be^{-i\phi}e^{-i\omega_\mathrm{m}t}$ for some oscillation center β_c, oscillating amplitude B, and arbitrary phase ϕ, the corresponsing optical solution can be split into average and fluctuating components $\alpha(t) = \langle\alpha(t)\rangle + \delta\alpha$, where the time-averaged component represents the solution obtained by omitting the fluctuating component.

In Fourier space, the nonlinear oscillation induces multiple sidebands to the optical amplitude at multiples of the mechanical frequency, with solution

$$\langle\alpha(\omega)e^{-izsin(\phi+\omega t)}\rangle = \sum_n \alpha_n\delta(\omega - n\omega_\mathrm{m}) \tag{5.19}$$

$$= \frac{-i\Omega\sum_n J_{-n}(z)e^{i\phi n}\delta(\omega - n\omega_\mathrm{m})}{\kappa/2 + i(\omega - \Delta + 2g_0\mathrm{Re}[\beta_\mathrm{c}])}, \tag{5.20}$$

$$\delta\alpha(\omega)e^{-izsin(\phi+\omega t)} = \frac{\xi\text{`}_\alpha e^{-izsin(\phi+\omega t)}}{\kappa/2 + i(\omega - \Delta + 2g_0\mathrm{Re}[\beta_\mathrm{c}])}. \tag{5.21}$$

$J_n(z)$ is a Bessel function of the first kind with argument $z = 2g_0B/\omega_\mathrm{m}$. Neglecting optical fluctuation terms of order 2 and higher, and retaining only the first-order component of the product $\langle\alpha\rangle\langle\alpha^*\rangle$, the equation of motion for the oscillating component $\tilde{\beta}(t) = \beta(t) - \beta_\mathrm{c}$ can then be written as

$$\dot{\tilde{\beta}} = -\frac{\gamma_\mathrm{OM} + \gamma_\mathrm{i}}{2}\tilde{\beta} - i(\omega_\mathrm{m} + \delta\omega_\mathrm{m})\tilde{\beta} + \xi_\beta - ig_0(\langle\alpha^*\rangle\delta\alpha + \langle\alpha\rangle\delta\alpha^*), \tag{5.22}$$

Limit-cycle oscillation can thus be induced by balancing the decaying first term of Eqn. 5.22 to equate the optomechanical gain γ_OM with the intrinsic mechanical resonator loss γ_i, with

$$\gamma_\mathrm{OM} = \frac{4g_0^2|\Omega^2|}{\omega_\mathrm{m}}\mathrm{Im}\Big[\sum_n \frac{J_n(z)J_{n+1}(z)}{zh_nh_{n+1}^*}\Big] = -\gamma_\mathrm{i}, \tag{5.23}$$

where $h_n = \kappa/2 + i(\Delta + n\omega_\mathrm{m})$.

Ref. [166] goes on to study the amplitude and phase fluctuations of the mechanical motion. The equation of motion for the amplitude of the coherent oscillation is

$$\dot{B} = -\frac{\gamma}{2}B + \xi_\mathrm{T}^-, \tag{5.24}$$

where the noise term is

$$\xi_{\mathrm{T}}^{\pm} = \frac{1}{2}(\xi_{\beta} e^{i(\phi+\omega_{\mathrm{m}}t)} \pm \xi_{\beta^*} e^{-i(\phi+\omega_{\mathrm{m}}t)}) - \frac{ig_0}{2}(\langle\alpha^*\rangle\delta\alpha + \langle\alpha\rangle\delta\alpha^*)(e^{i(\phi+\omega_{\mathrm{m}})} \pm e^{-i(\phi+\omega_{\mathrm{m}}t)}), \tag{5.25}$$

with the ξ_{T}^{+} term relating to phase diffusion.

Defining a diffusion constant D_{T} from the autocorrelation of $\xi_{\mathrm{T}}^{-}(t)$, averaged over a mechanical oscillation period,

$$D_{\mathrm{T}} = \lim_{\omega\to 0} \omega_{\mathrm{m}} \int_0^{2\pi/\omega_{\mathrm{m}}} \int_{\infty}^{\infty} \langle \xi_{\mathrm{T}}^{-}(\omega)\xi_{\mathrm{T}}^{-}(\omega')\rangle e^{i(\omega+\omega')t} d\omega' dt \tag{5.26}$$

$$= \frac{1}{2}(D_{\mathrm{m}} + D_{\mathrm{BA}}^{-}). \tag{5.27}$$

The total diffusion is composed of a contribution from the thermalization of the acoustic resonator to the ambient environment $D_{\mathrm{m}} = \frac{1}{2}\gamma_{\mathrm{i}}(n_{\mathrm{th}} + \frac{1}{2})$, and an optomechanical back-action component

$$D_{\mathrm{BA}}^{\pm}(z) = \frac{\kappa g_0^2 |\Omega|^2}{2} \sum_n \frac{1}{|h_n|^2} \left| \frac{J_{n-1}(z)}{h_{n-1}} \pm \frac{J_{n+1}(z)}{h_{n+1}} \right|^2, \tag{5.28}$$

with D_{BA}^{-} again relating to phase diffusion. The steady-state solution to Eqn.5.24 of the exponential form $e^{-U(B)}$, with

$$U(B) = \int_0^B \frac{2B'(\gamma_{\mathrm{i}} + \gamma_{\mathrm{OM}}(B'))}{D_{\mathrm{m}} + D_{\mathrm{BA}}^{-}(B')} dB', \tag{5.29}$$

can then be used to solve for the average acoustic occupation $\langle n\rangle$ and fluctuations thereof. A particularly useful figure of merit for the state of the acoustic resonator is the Fano factor, given by the division of the occupancy variance by the mean $F = (\Delta n)^2/\langle n\rangle$. As a coherent oscillation would exhibit Poissonian statistics in which the variance is equal to the mean, $F = 1$ would be expected well above threshold for a laser. In thermal and Fock states, the super-Poissonian and sub-Poissonian distributions in occupation would similarly produce Fano factors larger and smaller than 1, respectively.

In the limit-cycle regime, with amplitude B_0 meeting the condition of Eqn. 5.23, the exponential amplitude solution is well-described by a Gaussian with width $\sigma^2 = (D_{\mathrm{m}} + D_{\mathrm{BA}}^{-})/(2B_0 \frac{d\gamma_{\mathrm{OM}}}{dB}|_{B_0})$ and corresponding Fano factor

$$F = \left(n_{\mathrm{th}} + 1 + \frac{g_0^2 B_0^2}{\omega_{\mathrm{m}}}\right) \left[\frac{J_1(z)}{J_1(z) - zJ_1'(z)}\right]_{B_0} \tag{5.30}$$

in the sideband-resolved regime of $\kappa \ll \omega_{\mathrm{m}}$. The analytical and computational results of Ref. [166] show that the Fano factor decreases when the acoustic resonator is deep in its limit-cycle regime, and that the amplitude fluctuations are reduced from that of a thermal state harmonically-driven to the same oscillation amplitude, as expected when the acoustic field begins to exhibit coherent,

Poissonian statistics.

5.2.2 Threshold Behavior

Upon pumping of the blue motional sideband with a high-power laser input, the nanobeam optomechanical resonator displays a pronounced threshold effect with respect to intracavity photon number, as shown in Fig. 5.2. The Stokes sideband count rate (Fig. 5.2a) detected on a single SPD (as in the apparatus of Fig. 4.5) increases exponentially beginning at $n_c \approx 1200$, where $C \approx 0.8$ in agreement with the expected onset of instability around $C = 1$.

The average phonon occupancy $\langle n \rangle$ is also extracted from the SPD count rate on the right axis of Fig. 5.2a. Since the optical filtering of the cavity output selects only the first Stokes sideband at $\omega = \omega_l - \omega_m$, the corresponding intracavity photon number is that of the first series term of Eqn. 5.20, $n_1 = |\alpha_1|^2$. Well-below threshold, the room-temperature thermal occupation of the acoustic resonator $n_{th} \approx 1100$ can be used in a linear approximation of $n_1 = 4G^2 n_{th}/\kappa^2$. Near and above threshold, n_1 can be determined from the ratio of SPD count rates above and below threshold and the known value of n_1 below threshold. The value of n_1 for a given input power can be further be used to compare to the model of Ref. [166] by solving for the amplitude of oscillation B and detuning Δ commensurate with Eqns. 5.20 and 5.23. For the highest input power, we find $\Delta \approx -1.067\omega_m$ and $z \approx 0.15$ (with corresponding $B = z\omega_m/(2g_0)$). This amplitude is small enough that the linear approximation $\alpha_1 \propto z$ is still valid, and that the relation $J_1(z) \approx z/2$ should hold. For the largest value of z in this measurement, $J_1(z)$ differs from $z/2$ by only about 0.3 %. While the detuning shift from the mechanical sideband frequency is comparable to the cavity linewidth, it is a static shift derived from a fully nonlinear theory, and as such is not at odds with the linear response of the optical cavity in the limit cycle regime. The shift in detuning, and concomitant reduction in oscillation amplitude, is expected due to the thermo-optic effect, which will tend to shift the cavity resonance to lower frequencies as the total intracavity photon populations is increased by the amplified Stokes scattering [168]. This thermo-optic shift has been previously observed in similar nanobeam OMC structures [42].

The sharp oscillation threshold can also be observed spectrally from the mechanical NPSD (Fig. 5.2b) in which the amplitude of the mechanical spectrum is seen to rapidly increase with a simultaneous reduction in linewidth. The generation of coherence in the acoustic field can also be observed in plots of the in-phase and in-quadrature components of the photocurrent (produced by a fast-response photodetector) as shown in Fig. 5.2c. At low pump power, the phase-space is occupied by thermal noise , while near threshold a large coherent oscillation (represented by a circle in phase-space) is seen to rapidly decay back to thermal, chaotic motion. Well above threshold, the coherent oscillation is sustained for the duration of the pump input and does not decay to a thermal state. The state of the mechanics in this regime is not completely described by a coherent

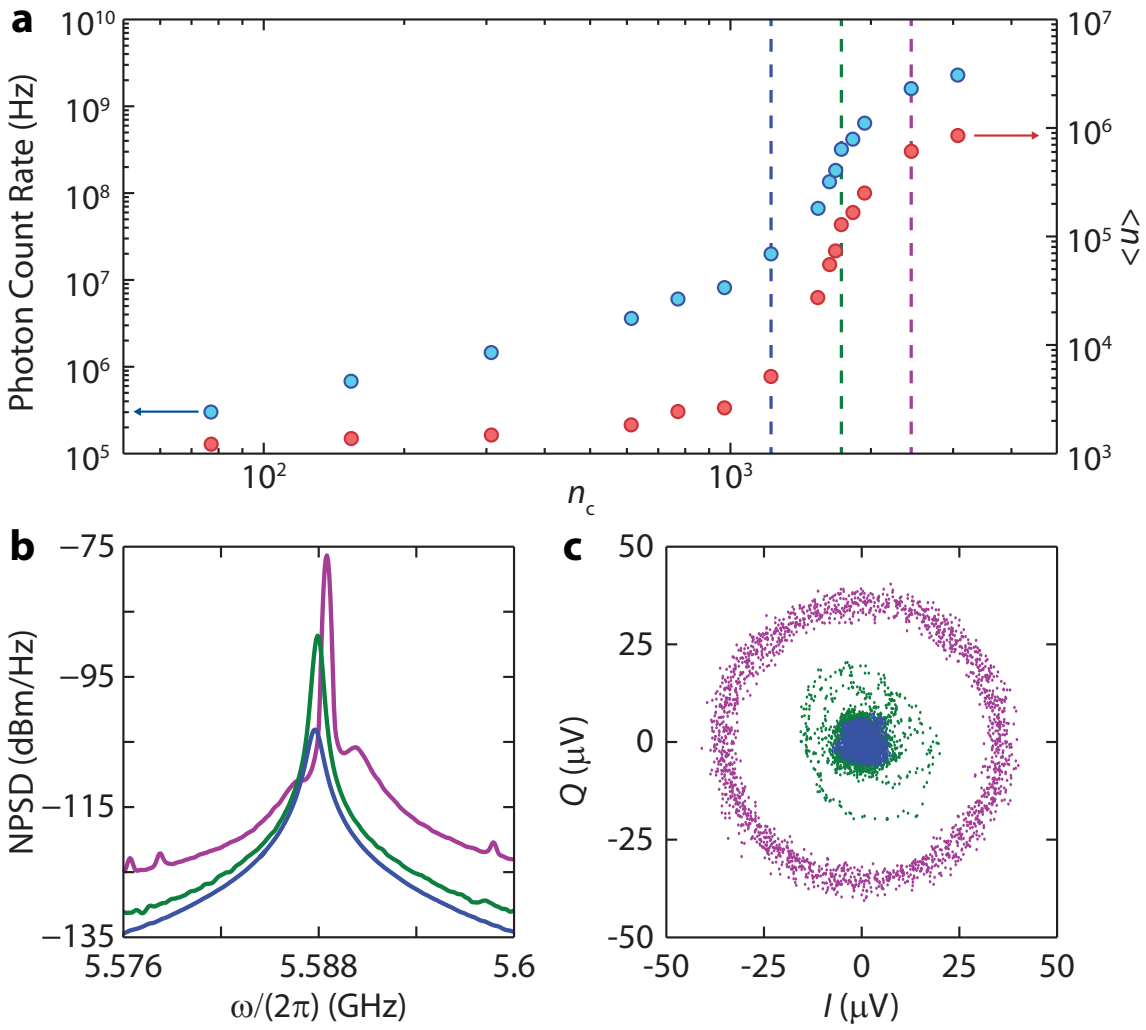

Figure 5.2: **Threshold Behavior at Onset of Self-Oscillation.** **a** Photon count rate (blue, left axis) measured as a function of n_c for a blue-detuned ($\Delta = -\omega_m$) laser drive. The absolute photon count rate, which takes values well above the maximum SPD count rate of $1e6$ Hz, is determined from the SPD count rate and the attenuation factor of the VOA preceding the VC. Average phonon occupancy $\langle n \rangle$ is extracted from photon count rate and calibrations of the optomechanical transduction, and is plotted in red points with respect to the left axis. The dashed vertical lines indicate photon numbers below (blue), at (green), and near self-oscillation threshold (purple), for which data were acquired for **b** and **c**. **b** Representative mechanical noise power spectral densities (NPSD) acquired on an RSA showing nonlinear amplitude increase and linewidth narrowing. Line colors correspond to the dashed lines in **a**. The small satellite peaks in the thermal emission background of the above threshold spectrum correspond to beating of the phonon laser line with low frequency modes of the nanobeam structure. **c** Phase plots of the in-phase (I) and in-quadrature (Q) amplitudes of the optical heterodyne signal for each of the dashed lines in **a**, acquired in a 36 MHz span around 5.588 GHz over a 60 second time interval.

state however, as the acoustic field still exhibits thermal noise. This thermal noise manifests in the annular distribution in the above-threshold phase-space, whereas a pure coherent state would be represented by a thinner annulus circle. The mechanical state above threshold is thus best described

as a displaced thermal state [169]. A displaced thermal state is the generalization of a coherent state, which is represented in phase space by a circle with radius of the zero-point fluctuations of the oscillator and with a center that is displaced from the origin by a well-defined amplitude, to a finite thermal occupancy, which manifests in phase space by increasing the noise circle radius to the thermal noise level.

5.2.3 Phonon Counting HBT Apparatus

The full experimental setup for phonon counting and intensity interferometry is shown in Fig. 5.3. A fiber-coupled, wavelength tunable external cavity diode laser is used as the light source, with a small portion of the output sent to a wavemeter module (λ-meter) for frequency stabilization of the laser detuning from optical resonance. The remaining laser power is sent through an electro-optic phase modulator (ϕ-m) and a variable optical attenuator (VOA) to allow control of the input power to the optomechanical resonator. The signal is then sent through an optical circulator to a lensed fiber tip, which end-couples to the device under test as described in Sec. 2.2. The cavity reflection couples back into the lensed-fiber, and passes through the circulator to the one of two detection paths of the setup. The first position of optical switch SW2 routes the signal either to a power meter (PM) for calibration of the reflected signal power, or to an erbium-doped fiber amplifier (EDFA) followed by a high-speed photodetector (PD). The detected photocurrent is either sent to a real-time spectrum analyzer (RSA) in order to measure the noise power spectral density (NPSD) of the mechanical modulation or to a vector network analyzer (VNA) for full characterization of the intensity and phase response of the optical cavity.

The second position of SW2 sends the signal to a series of narrowband tunable Fabry-Perot filters. The filter transmission is sent through a variable fiber coupler (VC), which is tuned to produce equal photon count rates on the two single-photon detectors (SPDs) coupled to its output. The electrical pulses generated by the SPDs are used as start and stop triggers of a Picoharp 300 Time-Correlated Single-Photon Counting (TCSPC) module, which measures the individual SPD count rate as well as integrates a histogram of photon arrival events with respect to the time delay between detection events of SPD1 and SPD2.

Since the pump laser is tuned to a motional sideband during the phonon counting measurement, the two Fabry-Perot filters are first tuned to the optical cavity resonance via an initial lock and stabilization procedure. First, the laser detuning is adjusted to a motional sideband by optimizing the mechanical transduction signal on the RSA. Since the power of the radiated Stokes- or anti-Stokes-scattered light is too low to provide a feedback signal for filter stabilization, we then bypass the cavity, and apply a phase modulation to the pump at the frequency of the mechanical resonance ω_{m}. The signal is switched into the filter path of the setup, and a small portion (2 %) of the filter transmission is detected on an Eigenlight series 100 fiber monitor. The photocurrent is then used

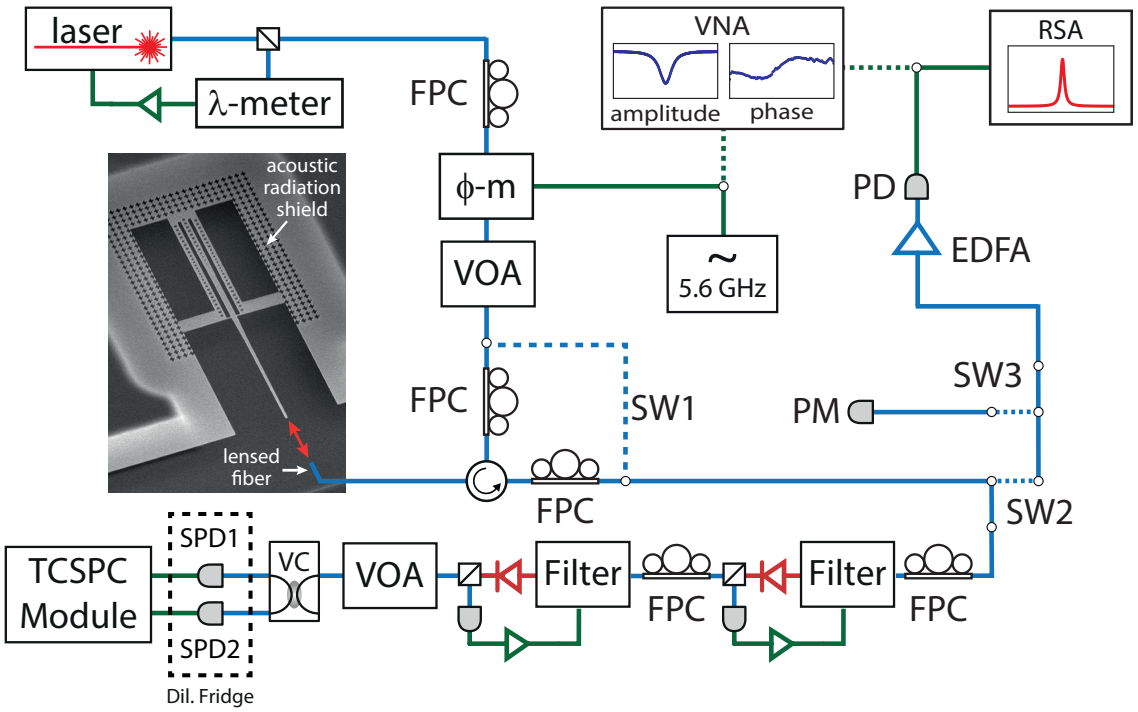

Figure 5.3: **Phonon Correlation Spectroscopy Apparatus.** Diagram of the setup for phonon counting, correlation spectroscopy, and optomechanical calibration. Abbreviations are defined as λ-meter: wavelength meter, FPC: fiber polarization controller, ϕ-m: electro-optic phase modulator, VOA: variable optical attenuator, SW: optical switch, PM: power meter, EDFA: erbium-doped fiber amplifier, PD: fast photodetector, RSA: real-time spectrum analyzer, VNA: vector network analyzer, VC: variable coupler, SPD: single photon detector, and TCSPC: time-correlated single photon counting.

as a feedback signal while the filter frequency is dithered and tuned via a piezoelectric motor to produce the maximum transmission. This is performed for each filter, resulting in alignment of the full filter path to the optical cavity resonance. After a stabilization period of a few seconds, the filter piezoelectric tuning signal is held without further feedback. The pump modulation is then turned off, the CW power adjusted with the VOA to produce the desired n_c and the device under test is switched back into the optical path. Once locked, the transmission of the filters is observed to be stable to within 5-10 % for several minutes in the absence of active feedback locking.

In order to avoid pile-up artifacts in the acquired $g^{(2)}(\tau)$ histograms [126], the photon count rate incident on the SPDs is kept at or below 30 kHz. This is accomplished with a VOA between the filters and VC, and is sufficient to maintain a flat histogram over a 5 μs time delay window.

To determine the validity of any observed optomechanically induced photon correlations, the optomechanical paramters of the device are first determined, and then used as the basis for models of $g^{(2)}(\tau)$ in comparison with data. Full characterization of the optical resonance involves measuring the fiber-to-waveguide coupling efficiency $\eta_{\rm cpl}$, the total optical energy rate κ, and the cavity coupling

depth κ_e/κ. The fiber collection efficiency is determined in the apparatus PM calibration path by observing the optical reflection far from resonance with the cavity, and yields $\eta_{cpl} = 0.63$. The total cavity decay rate is determined by fitting the optical reflection intensity spectrum (Fig. 5.4a) to a Lorentzian lineshape, yielding $\kappa/2\pi = 818$ MHz, which corresponds to an optical quality factor Q_o =236,000. The reflection level on resonance, when normalized to the off-resonance reflection level, is related to the cavity coupling depth by $R_0 = (1 - 2\kappa_e/\kappa)^2$. However, for single-sided optical coupling this is not a single-valued function of coupling depth. Consequently, full optical characterization requires measurement of the phase response of the cavity. First the laser detuning is locked far off-resonance from the cavity, and then the output of the VNA is used to drive the electro-optic phase modulator to sweep an optical pump sideband across the cavity lineshape. The PD output is then measured on the VNA, which computes the full complex frequency response of the device. Fitting the phase component (Fig. 5.4b) with prior calibration of the cavity resonance and decay rate yields $\kappa_e/\kappa = 0.52$.

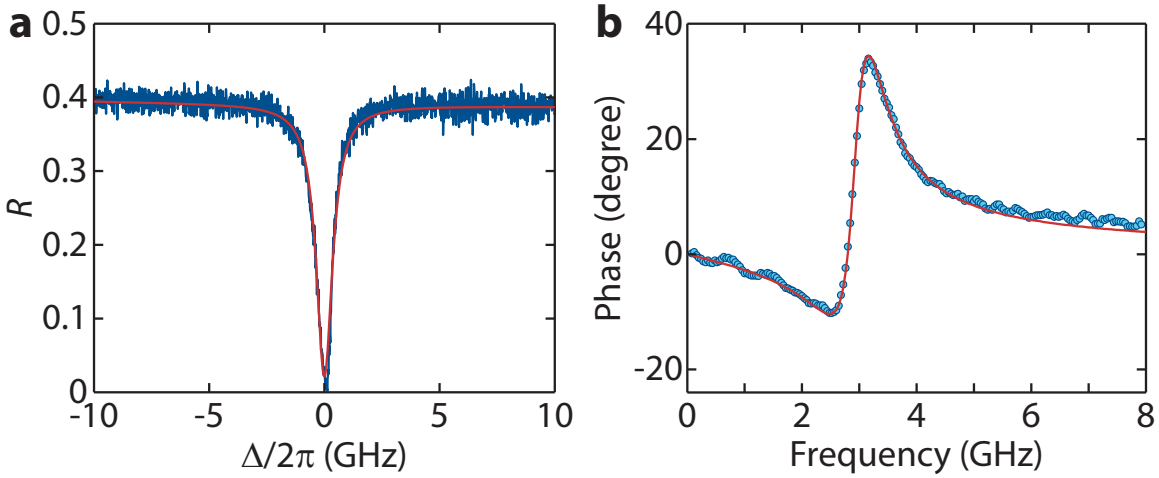

Figure 5.4: **Optical Cavity Intensity and Phase Response.** Calibration of optical cavity parameters with a vector network analyzer (VNA). **a** The optical reflection spectrum (blue) versus detuning Δ with a Lorentzian fit (red) shows a total optical quality factor of Q_o =236,000. **b** A fit of the optical phase response yields $\kappa_e/\kappa = 0.52$.

To characterize the acoustic resonance, the cavity reflection is sent to the spectrum analysis path, with the EDFA-amplified signal detected on the fast photodiode and the noise power spectral density (NPSD) measured on the RSA. The Lorentzian response due to transduction of the acoustic thermal Brownian motion can be observed at the acoustic resonance frequency $\omega_m/2\pi = 5.6$ GHz. For a pump laser locked onto the red or blue mechanical sideband of the cavity, the linewidth of the transduced signal is given by $\gamma = \gamma_i \pm \gamma_{OM}$, where $\gamma_{OM} = \pm 4g_0^2 n_c/\kappa$. The dependence of linewidth for both detunings versus n_c is shown in Fig. 5.5. By averaging the two sets of data, the γ_{OM} contribution can be cancelled out and the intrinsic acoustic damping rate is found to be $\gamma_i = 3$ MHz,

(equivalently, the mechanical quality factor $Q_{\rm m} = 1850$). Fitting the difference $\gamma_{\rm OM} = |\gamma - \gamma_{\rm i}|$ as a function of $n_{\rm c}$, the optomechanical coupling rate is found to be $g_0 = 645$ kHz.

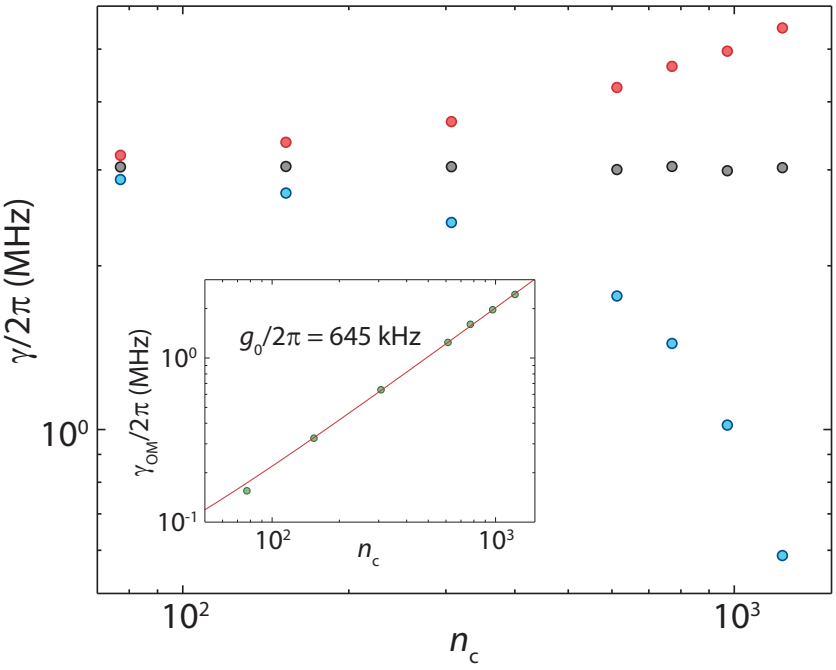

Figure 5.5: **Calibration of g_0. a** Mechanical linewidth γ versus $n_{\rm c}$ for $\Delta = -\omega_{\rm m}$ (blue) and $\Delta = \omega_{\rm m}$ (red). The intrinsic mechanical linewidth $\gamma_{\rm i}$ (black) is determined by averaging the detuned linewidths to cancel out the contribution of $\gamma_{\rm OM}$, and yields a mechanical quality factor of $Q_{\rm m} = 1850$ at room temperature. The inset shows the optomechanically induced damping rate $\gamma_{\rm OM}$ obtained by subtracting $\gamma_{\rm i}$ from γ. The linear fit shown in the red solid line yields a vacuum optomechanical coupling rate of $g_0 = 645$ kHz.

5.2.4 Histogram Coherence Characterization

With the optical and mechanical device properties fully characterized, the photon correlation in cavity reflected light is analyzed in the filter path of the setup. With the VC oriented to produce equal photon count rate $\Gamma_{\rm SB}$ on SPD1 and SPD2, this portion of the setup functions as an HBT apparatus, with the temporal second order correlation function integrated on the TCSPC module for an integration time $t_{\rm int}$ (usually of a few minutes). The correlation function is normalized to represent $g^{(2)}(\tau)$ by dividing the number of counts within each 512 ps width time bin by 512 ps$\times t_{\rm int}\Gamma_{\rm SB}^2$. With the probe laser detuned to either a red or blue motional sideband, and for low intracavity photon number $n_{\rm c} = 77$ (far below self-oscillation threshold) the histogram shows strong bunching towards zero time delay (Fig. 5.6a,e), and decays exponentially from $g^{(2)}(0) = 2$ to $g^{(2)}(t \to \infty) = 1$ in good agreement with the expected form of Eqn. 5.10. Just as in the HBT experiment, this bunching is a signature of a thermal source of photons. Since the probe laser emits Poissonian distributed,

un-bunched light, the only source for these photons to take on a thermal distribution is through Raman scattering from the acoustic resonance. Already this feature shows that the optomechanical interaction in the system maps the physical state of the mechanics onto the sideband scattered light, an important prerequisite of quantum information processing tasks using optomechanics.

At low power, the optomechanically induced damping is low, and the decay rate of the mechanics for both red and blue detuning is equal to γ_{i}. This is also observed in the low power histograms, which show the same exponential decay between both detunings. As power is increased approaching threshold, the blue-detuned histograms begin to show longer decay times and red-detuned histograms show faster decay (Fig. 5.6b,f for $n_{\mathrm{c}} = 1200$). Increasing power further, at the threshold intracavity photon number $n_{\mathrm{c}} = 1700$ the blue-detuned bunching begins to decrease as $g^{(2)}(0)$ begins to decrease from 2, while the red-detuned histogram remains bunched. Finally, well-above the phonon lasing threshold with $n_{\mathrm{c}} = 2400$, the blue-detuned histogram shows very little bunching as the mechanical resonator exhibits Poissonian statistics with $g^{(2)}(\tau) = 1$. The zero-delay photon correlation is plotted for a range of n_{c} in Fig. 5.7. As observed in the full histograms, the red-detuned correlation function remains bunched for all n_{c} with $g^{(2)}(0) = 2$, signifiying that for this measurement the mechanical resonator remains in a thermal state through threshold and beyond. The blue-detuned correlation shows a smooth transition from $g^{(2)}(0) = 2$ to $g^{(2)}(0) = 1$ as the self-oscillation threshold is crossed. This type of observation was critical in the early modelling of conventional lasers as Van der Pol oscillators [170, 171].

5.2.5 Decoherence Lifetime and Fano Factor

The decay rate of the acoustic resonator, measured from both the linewidth of the NPSD and from an exponential fit of $g^{(2)}(\tau)$ below threshold, is plotted in Fig. 5.8a versus the power of a blue-detuned laser drive. The decay rate as measured from the NPSD, which includes both phase and amplitude fluctuations, is seen to increase around threshold before continuing to decrease at higher probe powers. This behavior is commonly observed in semiconductor lasers where a coupling exists between the gain and the cavity refractive index [159]. A similar effect arises in optomechanical oscillators due to the optical spring effect [166]. On the other hand, the decay rate measured from $g^{(2)}(\tau)$, which measures only intensity fluctuations, begins to deviate from the measured linewidth in the vicinity of threshold. Although thermal phonon emission dictates a strict correspondence between the second-order and first-order coherence functions [148], above threshold where the phonon statistics are no longer purely thermal, such a deviation is possible, and in fact predicted for self-sustaining oscillators [172].

The Fano Factor, defined as

$$F = \frac{(\Delta n)^2}{\langle n \rangle} = 1 + \langle n \rangle (g^{(2)}(0) - 1), \tag{5.31}$$

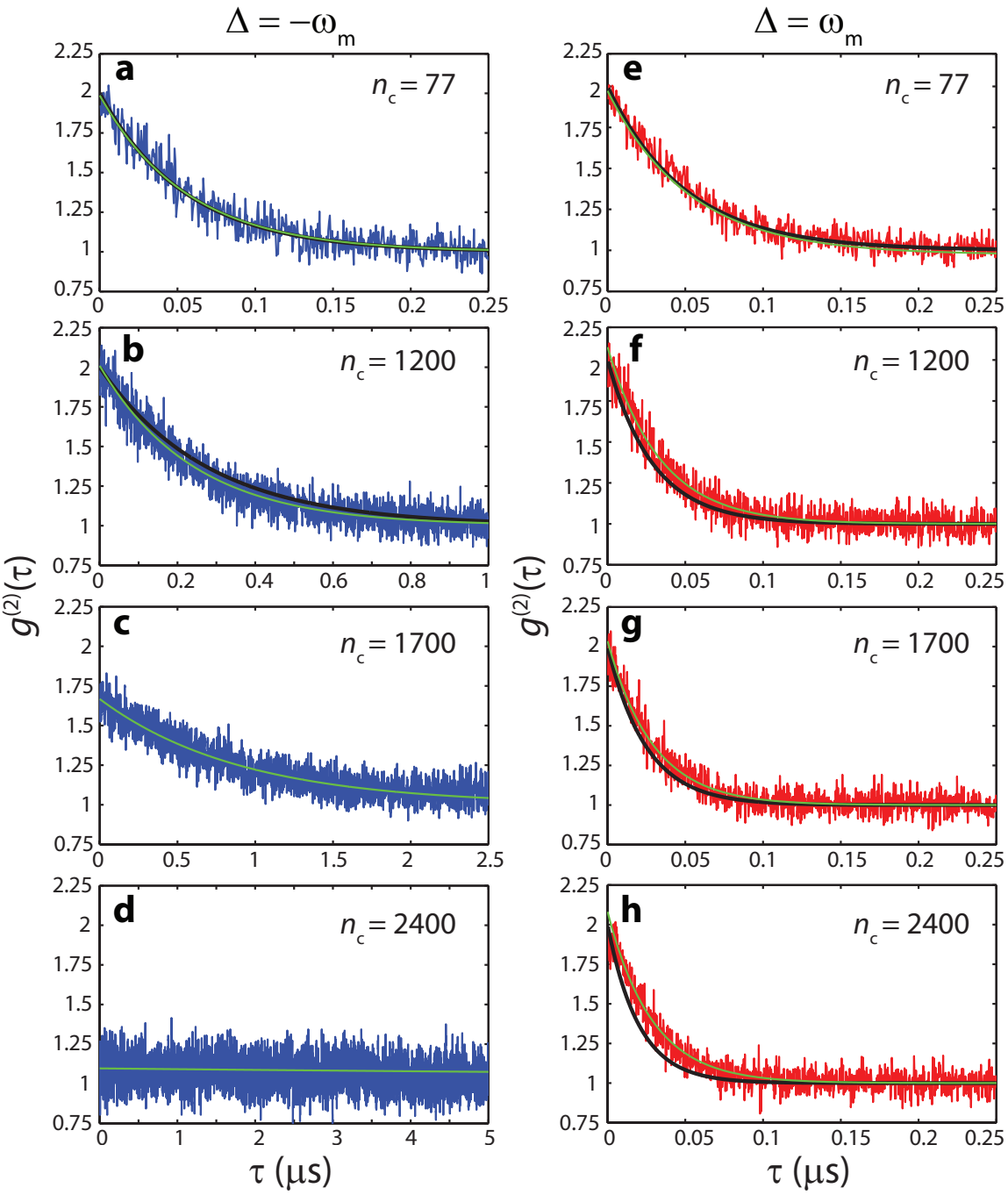

Figure 5.6: **Second-Order Temporal Phonon Correlation Function.** Second order phonon correlation function $g^{(2)}(\tau)$ measured via histograms produced in TCSPC, for representative photon numbers n_c with a blue-detuned (**a-d**) and red-detuned (**e-h**) laser drive. Exponential decay fits are plotted in green lines, while the expected decay function based on calibration of γ_i and γ_{OM} is plotted in black for the below-threshold histograms (**a**,**b**, **e-h**). The blue-detuned histograms show a smooth transition from thermal bunching to uncorrelated phonon emission, while the red-detuned histograms remain bunched at all photon numbers.

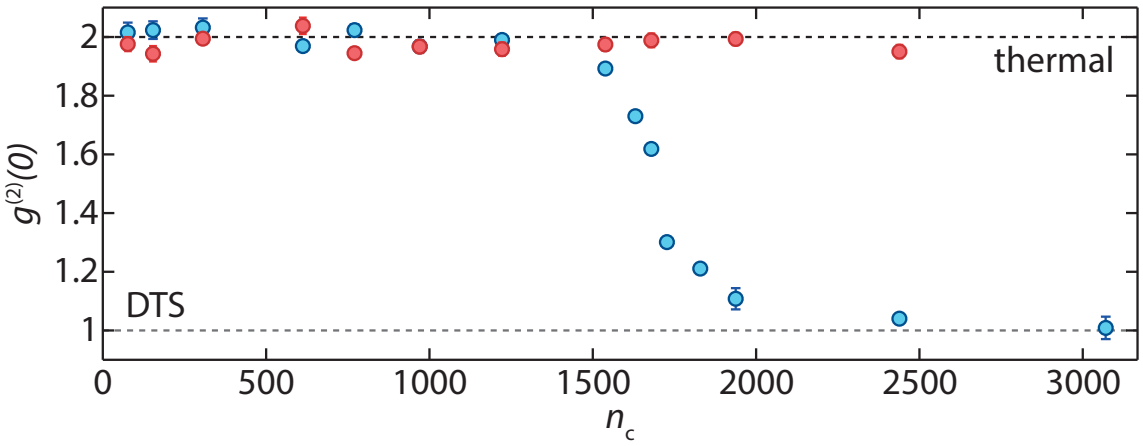

Figure 5.7: **Zero-Delay Phonon Correlation.** Second order phonon correlation function $g^{(2)}(0)$ versus n_c for $\Delta = -\omega_m$ (blue points) and $\Delta = \omega_m$ (red points). The top and bottom dashed lines indicate the expected values for purely thermal and for displaced thermal states (DTS), respectively. Error bars indicate one standard deviation from the mean produced by the error in fitting $g^{(2)}(\tau)$.

provides additional statistical information about the fluctuations of the oscillator, and is useful for defining a precise oscillator threshold [173] and distinguishing between states that may have similar or identical values of $g^{(2)}(0)$ (e.g. a coherent state versus a DTS) [166]. Inferring $\langle n \rangle$ from the sideband photon count rate (Fig. 5.2) via

$$\langle n \rangle = \frac{\kappa \Gamma_{SB}}{\kappa_e \eta} - 1, \tag{5.32}$$

and using the measured $g^{(2)}(0)$, the Fano factor of the mechanical oscillator plotted in Fig. 5.8b shows the expected increase and peak in fluctuations at threshold. Above threshold, the Fano factor drops again due to saturation in the optomechanical gain, approaching a measured value consistent with that of a DTS ($F \sim 2n_{th} + 1$).

5.3 Outlook for Quantum Regime Phonon Counting and Intensity Interferometry

Although this analysis has emphasized the analogy between the optomechanical oscillator and a conventional laser, there are unique differences which arise due to the intrinsically nonlinear nature of the radiation pressure interaction in an optomechanical cavity. A particularly interesting departure from classical phonon lasing dynamics is found in Ref. [166], for which the Fano factor determined by the diffusion constants of Eqn. 5.28 falls below a value of 1 when the thermal phonon occupancy $n_{th} \approx 0$. This is a uniquely nonclassical feature produced by anti-bunched phonon statistics. Under slightly

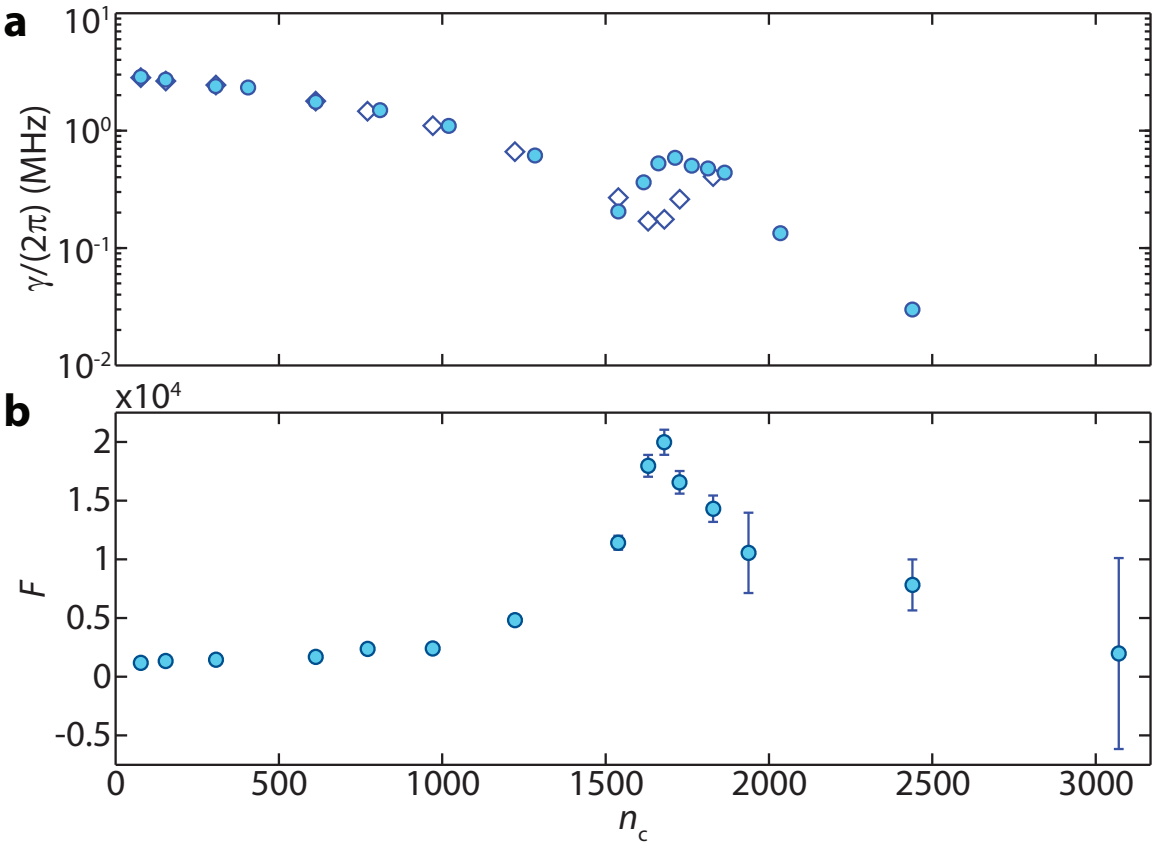

Figure 5.8: **Mechanical Decay and Fano Factor.** **a** Mechanical decay rate versus n_c for $\Delta = -\omega_m$, determined from the measured linewidth of the NPSD (circles) and from the exponential fit to $g^{(2)}(\tau)$ (diamonds). **b** Fano factor versus n_c determined by measurement of $\langle n \rangle$ and $g^{(2)}(0)$.

more restrictive conditions, laser-driving the optical cavity on-resonance can also produce limit-cycle oscillations with strongly negative Wigner density [174, 175]. Surprisingly, this is predicted to be observable even for classical parameters (i.e., outside the single-photon strong-coupling regime of $g_0/\kappa < 1$), and in the presence of thermal noise.

Beyond phonon correlation spectroscopy, it is envisioned that sensitive photon counting of the filtered motional sidebands may be utilized in the preparation and heralding of non-Gaussian quantum states of a mechanical resonator [25, 26]. Most proposals for the creation of nonclassical mechanical states rely on single-photon strong coupling of the optical and acoustic fields [55, 56, 59, 60], in which a single photon in the optical cavity shifts the mechanical oscillator by more than its zero-point fluctuation level with $\kappa, \omega_m \ll g_0$. As this regime has not yet been reached in the laboratory, with state-of-the-art optomechanical resonators featuring $g_0/\kappa < 10^{-2}$ [45], schemes for creating and observing quantum states of the mechanics in the weak-coupling regime ($g_0 < \kappa, \omega_m$, as in this work) are highly sought. Two recent proposals by Vanner and colleagues (Ref. [25]) and Galland and colleagues (Ref. [26]) have outlined phonon addition and subtraction processes for the projection and

heralding of phonon number states in the weak-coupling regime. These processes are particularly well-suited to the phonon counting and intensity interferometry developed in this work.

Using the analysis of Ref. [26], the following discussion investigates the feasability of using a pulsed laser input to first drive the blue mechanical sideband to create and herald a single-phonon Fock state, and second verify the quantum nature of the mechanical state by monitoring the red sideband. In the first step, a blue-detuned laser pulse produces the Langevin equations of motion in the sideband-resolved ($\kappa \ll \omega_{\rm m}$) and weak-coupling regimes

$$\dot{\hat{a}} = \frac{i}{\hbar}[\hat{H}_{\rm BSB}, \hat{a}] - \frac{\kappa}{2}\hat{a} + \sqrt{\kappa}\hat{a}_{\rm in}, \tag{5.33}$$

$$\dot{\hat{b}} = \frac{i}{\hbar}[\hat{H}_{\rm BSB}, \hat{b}] - \frac{\gamma}{2}\hat{b} + \sqrt{\gamma}\hat{b}_{\rm in}, \tag{5.34}$$

where the interaction Hamiltonian $\hat{H}_{\rm BSB} = -\hbar G\hat{a}^\dagger\hat{b}^\dagger + \text{h.c.}$ produces correlated phonon/resonant-photon pairs, and the strongly overcoupled regime of $\kappa = \kappa_{\rm e}$ has been chosen for simplicity.

For the condition that the mechanical decoherence time is long in comparison to the pulse cycle (on-state duration $T_{\rm write}$ and off-state duration $T_{\rm off}$), the mechanical dynamics can be neglected as slowly varying in the time-frame of the experiment. The intracavity field during the blue-detuned drive, or write pulse, then reduces to $\hat{a}_{\rm write}(t) = (2/\kappa)(iG\hat{b}^\dagger_{\rm write} + \sqrt{\kappa}\hat{a}_{\rm write,in})$. The optical cavity output field is then coupled to the acoustic field through

$$\hat{a}_{\rm write,out} = \hat{a}_{\rm write,in} + i\sqrt{2G_{\rm write}}\hat{b}^\dagger_{\rm write}, \tag{5.35}$$

$$\dot{\hat{b}}_{\rm write} = G_{\rm write}\hat{b}_{\rm write} + i\sqrt{2G_{\rm write}}\hat{a}^\dagger_{\rm write,in}, \tag{5.36}$$

where $G_{\rm write} = 2G^2/\kappa$. For solutions to Eqn. 5.35 of the form

$$\hat{A}_{\rm write,in(out)}(T_{\rm write}) = \sqrt{\frac{\pm 2G_{\rm write}}{1 - e^{\mp 2G_{\rm write}T_{\rm write}}}} \times \int_0^{T_{\rm write}} e^{\mp G_{\rm write}t}\hat{a}_{\rm in(out)}(t)dt, \tag{5.37}$$

a propagator U for input to output states ($\hat{A}_{\rm write,out} = U^\dagger\hat{A}_{\rm write,in}U$ and $\hat{b}_{\rm write}(T_{\rm write}) = U^\dagger\hat{b}_{\rm write}(0)U$) can be defined as

$$\begin{aligned} U(T_{\rm write}) =& \exp(i\sqrt{1 - e^{-2G_{\rm write}T_{\rm write}}}\hat{A}^\dagger_{\rm write,in}b^\dagger_{\rm write}) \\ &\times \exp(G_{\rm write}T_{\rm write}(-1 - \hat{A}^\dagger_{\rm write,in}\hat{A}_{\rm write,in} - \hat{b}^\dagger_{\rm write}\hat{b}_{\rm write})) \\ &\times \exp(-i\sqrt{1 - e^{-2G_{\rm write}T_{\rm write}}}\hat{A}_{\rm write,in}\hat{b}_{\rm write}). \end{aligned} \tag{5.38}$$

Starting with the density matrix of the mechanical resonator, initially in a thermal state,

$$\rho_b(0) = (1-p)\sum_{n\geq 0} p^n|n\rangle\langle n|, \tag{5.39}$$

with $p = n_{\rm th}/(1+n_{\rm th})$, the density matrix of the optomechanical system after the write pulse is $\rho_{A,b}(T_{\rm write}) = U(T_{\rm write})[0_A\rangle\langle 0_A| \otimes \rho_b(0)]U^\dagger(T_{\rm write})$. The detection of a sideband photon collapses the optical state to $|1_A\rangle$, so applying the operator $|1_A\rangle\langle 1_A| \otimes \mathbb{I}_b$ to the final system density matrix $\rho_{A,b}(T_{\rm write})$ and tracing over the optical states produces the heralded mechanical resonator state

$$\begin{aligned}\rho_b^{\rm cond}(T_{\rm write}) &= 1\frac{{\rm Tr}_A\big\{(|1_A\rangle\langle 1_A| \otimes \mathbb{I}_b)\rho_{A,b}(T_{\rm write})\big\}}{{\rm Tr}_{A,b}\big\{(|1_A\rangle\langle 1_A| \otimes \mathbb{I}_b)\rho_{A,b}(T_{\rm write})\big\}} \\ &= (1-pe^{-G_{\rm write}T_{\rm write}})^2 \sum_{n\geq 0} p^n e^{-nG_{\rm write}T_{\rm write}}(n+1)|n+1\rangle\langle n+1|. \end{aligned} \tag{5.40}$$

In the case of the mechanical resonator starting deep in its ground state ($n_{\rm th} \ll 1$ and $p \ll 1$), a pulse with duration short enough such that $G_{\rm write}T_{\rm write} \ll 1$ results in the single phonon Fock state term dominating in Eqn. 5.40. Thus the detection of a sideband photon in these conditions heralds the $|1_b\rangle$ mechanical state.

Following the blue-detuned drive pulse (and after a dark-state duration of $T_{\rm off}$), a red-detuned readout pulse can be used to measure and verify the heralded single phonon state. Here the interaction Hamiltonian during the read pulse is $\hat{H}_{\rm RSB} = -\hbar G\hat{a}^\dagger\hat{b} + {\rm h.c.}$, and absorption of a phonon results in the creation of a resonant photon. As with the intensity interferometry shown earlier in this chapter, detecting the sideband photon correlation with an HBT apparatus allows for the statistics of the acoustic field to be measured. In this case, the single phonon Fock state produces

$$g^{(2)}_{\rm cond}(\tau=0) = \frac{2pe^{-G_{\rm write}T_{\rm write}}(2+pe^{-G_{\rm write}T_{\rm write}})}{(1+pe^{-G_{\rm write}T_{\rm write}})^2} \approx 4n_{\rm th}. \tag{5.41}$$

The zero-delay second-order correlation function falls with the thermal mechanical occupation, and nears zero when the resonator begins deep in its quantum ground state.

The optomechanical crystal cavities of this work, with their large optomechanical coupling rate ($g_0 \sim 1$ MHz), high mechanical frequency ($\omega_{\rm m}/2\pi \sim 5$ GHz), and narrow optical linewidth ($\kappa/2\pi > 500$ MHz) easily meet the weak-coupling and sideband-resolved criteria for heralding and verifying single phonon Fock states. Recent experiments studying thermalization dynamics of optomechanical crystals at sub-Kelvin temperatures [111, 176] have shown that these devices also attain long mechanical decoherence times $\tau_{\rm th} = (\gamma_{\rm i}(1+\langle n\rangle))^{-1} = 475\ \mu$s when cryogenically cooled deep into the quantum ground state with $\langle n\rangle = 0.021$. Specifically, the experiment described in Ref. [176] utilizes pulsed excitation in order to avoid the deleterious optical heating effects explained in Section 4.1 and Ref. [111]. Phonon counting during red- and blue-detuned laser pulses with widths of $T_{\rm pulse} < 300$ ns and repetition rate approaching 1 MHz simultaneously achieves average occupation $\langle n\rangle < 1$ and effective cooperativity $C_{\rm eff} = C/n_{\rm th} > 1$ during the full pulse duration. These parameters meet the condition enabling the earlier assumption that the mechanics are slowly varying in the Fock-state heralding step (namely, $T_{\rm write} + T_{\rm off} \ll \tau_{\rm th}$). Thus the single-phonon

generation should be realizable with high-fidelity, as should the phonon addition and subtraction process of Ref. [25]. Remaining experimental developments in this area require the generation of blue- and red-detuned optical pulses to be integrated with the existing phonon counting and intensity interferometry apparatus.

Chapter 6

Conclusion

This dissertation is the culmination of a concentrated effort towards developing the experimental capabilities necessary for the creation and observation of non-classical phononic states in optomechanical crystals. In conjunction with the dissertation of Seán Meenehan, robust and efficient fiber optical couplers have been developed for cryogenic operation, and measurement techniques have been demonstrated which are well-suited to fulfilling the requirements of recent proposals for mechanical quantum state perparation and detection.

The design, fabrication, and characterization of a self-aligned fiber-optic integration method has been shown to enable high-efficiency optical coupling to silicon nitride optomechanical resonators. These V-groove couplers transform a single optical mode between an optical fiber and a zipper optomechanical resonator, allowing for single-sided coupling with one detection channel. The combination of high efficiency and single-sided coupling qualify this method for experiments which rely critically on high detection efficiency of intracavity photons. In this regard, the performance of a V-groove coupled device was benchmarked against the standard quantum limit (SQL) in a continuous measurement of the position of a nanobeam. With high-precision homodyne spectroscopy techniques, mechanical motion was transduced with an imprecision within a factor of 3 of the SQL, representing an order of magnitude improvement over comparable experiments in the optical domain and matching the performance of state-of-the-art microwave domain measurements. The V-groove device allows for permanent fiber coupling via epoxy, and is compatible with cryogenic systems such as dilution refrigerators. This coupling architecture has also proved useful to a variety of collaborative efforts both within and outside of the Painter research group, including; packaging and noise reduction in optomechanical accelerometers, fiber access to hybrid nanophotonic/atomic-ensemble systems, and wavelength multiplexing of single photon detectors.

Another fiber coupling method was developed for high-mechanical-frequency silicon optomechanical crystals. Here, the nanobeam resonator is coupled efficiently through a single detection channel to a lensed optical fiber tip, which is dynamically positioned relative to the device using motorized translation stages. Although these end-fire couplers are not permanently coupled like the V-groove

devices, sensitive alignment can be achieved without the use of in-situ microscope imaging, enabling its use in dilution refrigerators for cryogenic cooling to motional ground states. Using such an end-fire coupler, the nanobeam resonator was detected near its ground state using heterodyne spectroscopy, although at levels far above those predicted for thermalization at sub-Kelvin temperatures. It was eventually determined that small levels of optical absorption within the optical cavity were heating the structure to such a degree that the weak (by design) coupling of the acoustic mode to its exterior environment could not overcome. Even for probe laser powers so low that average intracavity photon numbers were 0.01, absorption heated the device to thermal occupancies greater than 1.

These initial cryogenic results revealed the need for a new approach. Since continuous-wave optical probing gave rise to such heating that mechanical ground states could not be achieved simultaneously with large parametric optomechanical coupling, pulsed-probing was an obvious choice. A particularly powerful experimental toolset pairs pulsed-probing with single photon detection, allowing for both direct measurement of the dynamic time response of the system and high detection efficiency. For this reason we proceeded to develop experimental techniques for photon counting of the optical cavity output, in a process we term phonon counting. Phonon counting occurs through single photon detection of a sideband photon, which is correlated to a phonon emission or absorption event within the resonator. Appropriately filtering the cavity output light allows for high-sensitivity phonon counting, which, when paired with pulsed probing, can efficiently detect the motional ground state with large coherent optomechanical coupling.

Although these tools were developed for cryogenic application, they also enabled a novel experiment to be performed at room temperature. Using two single photon detectors, intensity interferometry can be performed on the cavity radiation in a similar manner to the famous Hanbury-Brown Twiss experiment. Measuring the second-order temporal coherence function then shows qualitative features determined by the physical state of the radiation source, in this case of the mechanical oscillation. At room temperature, two distinct modes of mechanical oscillation are achievable; thermal, chaotic motion, and coherently oscillating limit-cycle motion. The transition between these two regimes occurs as the laser drive power is increased, and is analogous the the threshold condition of a conventional laser. I have followed analyses in literature to show that the above-threshold regime of the mechanical oscillator features strong reduction of amplitude noise, similarly to the clamping of spontaneous emission in optical lasers. We measured the correlation function as a function of power, and observed the oscillator transition from thermal bunching to the coherent non-bunching expected for a displaced thermal state.

With the optical coupling and measurement techniques developed in this work, a range of quantum domain optomechanics experiments are feasible. Two of these proposed observations, limit-cycle phonon anti-bunching and single phonon Fock state heradling, have been reviewed. While these measurements are on the horizon following straightforward extensions of the phonon counting

and intensity interferometry apparatus, many more fascinating experiments lie ahead. In particular, optomechanical crystals are uniquely suited to scaling to arrays of multiple devices. Lithographically defined optomechanical circuits in two dimensions have the potential to use both optical and acoustic waveguides [177, 178] to interconnect the optomechanical crystal array, exchanging photons or phonons in specific geometries. Beyond the usual paradigm of cavity optomechanics involving isolated single mechanical elements, coupled optomechanical crystal arrays have been proposed as a way to realize optomechanical memories [18], nanomechanical circuits for continuous variable quantum information processing [20], phononic quantum networks [21], and as a platform for engineering and studying quantum many-body physics of optomechanical metamaterials [22–24].

In yet another potential avenue of integration, other photonic elements can be coupled to optomechanical crystals to perform more experimental functions on the microchip. Single nanowire superconducting photon detectors (SNSPDs), fabricated on-chip and coupled through a waveguide to the output detection channel of an optomechanical crystal, could allow the phonon counting measurement to be performed without incurring the optical losses of multiple fiber couplings and manipulation in room-temperature instrumentation. Initial developments in the fabrication of SNSPDs coupled to nanobeam cavities are described in the Appendix to this dissertation. These detectors and waveguides could be coupled to high-quality optical cavities, with resonances tunable via electromechanical actuation [68, 179] for filtering of cavity radiation and stray light. Arrays of SNSPDs on the outputs of photonic waveguide power splitters could further be arranged into on-chip Hanbury-Brown Twiss experiments or higher-order correlation measurements.

Appendix A

Fabrication of Nanobeam-Integrated Single Photon Detectors

Improvements to the performance of superconducting nanowire single photon detectors (SNSPDs) are critical to broadening their application to quantum information science [133]. Particular effort has focused on increasing system detection efficiency, which has been limited to $< 40\,\%$ until the recent work by Ref. [119]. Although the optical absorption rate of a given section of nanowire is very high, optical mode mismatch between the illuminating field and the only partially area-filling meander pattern significantly reduces the achievable system detection efficiency. Approaches such as resonantly enhancing the absorption by embedding the nanowire within an optical cavity [119, 180] and robustly integrating fiber alignment assemblies [119, 138] have seen considerable improvement, but in many cases the system efficiency is limited by nonuniform constrictions to wire width [181]. To fully encompass the optical mode profile of a near-field optical fiber, most SNSPDs nanowires spiral in an inductor pattern encompassing an area of at least $100\,\mu\mathrm{m}^2$. Over this extended length of wire, fabrication imperfections result in a variation of wire width, and the maximum critical current bias will occur for the critical current density of the narrowest section. Therefore when the SNSPD is operated at this current bias, the wider wire sections will not go into the normal state during a detection, and the detection efficiency is decreased.

A promising solution to many of the optical coupling and fabrication challenges with SNSPDs is to integrate the nanowires into tailorable nanophotonic elements such as waveguides and cavities. Demonstrations of index-waveguide-coupled NbN SPDs have taken advantage of continuous absorption of a travelling-wave to increase the internal detector efficiency, although system detection efficiency was still limited to $\sim 1\,\%$ by poor waveguide-to-fiber optical coupling [182]. With the V-groove fiber couplers discussed here [99], system detection efficiencies of $70-80\,\%$ should be possible. Furthermore, integrating the nanowire on the top surface of a nanobeam or zipper resonator has the

potential to further increase internal detection efficiency, lower dark count rate by filtering the input light, and enable tunable single photon spectrometry through electromechanical actuation [68, 179].

Due to the highly-locallized optical mode volume of a nanobeam, a surface SPD nanowire (Fig. A.1) only requires a few microns of wire length to interact with a significant portion of the optical field. In contrast with meander-inductor nanowires of length $> 100\,\mu$m, the probability of width constrictions is much lower, enabling higher internal detection efficiency. The absorption rate is also tunable in the design of such a structure, as the wire can be overlapped with portions of the nanobeam mode profile with higher or lower magnitude as desired. Nanowires traversing the length of the beam at the cavity center will feature the largest absorption rate. This effect brings up the familiar bandwidth/gain trade-off, as the highest wire absorption rate will significantly decrease the optical quality factor (although still at the level of $Q_{\mathrm{o}} \sim 10^3$), while lower detection efficiencies would allow for finer filtering and resolution with respect to wavelength. Thus for applications requiring multiple chip-based, high-efficiency SPDs the nanowire should cross the near center of the nanobeam cavity, while nanowires crossing the nanobeam several holes diplace from center would be more suitable for spectrometry applications or tasks requiring very low dark count rate.

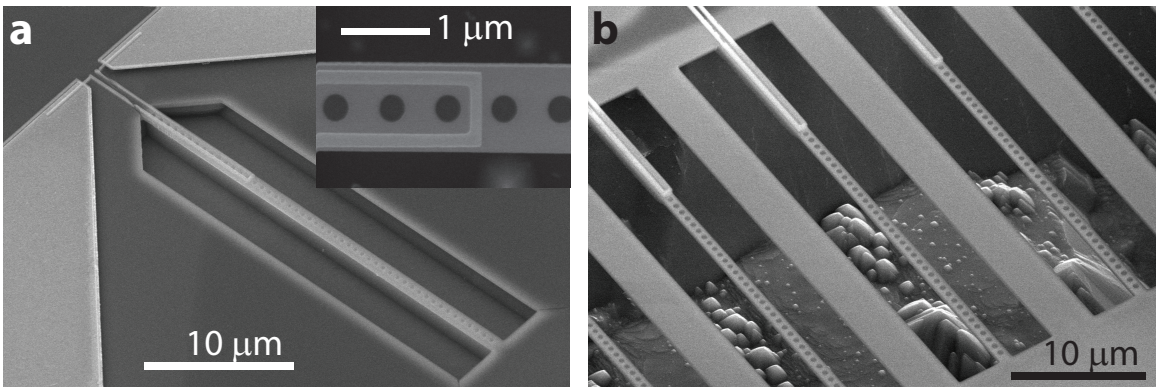

Figure A.1: **Nanobeam Cavity SPDs.** SEM images of **a** a nanobeam cavity integrated with an NbTiN nanowire connected to two electrical bond pads and **b** a test array of nanobeam SNSPD devices. The inset shows a top view of the nanowire and glass encapsulation traversing the nanobeam cavity.

The fabrication process for producing the nanobeam-coupled SNSPDs is detailed in Table A.1. Silicon nitride wafers are coated with a ~ 5 nm thick NbTiN film by the Jet Propulsion Laboratory [183] prior to the process. After Cr/Au wire-bond pads and alignment marks are deposited, best results are found when the defining the photonic structure prior to the patterning of the nanowire. Similarly to the process for silicon end-fire optical couplers, the NbTiN film must be protected by a mask from the TMAH undercut etch step. In this case, NbTiN wire is first etched via reactive-ion plasma (RIE), and is then encapsulated in a patterned glass layer formed from the electron-beam exposure of Dow Chemical flowable-oxide-16 resist (FOx-16). Since glass is robust to TMAH, the

Process Step	Sub-step	Parameter	Parameter Value	Duration
Clean Sample		See Table 2.1		
Apply E-Beam Resist	Spin ZEP-520a	Spin Speed Spin Ramp	2500 rpm 1500 rpm/s	1 min.
	Hot Plate Bake	Temperature	180 °C	2 min.
Liftoff E-Beam Lith.		Dose	250 μC/cm^2	-
E-Beam Development		See Table 2.1		
Cr/Au E-Beam Evap.		See Table A.3		
Cr/Au Liftoff	TCE	-	-	As needed
	Acetone Rinse	-	-	10 sec.
	IPA Rinse	-	-	10 sec.
	N_2 Nozzle Dry	-	-	10 sec.
Apply E-Beam Resist	Spin ZEP-520a	Spin Speed Spin Ramp	2000 rpm 1500 rpm/s	1 min.
	Hot Plate Bake	Temperature	180 °C	2 min.
Photonics E-Beam Lith.		Dose	230 μC/cm^2	-
E-Beam Development		See Table 2.1		
RIE NbTiN Etch		See Table A.4		15 sec.
ICP-RIE Nitride Etch		See Table 2.2		7 min. 25 sec.
Strip E-Beam Resist	TCE	-	-	5 min.
	Acetone Rinse	-	-	10 sec.
	IPA	-	-	10 sec.
	N_2 Nozzle Dry	-	-	10 sec.
Apply E-Beam Resist	Spin FOx-16	Spin Speed Spin Ramp	4000 rpm 1500 rpm/s	1 min.
	Hot Plate Bake	Temperature	180 °C	2 min.
SPD Wire E-Beam Lith.		Dose	1600 μC/cm^2	-
E-Beam Development	MF319	Temperature	50 °C	15 sec.
	H_2O	-	-	30 sec.
	IPA	-	-	1 min.
	N_2 Nozzle Dry	-	-	10 sec.
RIE NbTiN Etch		See Table A.4		15 sec.

Table A.1: **SPD Process Parameters Part I.** Table continued on following page.

nanowire is protected during the undercut etch by FOx-16 on its top and side surfaces and by silicon nitride on its bottom surface. Optionally, the glass encapsulation can be removed after the undercut by a quick HF dip.

The absorption rate of the SNSPD can be investigated at room temperature by measuring the optical quality factor of the nanobeam cavity as a function of wire placement. In Fig. A.2, a test pattern of devices with wires crossing the nanobeam cavity successively closer to center (higher hole number indicates closer to cavity center) is probed with a tapered fiber, and the intrinsic optical quality factor Q_i is extracted from the resnance linewidth and coupling depth. When no wire is present on the cavity, the average $Q_\mathrm{i} = 1.3 \times 10^5$, while nanowires crossing 10 or less holes into the

Process Step	Sub-step	Parameter	Parameter Value	Duration
Apply E-Beam Resist	Spin FOx-16	Spin Speed Spin Ramp	6000 rpm 1500 rpm/s	1 min.
	Hot Plate Bake	Temperature	180 °C	2 min.
SPD Cap E-Beam Lith.		Dose	800 μC/cm^2	-
E-Beam Development	MF319	Temperature	50 °C	15 sec.
	H_2O	-	-	30 sec.
	IPA	-	-	1 min.
	N_2 Nozzle Dry	-	-	10 sec.
Undercut	TMAH	Concentration Temperature	5 % 72 °C	2 hours
	H_2O ×2	-		30 sec.
Oxide Etch	HF:H_2O	Ratio	1:10	5 sec.
	H_2O ×2	-	-	30 sec.
	N_2 Nozzle Dry	-	-	10 sec.

Table A.2: **SPD Process Parameters Part II.** Listing of a chemical in a sub-step specifies submersion at room temperature of the sample in a beaker of the undiluted chemical, unless otherwise specified. Steps or sub-steps with a $\times N$ designation should be repeated for N iterations. IPA refers to Isopropyl Alcohol.

Parameter	Parameter Value
Initial Chamber Pressure	3×10^{-7} Torr
Cr Dep. Rate	0.05 nm/s
Cr Dep. Current	$\sim$ 14 mA
Cr Dep. Final Thickness	$\sim$ 5 nm
Au Dep. Rate	1 nm/s
Au Dep. Current	$\sim$ 45 mA
Au Dep. Final Thickness	$\sim$ 100 nm

Table A.3: **SPD Metal Deposition Recipe.** Process parameters for the chromium/gold (Cr/Au) electrode deposition in the Painter Group BOC Edwards Auto 306 electron beam evaporator

Parameter	Parameter Value
RF Forward Power	80 W
DC Bias Voltage	28 V
SF_6 Flow Rate	30 sccm
Chamber Pressure	20 mTorr
Time Duration	30 sec. (15 sec. of active plasma)

Table A.4: **SPD NbTiN Plasma Etch Recipe.** Process parameters for the NbTiN etch in the Kavli Nanoscience Institute Plasmatherm etcher.

nanobeam show little impact on Q_i. From crossings of 12 or more holes, Q_i decreases rapidly, with a more than 6-fold reduction of Q_i when the wire traverses 20 nanobeam holes. This result indicates that the wire indeed survives the fabrication process, and can feature an absorption rate which strongly dominates over all other optical loss channels in the nanobeam cavity. Therefore photon absorption in the nanowire should occur at much higher probabilities than parasitic scattering or

optical coupling back into the input channel of a V-groove-coupled device. In the first test of Q_i, the devices were measured before removal of the glass encapsulation layer. Testing the same pattern after the HF glass removal step shows that Q_i increases for wire-coupled cavities, but not for the wire-free devices which did not originally suffer from parasitic scattering from the glass encapsulation. Although this trend would seem to show that the nanowire survives the HF etch, further testing of the electrical properties at low temperature (i.e., verifying superconductivity) is required.

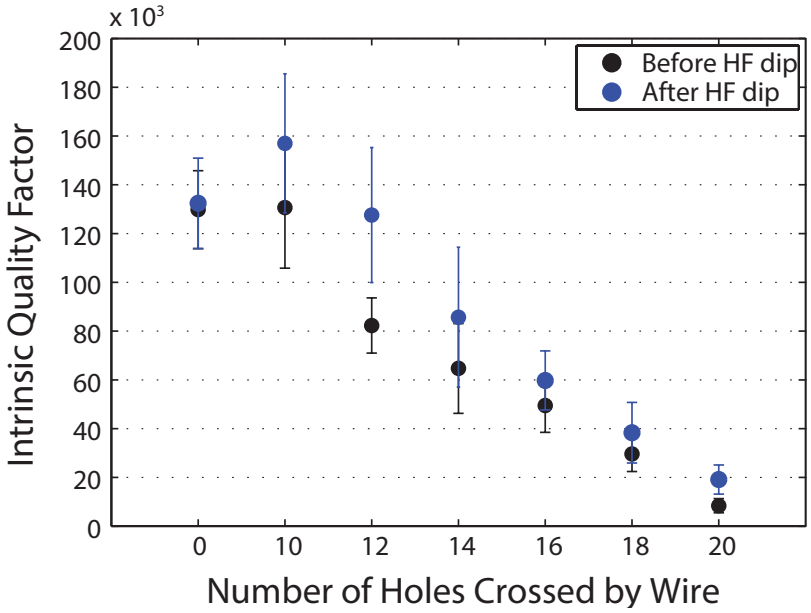

Figure A.2: **Tuning of SPD Absorption.** Variation of the position of the NbTiN nanowire on the optical cavity determines the absorption rate of the optical mode into the SNSPD. The intrinsic optical quality factor drops as the wire traverses more holes approaching the center of the nanobeam cavity. The scattering caused by the glass encapsulation layer is seen by the difference in quality factor before and after HF etching.

Appendix B

Publications

S. M. Meenehan, J. D. Cohen, G. S. MacCabe, F. Marsili, M. D. Shaw, and O. Painter, "Pulsed excitation dynamics of an optomechanical crystal resonator near its quantum ground-state of motion," *arxiv*, 1503.05135 (2015).

J. D. Cohen, S. M. Meenehan, G. S. MacCabe, S. Gröblacher, A. H. Safavi-Naeini, F. Marsili, M. D. Shaw, and O. Painter, "Phonon counting and intensity interferometry of a nanomechanical oscillator," accepted to *Nature*, *arxiv*, 1410.1047 (2015).

S. M. Meenehan, J. D. Cohen, S. Gröblacher, J. T. Hill, A. H. Safavi-Naeini, M. Aspelmeyer, and O. Painter, "Silicon optomechanical crystal resonator at millikelvin temperatures," *Phys. Rev. A* **90**, 011803(R) (2014).

S.-P. Yu, J. D. Hood, J. A. Muniz, M. J. Martin, R. Norte, C.-L. Hung, S. M. Meenehan, J. D. Cohen, O. Painter, and H. J. Kimble "Nanowire photonic crystal waveguides for single-atom trapping and strong light-matter interactions," *Appl. Phys. Lett.* **104**, 111103 (2014).

J. D. Cohen, S. M. Meenehan, and O. Painter, "Optical coupling to nanoscale optomechanical cavities for near-quantum-limited motion transduction," *Opt. Express* **21**, 11227 (2013).

M. Winger, T. D. Blasius, T. P. Mayer Alegre, A. H. Safavi-Naeini, S. M. Meenehan, J. D. Cohen, S. Stobbe, and O. Painter, "A chip-scale integrated cavity-electro-optomechanics platform," *Opt. Express* **19**, 24905 (2011).

R. Perahia, J. D. Cohen, S. M. Meenehan, T. P. Mayer Alegre, and O. Painter, "Electrostatically tunable optomechanical "zipper" cavity laser," *Appl. Phys. Lett.* **97**, 191112 (2010).

Bibliography

[1] J. Kepler, *De Cometis Libelli Tres* (Augsburg, 1619).

[2] J. C. Maxwell, *A treatise on electricity and magnetism*, Vol. 2 (Clarendon Press, Oxford, 1873).

[3] A. Einstein, "On the electrodynamics of moving bodies," *Annalen der Physik* **17**, 891 (1905).

[4] P. Lebedev, "Untersuchungen über die Druckkräfte des Lichtes," *Ann. Phys.* **6**, 433–458 (1901).

[5] E. F. Nichols and G. F. Hull, "A preliminary communication on the pressure of heat and light radiation," *Phys. Rev.* **13**, 307–320 (1901).

[6] A. H. Compton, "A Quantum Theory of the Scattering of X-rays by Light Elements," *Phys. Rev.* **21**, 483 (1923).

[7] T. H. Maiman, "Stimulated optical radiation in ruby," *Nature* **187**, 493 (1960).

[8] A. Ashkin, J. M. Dziedzic, J. E. Bjorkholm, and S. Chu, "Observation of a single-beam gradient force optical trap for dielectric particles," *Optics Letters* **11**, 288 (1986).

[9] D. J. Wineland, R. E. Drullinger, and F. L. Walls, "Radiation pressure cooling of bound resonant absorbers," *Phys. Rev. Lett.* **40**, 1639 (1978).

[10] S. Chu, L. Hollberg, J. E. Bjorkholm, A. Cable, and A. Ashkin, "Three-dimensional viscous confinement and cooling of atoms by resonance radiation pressure," *Phys. Rev. Lett.* **55**, 48–51 (1985).

[11] V. B. Braginsky, *Eksp. Teor. Fiz.* **53**, 1434 (1967).

[12] V. B. Braginsky, A. B. Manukin, and M. Y. Tikhonov, "Investigation of dissipative ponderomotive effects of electromagnetic radiation," *Sov. Phys. JETP* **31**, 829 (1970).

[13] C. M. Caves, K. S. Thorne, R. W. P. Drever, V. D. Sandberg, and M. Zimmermann, "On the measurement of a weak classical force coupled to a quantum-mechanical oscillator. I. Issues of principle," *Rev. Mod. Phys.* **52**, 341–392 (1980).

[14] C. Caves, K. Thorne, R. Drever, V. D. Sandberg, and M. Zimmermann, "On the measurement of a weak classical force coupled to a quantum-mechanical oscillator," *Reviews of Modern Physics* **52**, 341–392 (1980).

[15] C. M. Caves, "Quantum-Mechanical Radiation-Pressure Fluctuations in an Interferometer," *Phys. Rev. Lett.* **45**, 75–79 (1980).

[16] V. Braginsky and F. Khalili, *Quantum Measurements* (Cambridge University Press, 1995).

[17] T. J. Kippenberg and K. J. Vahala, "Cavity Opto-Mechanics," *Opt. Express* **15**, 17172–17205 (2007).

[18] D. Chang, A. H. Safavi-Naeini, M. Hafezi, and O. Painter, "Slowing and stopping light using an optomechanical crystal array," *New J. Phys.* **13**, 023003 (2011).

[19] K. Børkje, A. Nunnenkamp, and S. M. Girvin, "Proposal for Entangling Remote Micromechanical Oscillators via Optical Measurements," *Phys. Rev. Lett.* **107**, 123601 (2011).

[20] M. Schmidt, M. Ludwig, and F. Marquardt, "Optomechanical circuits for nanomechanical continuous variable quantum state processing," *New J. Phys.* **14**, 125005 (2012).

[21] S. J. M. Habraken, K. Stannigel, M. D. Lukin, P. Zoller, and P. Rabl, "Continuous mode cooling and phonon routers for phononic quantum networks," *New J. Phys.* p. 115004 (2012).

[22] A. Tomadin, S. Diehl, M. D. Lukin, P. Rabl, and P. Zoller, "Reservoir engineering and dynamical phase transitions in optomechanical arrays," *Phys. Rev. A* **86**, 033821 (2012).

[23] M. Ludwig and F. Marquardt, "Quantum Many-Body Dynamics in Optomechanical Arrays," *Phys. Rev. Lett.* **111**, 073603 (2013).

[24] M. Schmidt, V. Peano, and F. Marquardt, "Optomechanical Metamaterials: Dirac polaritons, Gauge fields, and Instabilities," *arXiv:1311.7095* (2013).

[25] M. R. Vanner, M. Aspelmeyer, and M. S. Kim, "Quantum State Orthogonalization and a Toolset for Quantum Optomechanical Phonon Control," *Phys. Rev. Lett.* **110**, 010504 (2013).

[26] C. Galland, N. Sangouard, N. Piro, N. Gisin, and T. J. Kippenberg, "Heralded single phonon preparation, storage and readout in cavity optomechanics," *Phys. Rev. Lett.* **112**, 143602 (2014).

[27] S. M. Meenehan, *Cavity Optomechanics at Millikelvin Temperatures*, Ph.D. thesis, California Institute of Technology (2015).

[28] A. Abramovici, W. E. Althouse, R. W. P. Drever, Y. Grsel, S. Kawamura, F. J. Raab, D. Shoemaker, L. Sievers, R. E. Spero, K. S. Thorne, R. E. Vogt, R. Weiss, S. E. Whitcomb, and M. E. Zucker, "LIGO: The Laser Interferometer Gravitational-Wave Observatory," *Science* (1992).

[29] T. Corbitt, Y. Chen, E. Innerhofer, H. Müller-Ebhardt, D. Ottaway, H. Rehbein, D. Sigg, S. Whitcomb, C. Wipf, and N. Mavalvala, "An All-Optical Trap for a Gram-Scale Mirror," *Phys. Rev. Lett.* **98**, 150802 (2007).

[30] B. M. Zwickl, W. E. Shanks, A. M. Jayich, C. Yang, A. C. Bleszynsk-Jayich, J. D. Thompson, and J. G. E. Harris, "High quality mechanical and optical properties of commercial silicon nitride membranes," *Appl. Phys. Lett.* **92**, 103125 (2008).

[31] J. D. Thompson, B. M. Zwickl, A. M. Jayich, F. Marquardt, S. M. Girvin, and J. G. E. Harris, "Strong dispersive coupling of a high-finesse cavity to a micromechanical membrane," *Nature* **452**, 72–75 (2008).

[32] S. Gigan, H. R. Böhm, M. Paternostro, F. Blaser, G. Langer, J. B. Hertzberg, K. C. Schwab, D. Bäuerle, M. Aspelmeyer, and A. Zeilinger, "Self-cooling of a micromirror by radiation pressure," *Nature* **444**, 67–70 (2006).

[33] S. Gröblacher, J. B. Hertzberg, M. R. Vanner, G. D. Cole, S. Gigan, K. C. Schwab, and M. Aspelmeyer, "Demonstration of an ultracold micro-optomechanical oscillator in a cryogenic cavity," *Nature Phys.* **5**, 485–488 (2009).

[34] M. D. LaHaye, O. Buu, B. Camarota, and K. C. Schwab, "Approaching the Quantum Limit of a Nanomechanical Resonator," *Science* **304**, 74–77 (2004).

[35] K. C. Schwab and M. L. Roukes, "Putting Mechanics into Quantum Mechanics," *Physics Today* **58**, 36–42 (2005).

[36] C. A. Regal, J. D. Teufel, and K. W. Lehnert, "Measuring nanomechanical motion with a microwave cavity interferometer," *Nature Phys.* **4**, 555–560 (2008).

[37] M. Eichenfield, R. Camacho, J. Chan, K. J. Vahala, and O. Painter, "A picogram- and nanometre-scale photonic-crystal optomechanical cavity," *Nature* **459**, 550–555 (2009).

[38] M. Eichenfield, J. Chan, R. M. Camacho, K. J. Vahala, and O. Painter, "Optomechanical crystals," *Nature* **462**, 78–82 (2009).

[39] C. Kittel, *Introduction to Solid State Physics* (Wiley, 2004).

[40] J. D. Joannopoulos, S. G. Johnson, J. N. Winn, and R. D. Meade, *Photonic Crystals: Molding the Flow of Light* (Princeton University Press, 2008).

[41] J. Chan, *Laser cooling of an optomechanical crystal resonator to its quantum ground state of motion*, Ph.D. thesis, California Institute of Technology (2012).

[42] J. Chan, T. P. M. Alegre, A. H. Safavi-Naeini, J. T. Hill, A. Krause, S. Gröblacher, M. Aspelmeyer, and O. Painter, "Laser cooling of a nanomechanical oscillator into its quantum ground state," *Nature* **478**, 89–92 (2011).

[43] S. G. Johnson, M. Ibanescu, M. A. Skorobogatiy, O. Weisberg, J. D. Joannopoulos, , and Y. Fink, "Perturbation theory for Maxwells equations with shifting material boundaries," *Phys. Rev. E* **65**, 066611 (2002).

[44] D. K. Biegelsen, "Photoelastic Tensor of Silicon and the Volume Dependence of the Average Gap," *Phys. Rev. Lett.* **32**, 1196 (1974).

[45] J. Chan, A. H. Safavi-Naeini, J. T. Hill, S. Meenehan, and O. Painter, "Optimized optomechanical crystal cavity with acoustic radiation shield," *Appl. Phys. Lett.* **101**, 081115 (2012).

[46] A. H. Safavi-Naeini, J. Chan, J. T. Hill, S. Gröblacher, H. Miao, Y. Chen, M. Aspelmeyer, and O. Painter, "Laser noise in cavity-optomechanical cooling and thermometry," *New J. Phys.* **15**, 035007 (2013).

[47] A. Naik, O. Buu, M. D. LaHaye, A. D. Armour, A. A. Clerk, M. P. Blencowe, and K. C. Schwab, "Cooling a nanomechanical resonator with quantum back-action," *Nature* **443**, 193–196 (2006).

[48] F. Marquardt, J. P. Chen, A. A. Clerk, and S. M. Girvin, "Quantum Theory of Cavity-Assisted Sideband Cooling of Mechanical Motion," *Phys. Rev. Lett.* **99**, 093902 (2007).

[49] T. Rocheleau, T. Ndukum, C. Macklin, J. B. Hertzberg, A. A. Clerk, and K. C. Schwab, "Preparation and detection of a mechanical resonator near the ground state of motion," *Nature* **463**, 72–75 (2010).

[50] J. D. Teufel, T. Donner, D. Li, J. W. Harlow, M. S. Allman, K. Cicak, A. J. Sirois, J. D. Whittaker, K. W. Lehnert, and R. W. Simmonds, "Sideband cooling of micromechanical motion to the quantum ground state," *Nature* **475**, 359–363 (2011).

[51] R. Rivière, S. Deléglise, S. Weis, E. Gavartin, O. Arcizet, A. Schliesser, and T. J. Kippenberg, "Optomechanical sideband cooling of a micromechanical oscillator close to the quantum ground state," *Phys. Rev. A* **83**, 063835 (2011).

[52] A. D. O'Connell, M. Hofheinz, M. Ansmann, R. C. Bialczak, M. Lenander, E. Lucero, M. Neeley, D. Sank, H. Wang, M. Weides, J. Wenner, J. M. Martinis, and A. N. Cleland, "Quantum

ground state and single-phonon control of a mechanical resonator," *Nature* **464**, 697–703 (2010).

[53] M. Ludwig, B. Kubala, and F. Marquardt, "The optomechanical instability in the quantum regime," *New Journal of Physics* **10**, 23 (2008).

[54] K. Stannigel, P. Rabl, A. S. Sørensen, P. Zoller, and M. D. Lukin, "Optomechanical Transducers for Long-Distance Quantum Communication," *Phys. Rev. Lett.* **105**, 220501 (2010).

[55] P. Rabl, "Photon blockade effect in optomechanical systems," *Phys. Rev. Lett.* **107**, 63601 (2011).

[56] A. Nunnenkamp, K. Borkje, and S. M. Girvin, "Single-photon Optomechanics," *Phys. Rev. Lett.* **107**, 063602 (2011).

[57] K. Stannigel, P. Rabl, A. S. Sørensen, M. D. Lukin, and P. Zoller, "Optomechanical Transducers for Quantum Information Processing," *Phys. Rev. A* **84**, 042341 (2011).

[58] K. Stannigel, P. Komar, S. J. M. Habraken, S. D. Bennett, M. D. Lukin, P. Zoller, and P. Rabl, "Optomechanical Quantum Information Processing with Photons and Phonons," *Phys. Rev. Lett.* **109**, 013603 (2012).

[59] M. Ludwig, A. H. Safavi-Naeini, O. Painter, and F. Marquardt, "Enhanced Quantum Nonlinearities in a Two-Mode Optomechanical System," *Phys. Rev. Lett.* **109**, 063601 (2012).

[60] A. Kronwald, M. Ludwig, and F. Marquardt, "Full photon statistics of a light beam transmitted through an optomechanical system," *Phys. Rev. A* **87**, 013847 (2013).

[61] A. A. Clerk, M. H. Devoret, S. M. Girvin, F. Marquardt, and R. J. Schoelkopf, "Introduction to quantum noise, measurement, and amplification," *Rev. Mod. Phys.* **82**, 1155–1208 (2010).

[62] J. D. Teufel, T. Donner, M. A. Castellanos-Beltran, J. W. Harlow, and K. W. Lehnert, "Nanomechanical motion measured with an imprecision below that at the standard quantum limit," *Nature Nanotech.* **4**, 820 (2009).

[63] A. Schliesser, O. Arcizet, R. Rivière, G. Anetsberger, and T. J. Kippenberg, "Resolved-sideband cooling and position measurement of a micromechanical oscillator close to the Heisenberg uncertainty limit," *Nature Phys.* **5**, 509–514 (2009).

[64] G. Anetsberger, E. Gavartin, O. Arcizet, Q. Unterreithmeier, E. Weig, M. Gorodetsky, J. Kotthaus, and T. Kippenberg, "Measuring nanomechanical motion with an imprecision below the standard quantum limit," *Phys. Rev. A* **82**, 061804 (2010).

[65] M. Poggio, C. L. Degen, H. J. Mamin, and D. Rugar, "Feedback cooling of a cantilever's fundamental mode below 5 mK," *Phys. Rev. Lett.* **99**, 017201 (2007).

[66] K. H. Lee, T. G. McRae, G. I. Harris, J. Knittel, and W. P. Bowen, "Cooling and Control of a Cavity Optoelectromechanical System," *Phys. Rev. Lett.* **104**, 123604 (2010).

[67] T. Li, S. Kheifets, and M. G. Raizen, "Millikelvin cooling of an optically trapped microsphere in vacuum," *Nature Phys.* **7**, 527 (2011).

[68] R. Perahia, J. D. Cohen, S. Meenehan, T. P. M. Alegre, , and O. Painter, "Electrostatically tunable optomechanical zipper cavity laser," *Appl. Phys. Lett.* **97**, 191112 (2010).

[69] M. Dakss, L. Kuhn, P. F. Heidrich, , and B. Scott, "Grating coupler for efficient excitation of optical guided waves in thin films," *Appl. Phys. Lett.* **16**, 523 (1970).

[70] D. Taillaert, P. Bienstman, and R. Baets, "Compact efficient broadband grating coupler for silicon-on-insulator waveguides," *Optics Letters* **29**, 2749 (2004).

[71] X. Chen, C. Li, C. K. Y. Fung, S. M. G. Lo, and H. K. Tsang, "Apodized Waveguide Grating Couplers for Efficient Coupling to Optical Fibers," *IEEE Photonic. Tech. L.* **22**, 1156–1158 (2010).

[72] M. Li, W. H. P. Pernice, and H. X. Tang, "Broadband all-photonic transduction of nanocantilevers," *Nature Nanotech.* **4**, 377 (2009).

[73] J. C. Knight, G. Cheung, F. Jacques, and T. A. Birks, "Phase-matched excitation of whispering-gallery-mode resonances by a fiber taper," *Opt. Lett.* **22**, 1129–1131 (1997).

[74] P. E. Barclay, K. Srinivasan, M. Borselli, and O. Painter, "Experimental demonstration of evanescent coupling from optical fibre tapers to photonic crystal waveguides," *Electron. Lett.* **39**, 842–844 (2003).

[75] P. E. Barclay, K. Srinivasan, and O. Painter, "Design of photonic crystal waveguides for evanescent coupling to optical fiber tapers and integration with high-Q cavities," *J. Opt. Soc. Am. B* **20**, 2274–2284 (2003).

[76] P. E. Barclay, K. Srinivasan, M. Borselli, and O. Painter, "Efficient input and output fiber coupling to a photonic crystal waveguide," *Opt. Lett.* **29**, 697–699 (2004).

[77] C. P. Michael, M. Borselli, T. J. Johnson, C. Chrystal, and O. Painter, "An optical fiber-taper probe for wafer-scale microphotonic device characterization," *Opt. Express* **15**, 4745–4752 (2007).

[78] K. Srinivasan and O. Painter, "Linear and nonlinear optical spectroscopy of a strongly coupled microdisk-quantum dot system," *Nature* **450**, 862–865 (2007).

[79] A. H. Safavi-Naeini, T. P. M. Alegre, J. Chan, M. Eichenfield, M. Winger, Q. Lin, J. T. Hill, D. Chang, and O. Painter, "Electromagnetically induced transparency and slow light with optomechanics," *Nature* **472**, 69–73 (2011).

[80] A. H. Safavi-Naeini, J. Chan, J. T. Hill, T. P. M. Alegre, A. Krause, and O. Painter, "Observation of Quantum Motion of a Nanomechanical Resonator," *Phys. Rev. Lett.* **108**, 033602 (2012).

[81] J. T. Hill, A. H. Safavi-Naeini, J. Chan, and O. Painter, "Coherent optical wavelength conversion via cavity optomechanics," *Nature Commun.* **3**, 1196 (2012).

[82] M. Cai, O. Painter, and K. J. Vahala, "Observation of Critical Coupling in a Fiber Taper to a Silica-Microsphere Whispering-Gallery Mode System," *Phys. Rev. Lett.* **85**, 74 (2000).

[83] COMSOL Multiphysics 3.5, http://www.comsol.com/.

[84] Lumerical Solutions Inc. http://www.lumerical.com/tcad-products/fdtd/.

[85] M. A. Rosa, N. Q. Ngo, D. Sweatman, S. Dimitrijev, and H. B. Harrison, "Self-Alignment of Optical Fibers with Optical Quality End-Polished Silicon Rib Waveguides Using Wet Chemical Micromachining Techniques," *IEEE Journal of Selected Topics in Quantum Electronics* **5**, 1249 (1999).

[86] R. Moosburger, R. Hauffe, U. Siebel, D. Arndt, J. Kropp, and K. Petermann, "Passive Alignment of Single-Mode Fibers to Integrated Polymer Waveguide Structures Utilizing a Single-Mask Process," *IEEE Photon. Technol. Lett.* **11**, 848 (1999).

[87] O. Mitomi, K. Kasaya, and H. Miyazawa, "Design of a single-mode tapered waveguide for low-loss chip-to-fiber coupling," *IEEE J. Quantum Elect.* **30**, 1787–1793 (1994).

[88] V. R. Almeida, R. R. Panepucci, and M. Lipson, "Nanotaper for compact mode conversion," *Opt. Lett.* **28**, 1302–1304 (2003).

[89] S. McNab, N. Moll, and Y. Vlasov, "Ultra-low loss photonic integrated circuit with membrane-type photonic crystal waveguides," *Opt. Express* **11**, 2927–2939 (2003).

[90] L. Chen, C. R. Doerr, Y.-K. Chen, and T.-Y. Liow, "Low-Loss and Broadband Cantilever Couplers Between Standard Cleaved Fibers and High-Index-Contrast Si_3N_4 or Si Waveguides," *IEEE Photonic. Tech. Lett.* **22**, 1744–1746 (2010).

[91] H. Tada, A. E. Kumpel, R. E. Lathrop, J. B. Slanina, P. Nieva, P. Zavracky, I. N. Miaoulis, and P. Y. Wong, "Thermal expansion coefficient of polycrystalline silicon and silicon dioxide thin films at high temperatures," *J. Appl. Phys.* **87**, 4189 (2000).

[92] C. Unger and W. Stoecklein, "Characterization of the bending sensitivity of fibers by the MAC-value," *Optics Communications* **107**, 361 (1994).

[93] S. Gröblacher, J. T. Hill, A. H. Safavi-Naeini, J. Chan, and O. Painter, "Highly efficient coupling from an optical fiber to a nanoscale silicon optomechanical cavity," *Appl. Phys. Lett.* **103**, 181104 (2013).

[94] A. G. Krause, M. Winger, T. D. Blasius, Q. Lin, and O. Painter, "A high-resolution microchip optomechanical accelerometer," *Nature Photonics* **6**, 768–772 (2012).

[95] V. B. Braginsky, M. L. Gorodetsky, and F. Y. Khalili, "Quantum limits and symphotonic states in free-mass gravitational-wave antennae," *Phys. Lett. A* **246**, 485–497 (1998).

[96] G. M. Harry, "Advanced LIGO: the next generation of gravitational wave detectors," *Class. Quantum Grav.* **27**, 084006 (2010).

[97] The LIGO Scientific Collaboration, "A gravitational wave observatory operating beyond the quantum shot-noise limit," *Nature Phys.* **7**, 962–965 (2011).

[98] M. A. Taylor, J. Janousek, V. Daria, J. Knittel, B. Hage, H.-A. Bachor, and W. P. Bowen, "Biological measurement beyond the quantum limit," *Nature Photon.* **7**, 229–233 (2013).

[99] J. D. Cohen, S. M. Meenehan, and O. Painter, "Optical coupling to nanoscale optomechanical cavities for near quantum-limited motion transduction," *Opt. Express* **21**, 11227–11236 (2013).

[100] V. B. Braginsky, Y. I. Vorontsov, and K. S. Thorne, "Quantum Nondemolition Measurements," *Science* **209**, 547–557 (1980).

[101] J. Suh, A. J. Weinstein, C. U. Lei, E. E. Wollman, S. K. Steinke, P. Meystre, A. A. Clerk, and K. C. Schwab, "Mechanically Detecting and Avoiding the Quantum Fluctuations of a Microwave Field," *Science* **344**, 1262–1265 (2014).

[102] A. H. Safavi-Naeini, S. Gröblacher, J. T. Hill, J. Chan, M. Aspelmeyer, and O. Painter, "Squeezed light from a silicon micromechanical resonator," *Nature* **500**, 185–189 (2013).

[103] Q. Lin, J. Rosenberg, X. Jiang, K. J. Vahala, and O. Painter, "Mechanical Oscillation and Cooling Actuated by the Optical Gradient Force," *Phys. Rev. Lett.* **103**, 103601 (2009).

[104] T. P. Purdy, R. W. Peterson, and C. A. Regal, "Observation of Radiation Pressure Shot Noise on a Macroscopic Object," *Science* **339**, 801–804 (2013).

[105] P. Rabl, C. Genes, K. Hammerer, and M. Aspelmeyer, "Phase-noise induced limitations on cooling and coherent evolution in optomechanical systems," *Phys. Rev. A* **80**, 063819 (2009).

[106] A. M. Jayich, J. C. Sankey, K. Børkje, D. Lee, C. Yang, M. Underwood, L. Childress, A. Petrenko, S. M. Girvin, and J. G. E. Harris, "Cryogenic optomechanics with a Si_3N_4 membrane and classical laser noise," *New J. Phys.* **14**, 115018 (2012).

[107] P.-F. Cohadon, A. Heidmann, and M. Pinard, "Cooling of a Mirror by Radiation Pressure," *Phys. Rev. Lett.* **83**, 3174–3177 (1999).

[108] C. Genes, D. Vitali, P. Tombesi, S. Gigan, and M. Aspelmeyer, "Ground-state cooling of a micromechanical oscillator: comparing cold damping and cavity-assisted cooling schemes," *Phys. Rev. A* **77**, 033804 (2008).

[109] D. Kleckner and D. Bouwmeester, "Sub-kelvin optical cooling of a micromechanical resonator," *Nature* **444**, 75–78 (2006).

[110] T. Corbitt, C. Wipf, T. Bodiya, D. Ottaway, D. Sigg, N. Smith, S. Whitcomb, and N. Mavalvala, "Optical Dilution and Feedback Cooling of a Gram-Scale Oscillator to 6.9 mK," *Phys. Rev. Lett.* **99**, 160801 (2007).

[111] S. M. Meenehan, J. D. Cohen, S. Gröblacher, J. T. Hill, A. H. Safavi-Naeini, M. Aspelmeyer, and O. Painter, "Silicon optomechanical crystal resonator at millikelvin temperatures," *Phys. Rev. A* **90**, 011803 (2014).

[112] J. Gao, *The Physics of Superconducting Microwave Resonators*, Ph.D. thesis, California Institute of Technology (2008).

[113] W. A. Phillips, "Tunneling states in amorphous solids," *Journal of Low Temperature Physics* **7**, 351–360 (1972).

[114] P. W. Anderson, B. I. Halperin, and C. M. Varma, "Anomalous low-temperature thermal properties of glasses and spin glasses," *Philos. Mag.* **25**, 1–9 (1972).

[115] A. Stesmans, "Passivation of P_{bo} amd P_{b1} interface defects in thermal (100) Si/SiO_2 with molecular hydrogen," *App. Phys. Lett.* **68** (1996).

[116] M. Borselli, T. J. Johnson, C. P. Michael, M. D. Henry, and O. Painter, "Surface encapsulation for low-loss silicon photonics," *Appl. Phys. Lett.* **91**, 131117 (2007).

[117] A. H. Safavi-Naeini, J. T. Hill, S. Meenehan, J. Chan, S. Gröblacher, and O. Painter, "Two-dimensional phononic-photonic bandgap optomechanical crystal cavity," *Phys. Rev. Lett.* **112**, 153603 (2014).

[118] K. C. Lee, M. R. Sprague, B. J. Sussman, J. Nunn, N. K. Langford, X.-M. Jin, T. Champion, P. Michelberger, K. F. Reim, D. England, D. Jaksch, and I. A. Walmsley, "Entangling Macroscopic Diamonds at Room Temperature," *Science* **334**, 1253–1256 (2011).

[119] F. Marsili, V. B. Verma, J. A. Stern, S. Harrington, A. E. Lita, T. Gerrits, I. Vayshenker, B. Baek, M. D. Shaw, R. P. Mirin, and S. W. Nam, "Detecting single infrared photons with 93Nature Photon." **7**, 210–214 (2013).

[120] R. Pike, "Lasers, photon statistics, photon-correlation spectroscopy and subsequent applications," *J. Eur. Opt. Soc. - Rapid Publications* **5**, 10047S (2010).

[121] A. Geata and R. W. Boyd, "Stochastic dynamics of stimulated Brillouin scattering in an optical fiber," *Phys. Rev. A* **44**, 3205–3209 (1991).

[122] M. Dammig, G. Zinner, F. Mitschke, and H. Welling, "Stimulated Brillouin scattering in fibers with and without external feedback," *Phys. Rev. A* **48**, 3301 (1993).

[123] A. A. Fotiadi, R. Kiyan, O. Deparis, P. Megret, and M. Blondel, "Statistical properties of stimulated Brillouin scattering in single-mode optical fibers above threshold," *Optics Letters* **27**, 83 (2002).

[124] A. Castro, F. R. Fairfield, and E. Brooks Shera, "Fluorescence Detection and Size Measurement of Single DNA Molecules," *Anal. Chem.* **65**, 849 (1993).

[125] E. E. Hoover and J. A. Squier, "Advances in multiphoton microscopy technology," *Nature Photonics* **7**, 93–101 (2013).

[126] W. Becker, *Advanced Time-Correlated Single Photon Counting Techniques* (Springer Verlag, New York, 2005).

[127] E. Knill, R. Laflamme, and G. J. Milburn, "A scheme for effcient quantum computation with linear optics," *Nature* **409**, 46–52 (2001).

[128] H. J. Kimble, "The quantum internet," *Nature* **453**, 1023 (2008).

[129] R. H. Hadfield, "Single-photon detectors for optical quantum information applications," *Nature Photon.* **3**, 696 (2009).

[130] S. Pellegrini, R. E. Warburton, J. J. L. Tan, J. S. Ng, A. B. Krysa, K. Groom, J. P. R. David, S. Cova, M. J. Robertson, and G. S. Buller, "Design and Performance of an InGaAsInP Single-Photon Avalanche Diode Detector," *IEEE J. Quantum Elec.* **42**, 397 (2006).

[131] G. N. Goltsman, O. Okunev, G. Chulkova, A. Lipatov, A. Semenov, K. Smirnov, B. Voronov, and A. Dzardanov, "Picosecond superconducting single-photon optical detector," *App. Phys. Lett.* **79**, 705 (2001).

[132] B. Cabrera, R. M. Clarke, P. Colling, A. J. Miller, S. Nam, and R. W. Romani, "Detection of single infrared, optical, and ultraviolet photons using superconducting transition edge sensors," *App. Phys. Lett.* **73**, 735 (1998).

[133] C. M. Natarajan, M. G. Tanner, and R. H. Hadfield, "Superconducting nanowire single-photon detectors: physics and applications," *Superconductor Science and Technology* **25**, 063001 (2012).

[134] S. Miki, T. Yamashita, Z. Wang, and H. Terai, "A 64-pixel NbTiN superconducting nanowire single-photon detector array for spatially resolved photon detection," *Opt. Express* **22**, 7811 (2014).

[135] D. Rosenberg, A. J. Kerman, R. J. Molnar, and E. A. Dauler, "High-speed and high-efficiency superconducting nanowire single photon detector array," *Opt. Express* **21**, 1440 (2013).

[136] S. Miki, T. Yamashita, H. Terai, and Z. Wang, "High performance fiber-coupled NbTiN superconducting nanowire single photon detectors with Gifford-McMahon cryocooler," *Opt. Express* **21**, 10208 (2013).

[137] V. B. Verma, F. Marsili, S. Harrington, A. E. Lita, R. P. Mirin, and S. W. Nam, "A three-dimensional, polarization-insensitive superconducting nanowire avalanche photodetector," *App. Phys. Lett.* **101**, 251114 (2012).

[138] A. J. Miller, A. E. Lita, B. Calkins, I. Vayshenker, S. M. Gruber, and S. W. Nam, "Compact cryogenic self-aligning fiber-to-detector coupling with losses below one percent," *Opt. Express* **19**, 9102 (2011).

[139] L. Mandel and E. Wolf, *Optical Coherence and Quantum Optics* (Cam, 1995).

[140] R. H. Brown and R. Q. Twiss, "Correlation between photons in two coherent beams of light," *Nature* **177**, 27–29 (1956).

[141] R. H. Brown and R. Q. Twiss, "A test of a new type of stellar interferometer on Sirius," *Nature* **178**, 1046–1048 (1956).

[142] I. Silva and O. Freire, "The concept of the photon in question: the controversy surrounding the HBT effect circa 1956-1958," *Historical Studies in the Natural Sciences* **43**, 453 (2013).

[143] A. A. Michelson, "On the application of interference methods to astronomical measurements," *Astrophys. J.* **51**, 257 (1920).

[144] A. A. Michelson and F. G. Pease, "Measurement of the diameter of α Orionis with the Interferometer," *Astrophys. J.* **51**, 249 (51).

[145] E. Brannen and H. I. S. Ferguson, "The question of correlation between photons in coherent light rays," *Nature* **178**, 481 (1956).

[146] E. M. Purcell, "The Question of Correlation Between Photons in Coherent Light Rays," *Nature* **178**, 1449–1450 (1956).

[147] R. J. Glauber, "Coherent and Incoherent States of the Radiation Field," *Phys. Rev.* **131**, 2766–2788 (1963).

[148] R. J. Glauber, "The Quantum Theory of Optical Coherence," *Phys. Rev.* **130**, 2529–2539 (1963).

[149] E. Hanamura, Y. Kawabe, and A. Yamanaka, *Quantum Nonlinear Optics* (Springer, 2007).

[150] D. F. Walls and G. J. Milburn, *Quantum Optics* (Springer, 1994).

[151] H. J. Kimble, M. Dagenais, and L. Mandel, "Photon Antibunching in Resonance Fluorescence," *Phys. Rev. Lett.* **39**, 691 (1977).

[152] F. Diedrich and H. Walther, "Nonclassical radiation of a single stored ion," *Phys. Rev. Lett.* **58**, 203 (1987).

[153] P. Michler, A. Imamoglu, M. D. Mason, P. J. Carson, G. F. Strouse, and S. K. Buratto, "Quantum correlation among photons from a single quantum dot at room temperature," *Nature* **406**, 968 (2000).

[154] R. Brouri, A. Beveratos, J.-P. Poizat, and P. Grangier, "Photon antibunching in the fluorescence of individual color centers in diamond," *Optics Letters* **25**, 1294 (2000).

[155] M. Ueda and M. Kitagawa, "Reversibility in quantum measurement processes," *Phys. Rev. Lett.* **68**, 3424 (1992).

[156] M. Ueda, N. Imoto, and H. Nagaoka, "Logical reversibility in quantum measurement: General theory and specific examples," *Phys. Rev. A* **53**, 3808 (1996).

[157] T. Kippenberg, H. Rokhsari, T. Carmon, A. Scherer, and K. Vahala, "Analysis of Radiation-Pressure Induced Mechanical Oscillation of an Optical Microcavity," *Phys. Rev. Lett.* **95**, 033901 (2005).

[158] I. Bargatin and M. L. Roukes, "Nanomechanical Analog of a Laser: Amplification of Mechanical Oscillations by Stimulated Zeeman Transitions," *Phys. Rev. Lett.* **91**, 138301 (2003).

[159] G. P. Agrawal and N. K. Dutta, *Long-wavelength Semiconductor lasers* (Van Nostrand, 1986).

[160] L. Allen and J. H. Eberly, *Optical resonance and two-level atoms* (Dover Publications, 1975).

[161] L. A. Coldren, S. W. Corzine, and M. L. Masanovic, *Diode lasers and photonic integrated circuits* (Wiley, 2011), 2 edition.

[162] X. L. Feng, C. J. White, A. Hajimiri, and M. L. Roukes, "A self-sustaining ultrahigh-frequency nanoelectromechanical oscillator," *Nature Nanotech.* **3**, 342 (2008).

[163] K. Vahala, M. Herman, S. Knunz, V. Batteiger, G. Saathoff, T. W. Hansch, and T. Udem, "A phonon laser," *Nat. Phys.* **5**, 682 (2009).

[164] I. S. Grudinin, H. Lee, O. Painter, and K. J. Vahala, "Phonon Laser Action in a Tunable Two-Level System," *Phys. Rev. Lett.* **104**, 083901 (2010).

[165] J. B. Khurgin, M. W. Pruessner, T. H. Stievater, and W. S. Rabinovich, "Laser-rate-equation description of optomechanical oscillators," *Phys. Rev. Lett.* **108**, 223904 (2012).

[166] D. A. Rodrigues and A. D. Armour, "Amplitude noise suppression in cavity-driven oscillations of a mechanical resonator," *Phys. Rev. Lett.* **104**, 053601 (2010).

[167] F. Marquardt, J. G. E. Harris, and S. M. Girvin, "Dynamical Multistability Induced by Radiation Pressure in High-Finesse Micromechanical Optical Cavities," *Phys. Rev. Lett.* **96**, 103901 (2006).

[168] A. G. Krause, J. T. Hill, M. Ludwig, A. H. Safavi-Naeini, J. Chan, F. Marquardt, and O. Painter, *in preparation* (2014).

[169] H. Saito and H. Hyuga, "Relaxation of Schroedinger cat states and displaced thermal states in a density operator representation," *Jour. of the Phys. Soc. of Japan* **65**, 1648 (1996).

[170] F. Davidson and L. Mandel, "Correlation mesurements of laser beam fluctuations near threshold," *Phys. Lett.* **25A**, 700 (1967).

[171] M. Lax and M. Zwanziger, "Exact photocount statistics: lasers near threshold," *Phys. Rev. A* **7**, 750 (1973).

[172] M. Lax, "Classical noise V: Noise in self-sustained oscillators," *Phys. Rev.* **160**, 290 (1967).

[173] P. R. Rice and H. J. Carmichael, "Photon statistics of a cavity-QED laser: A comment on the laser-phase-transition analogy," *Phys. Rev. A* **50**, 4318 (1994).

[174] J. Qian, A. A. Clerk, K. Hammerer, and F. Marquardt, "Quantum Signatures of the Optomechanical Instability," *Phys. Rev. Lett.* **109**, 253601 (2012).

[175] N. Lörch, J. Qian, A. Clerk, F. Marquardt, and K. Hammerer, "Laser Theory for Optomechanics: Limit Cycles in the Quantum Regime," *Phys. Rev. X* **4**, 011015 (2014).

[176] S. M. Meenehan, J. D. Cohen, G. S. MacCabe, F. Marsili, M. D. Shaw, and O. Painter, "Pulsed excitation dynamics of an optomechanical crystal resonator near its quantum ground-state of motion," *in preparation* (2015).

[177] A. H. Safavi-Naeini and O. Painter, "Design of optomechanical cavities and waveguides on a simultaneous bandgap phononic-photonic crystal slab," *Opt. Express* **18**, 14926 (2010).

[178] A. H. Safavi-Naeini and O. Painter, "Proposal for an optomechanical traveling wave phonon-photon translator," *New J. Phys.* **13**, 013017 (2011).

[179] M. Winger, T. D. Blasius, T. P. M. Alegre, A. H. Safavi-Naeini, S. Meenehan, J. Cohen, S. Stobbe, and O. Painter, "A chip-scale integrated cavity-electro-optomechanics platform," *Opt. Express* **19**, 24905–24921 (2011).

[180] S. Miki, T. Yamashita, M. Fujiwara, M. Sasaki, and Z. Wang, "Enhancing Detection Efficiency by Applying an Optical Cavity Structure in a Superconducting Nanowire Single-Photon Detector," *IEEE Trans. Electron* **E94**, 260 (2011).

[181] F. Marsili, F. Najafi, E. Dauler, F. Bellei, X. Hu, M. Csete, R. J. Molnar, and K. K. Berggren, "Single-Photon Detectors Based on Ultranarrow Superconducting Nanowires," *Nano* **11**, 2048 (2011).

[182] W. H. P. Pernice, C. Schuck, O. Minaeva, M. Li, G. Goltsman, A. Sergienko, and H. X. Tang, "High-speed and high-efficiency travelling wave single-photon detectors embedded in nanophotonic circuits," *Nature Commun.* **3**, 1325 (2012).

[183] J. A. Stern and W. H. Farr, "Fabrication and Characterization of Superconducting NbN Nanowire Single Photon Detectors," *IEEE Trans. on Appl. Superconductivity* **17**, 306 (2006).